THE NATURE OF ACTIVE GALAXIES

By

SCOTT CHRISTOPHER CHAPMAN

B. Sc. (Honours Physics and Mathematics) University of British Columbia, 1995

M. Sc. (Astronomy) University of British Columbia, 1996

A THESIS SUBMITTED IN PARTIAL FULFILLMENT OF

THE REQUIREMENTS FOR THE DEGREE OF

DOCTOR OF
Philosophy

in

THE FACULTY OF GRADUATE STUDIES

Department of Physics and Astronomy

We accept this thesis as conforming

to the required standard

THE UNIVERSITY OF BRITISH COLUMBIA

January 1999

In presenting this thesis in partial fulfilment of the requirements for an advanced degree at the University of British Columbia, I agree that the Library shall make it freely available for reference and study. I further agree that permission for extensive copying of this thesis for scholarly purposes may be granted by the head of my department or by his or her representatives. It is understood that copying or publication of this thesis for financial gain shall not be allowed without my written permission.

Astronomy
The University of British Columbia
129-2219 Main Mall
Vancouver, Canada
V6T 1Z4

Date: June 11/99

Abstract

Many details of the structure of Active Galactic Nuclei (AGN) galaxies continue to elude researchers in the field. To shed light on some of the enigmas related to the fueling and classification of AGN, I have studied the core structure of a sample of 37 nearby Seyfert galaxies at high resolution using adaptive optics on the CFHT. This dataset consists of near-IR imaging from 1 to 3 μm (the J,H, and K bands).

I first describe the instruments and observing techniques along with a presentation of the galaxy sample properties. I then outline the detailed data reduction and image processing required with adaptive optics observations, highlighting some of the associated unavoidable perils. The main difficulty with adaptive optics observations is a PSF artifact I discovered which is associated with guiding on galactic nuclei. This represents the main hurdle to identifying small-scale ($<1''$) structures in the core regions of galaxies using adaptive optics.

A detailed multi-wavelength study is pursued for two nearby Seyfert galaxies, NGC3227 and NGC2992. With these objects, the current ideas of Seyfert fueling and unification of Seyfert types are scrutinized, focusing on the high spatial resolution achieved using adaptive optics in the near-IR. The dynamical processes and differing classifications of these galaxies are substantially clarified through their core morphologies. These studies show that scientific results can be established with AO data, in spite of the above mentionned artifact. For NGC2992, a spiral structure within the central $6''$ and a $1''$ extended feature are traced down to the core at the resolution of our images. We speculate, based on these observed structures, that multiple radio components are superposed which contribute to the observed figure-8 morphology in the VLA images: one associated with the spiral structure in the galaxy disk, and another flowing out of the galaxy plane. With NGC3227, an assembly of star formation knots lying in a spiral/ring pattern is suggestive of embedded spiral arms within the larger-scale spiral of the outer galaxy. An elongation of $PA \sim 40°$ may be a nuclear disk or bar structure, although the blue colors

are suggestive of some scattered nuclear continuum emission. The extended radio feature observed with MERLIN is coincident with the near-IR region of knots assuming a spiral/ring pattern, but may still be associated with an outflow.

I then address whether the classification of Seyfert galaxy types can be explained via patchy dust at fairly large distances ($\sim 100\,pc$) from the central engine. Maps of dust extinction are constructed with the deep view afforded by the near-IR. These are compared with optical images observed with the Hubble Space Telescope (HST) to aid in distinguishing dust absorption from other emission processes, as well as providing a dust diagnostic with a different range of sensitivity than the near-IR. In the absence of any standardized classification for dust absorption in galaxies, we have developed a graded system of two indices. A dust patchiness index (DPI) characterizes the dust morphology, and a global dust index (GDI) combines the DPI morphological index with a quantitative assessment of the extinction. Applying these indices to the Seyfert sample, we find that Seyfert type 2 galaxies are typically slightly more dusty than Seyfert type 1. However, when later intermediate-type Seyfert galaxies (Seyfert 1.8 and 1.9) and Seyfert 1 with extended nuclei are included with the Seyfert 2, the dust indices indicate a significant difference from the Seyfert types 1 through 1.5. The observational evidence is now such that an alternative should be considered to the standard classification model where the visibility of the type 1 AGN signature is the main differentiator. The new possibility is that Seyfert galaxies are drawn from two different populations: very dusty, and less/non-dusty. Sy2 are then thought almost always to be of the very dusty type. Whether or not the actual Sy1 nucleus is visible in the very dusty type is then merely a result of the current dust configuration of the Seyfert nucleus.

Table of Contents

List of Tables

List of Figures

Acknowledgement

Firstly I would like to thank Gordon Walker, for taking me on as a graduate student and constantly encouraging me to pursue new ideas and topics. I would also like to thank Simon Morris who got me up to speed with the intricacies of observing on Mauna Kea telescopes, as well as nurturing my scientific development. With pleasure, I also acknowledge the discussions and suggestions of Douglas Scott, Greg Fahlman, Paul Hickson, Tim Davidge and John Hutchings.

This research is partially supported by operating grants from the Natural Sciences and Engineering Research Council of Canada.

Chapter 1

Introduction

1.1 Introduction to AGN

Certain galaxies are observed to produce a tremendous amount of energy in their very centes, and are usually designated Active Galactic Nuclei (AGN). The core luminosity can easily exceed the total luminosity of the underlying galaxy, and is emitted across a broad range of wavelengths, from radio waves to x-rays. This great energy cannot come entirely from stars that radiate predominantly in the visible for the following reasons. The main source of energy output in stars is nuclear fusion, with a mass to energy conversion efficiency of less than 0.1%. Variability of the nuclear energy source on timescales of days in some cases implies that the energy is being produced in a region on the order of our solar system in diameter. The density of stars that would therefore be required has never been directly observed. If a sufficient number of stars were contained in this small volume to power the nuclei (which can be as bright as 10^{12} L$\odot$), the stars would quickly collide and coalesce into a single unstable massive object (Haehnelt and Rees 1994). Therefore, the most widely accepted explanation for the AGN phenomenon is accretion of material onto a supermassive black hole (Longair 1996), with a mass of billions of suns in the more extreme cases.

Between 1 and 5% of all galaxies are believed to be active, but it is still largely unknown how galaxies become active or how their evolution progresses. AGN come in many forms, from the nearby Seyfert galaxies with bright nuclei residing mostly in fairly typical spiral galaxies, to quasars and radio galaxies where the host is usually a massive elliptical. The required amount of fuel accreting onto the blackhole can vary from less than one sun per year ($1\,M\odot yr^{-1}$) for Seyferts to $100\,M\odot yr^{-1}$ for luminous quasars.

The history of AGN begins in 1943 when Carl Seyfert made spectroscopic observations of several

galaxy nuclei. He found a non-thermal and non-stellar spectrum, with strong emission lines (Seyfert 1943). These types of active galaxies became known as Seyfert galaxies and their relative proximity presents an opportunity to study in detail the AGN phenomenon. In 1963, B.E. Markarian initiated a program to isolate a sample of galaxies using a selection criterion of excess blue/UV continuum (Markarian 1967). The majority of these galaxies are blue because they have an elevated rate of star formation, but approximately 10% of these galaxies are Seyfert galaxies with the excess blue light being due to the non-thermal UV emission from the active nucleus. Seyfert galaxies are divided into two main types based on their spectral characteristics (Osterbrock 1977). The Seyfert type 1 (Sy1) show a line broadening of several thousand km/s in the permitted emission lines observed in the very core region. This is thought to be a result of the doppler motions of individual gas clouds, ionized by the nuclear continuum radiation - the so-called *broad line region.* The Seyfert type 2 (Sy2) do not display this line broadening but do show the strong high ionization forbidden lines also observed in Sy1.

Classifications according to activity are defined in the catalog of Veron-Cetty & Veron (1986) as follows. Seyfert 1 nuclei have broad permitted hydrogen emission lines; Seyfert 2 nuclei have [OIII]λ5007 strong compared to Hβ, and [NII]λ6584 comparable to Hα. Subclassifications of Sy1 into Seyfert 1.2, 1.5, 1.8 and 1.9 (Osterbrock 1977) have arisen to distinguish the relative strengths of the line broadening. Numerically larger subclasses have weaker broad-line components relative to the narrow lines. Seyfert 1.9 galaxies have a detectable broad line component only in the Hα line. Sy1.8 and lower have detected Hβ with decreasing ratios of [OIII]/Hβ.

1.1.1 Motivation

Most bright galaxies are now thought to host super-massive black holes at their centers (Kormendy et al. 1998, Richstone et al. 1998). AGN hosts must therefore be the galaxies which are capable of efficiently transporting material from the outer galaxy down to the scales on which activity is observed. Another implication is that since all AGN have the same power source, there may well be a unifying thread which explains the huge variety in the AGN types and classifications, as I now discuss.

1.2 Unified model of AGN

There exist unifying models which seek to explain every type of AGN based on a very limited number of physical parameters (Antonucci 1993). The unification hypothesis restricted only to Seyfert galaxies states simply that each Seyfert 2 nucleus actually harbours a normal Seyfert 1 nucleus in its center (Antonucci 1982). The observational signatures which characterize Seyfert 1 nuclei (point-like nonstellar continuum plus broad permitted emission lines) are thought not to be visible in Seyfert 2's because of obscuration along our line-of-sight (LOS) to the central engine. As a consequence, Seyfert 1 nuclei which suffer sufficient extinction will then appear to us as Seyfert 2's.

It has long been suspected that Seyfert 2 nuclei are more heavily obscured than Seyfert 1 nuclei (e.g. Lawrence and Elvis 1982; Malkan and Oke 1983). Seyfert 2 are redder than Seyfert 1's in all wavelength bands from the far-infrared to the X-rays, and a relatively large fraction of their total energy output has been reprocessed by warm dust grains (Edelson and Malkan 1986). The surviving transmitted continuum is then weaker, allowing the scattered continuum light to appear relatively more prominent. With a higher dust covering fraction, the scattering is further enhanced. Thus the proportion of nuclear luminosity which is re-radiated in the thermal infrared is increased (Spinoglio et al. 1989).

The unification hypothesis as such is by no means proven, operating on a scale which is currently beyond the resolution of any telescope at any wavelength. It was once hypothesized that the variety of AGN types might be explained by varying nuclear energy sources, including massive compact stellar clusters (Terlevich et al. 1982). However, it is now becoming apparent that accretion onto a supermassive black hole is the inevitable outcome at the cores of galaxies (Richstone et al. 1998), whether or not there was once a compact starburst in the evolutionary chain. Thus there is little evidence to point towards differences in the type of central engine to account for the varying AGN types.

Assuming the Seyfert unification hypothesis to be true, an outstanding question remains: What are the nature and location of the absorbers that obscure our view of the Seyfert 1 nucleus, which we suppose are always present in the center of a Seyfert 2 galaxy? One possibility has become well known

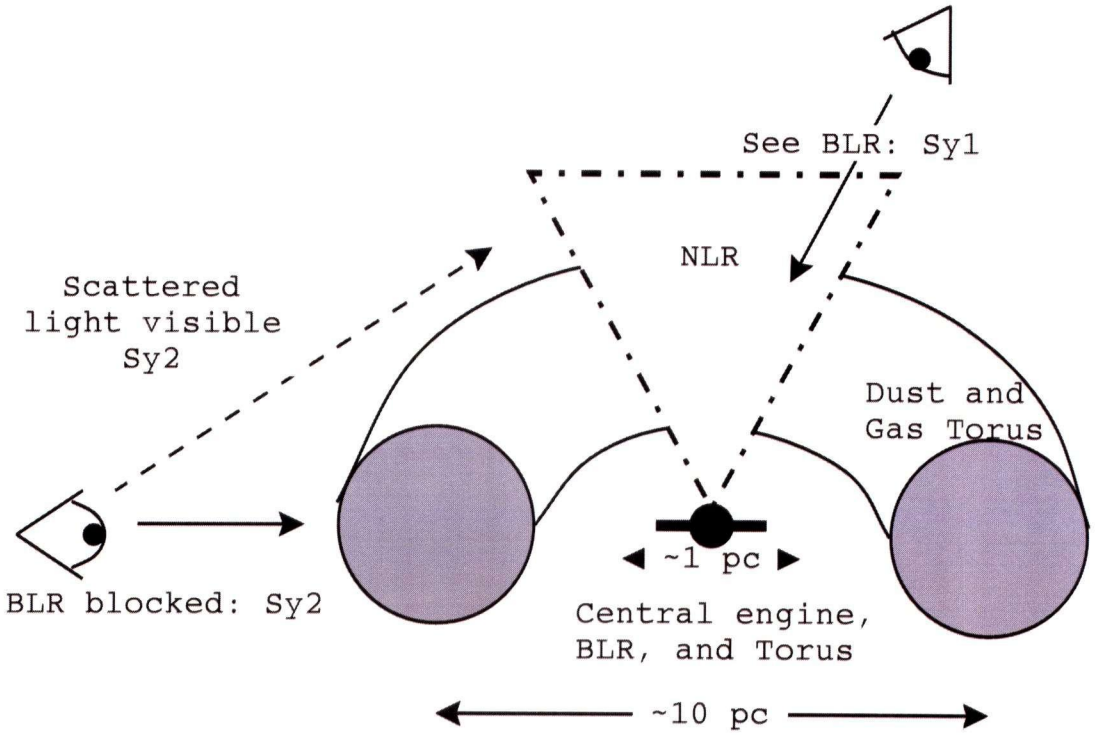

Figure 1.1: The Accreting Torus Model of Seyfert Unification. Viewing angle on an otherwise identical object is the only thing differentiating type 1 from type 2 Seyfert galaxies

since it was sketched in Antonucci (1982). That paper described a particular scenario in which our view of the central continuum and broad-line region is occulted by a dusty thick gas ring which surrounds the central engine, and is closely aligned with its rotation axis. A Seyfert which we view at sufficiently high inclination, through its torus, will appear to us as a type 2. A Seyfert nucleus which we view close enough to a face-on orientation would show us a direct view of its Broad Line Region (BLR), and would thus be classified as type 1. This Accreting Torus Model (ATM) is sketched in Figure 1.1.

This specificity also makes the ATM vulnerable to observational tests. There are three reasonably established observational signatures which do show some support for the ATM: dusty tori, hidden broad line regions, and cones of ionized emission.

1.2.1 The dusty torus

The inner diameter of the torus only has to be large enough to surround and obscure the broad line region. For the typical low-luminosity Seyferts found in our local neighborhood (< 40 Mpc), this is only of order 1 pc. The outer diameter is not expected to be much more than one or two orders of magnitude larger, so that the entire torus structure remains aligned with (and connected to) the central engine, rather than the host galaxy. The gravity of the central engine is likely to be less important than that of the galactic stars at distances of more than 100 parsecs.

The existence of obscuring tori of very high column densities is supported by the low energy cut-offs in the X-ray spectra of Seyfert 2's (e.g. Mulchaey et al. 1992), by strong nuclear emission in the near-infrared vibration-rotation transitions of molecular hydrogen (e.g. Rotaciuc et al. 1991). Ground-based color maps (e.g. 40% of the Seyferts in Mulchaey, Wilson, & Tsvetanov 1994) and a few HST images (e.g. NGC 4261, Jaffe et al. 1993) have revealed structures that have properties consistent with those expected for dusty tori. In the case of NGC 4151, the nuclear red feature is aligned with the large-scale stellar bar, supporting the idea that the bar-driven gas flow provides the material for the opaque torus (Vila-Vilaro et al. 1995). Thus far however, such direct evidence has been minimal and anecdotal, with only a few cases showing extended linear structures which could be interpreted as such a dusty torus.

1.2.2 Hidden Broad Line Regions

If the central obscuration is not too great, one might hope to see signs of broadened lines at longer wavelengths where the effects of dust extinction are reduced. This has indeed been realized with the direct observation of broad wings on infrared recombination lines in objects classified optically as narrow-line AGN (e.g. Nakajima et al. 1991, Veilleux et al. 1997).

Polarimetric studies have also revealed hidden BLRs in some cases. A polarized spectrum can result from scattering or reflection of the AGN continuum into our line of sight, either by dust or by free electrons lying above the obscuring torus. Figure 1.1 depicts this scenario, where the scattering medium is assumed to lie within the cone region above the central engine. The ATM version of Seyfert unification

then appears relatively well established for some Seyfert 2 nuclei which show weak broad emission lines in linear polarized light.

On the other hand, this powerful observational signature has by no means been shown to be universal among Seyfert 2's (Tran et al. 1992,1995a,1995b). In addition, the amount of polarization is never as strong as would be expected in the case of such an ATM. For edge-on galaxies the level of continuum polarization should reach 50% (Miller and Goodrich 1990), whereas no galaxy has ever been observed with more than about 20% polarization. Whether *all* Seyfert 2's harbour obscured Seyfert 1 nuclei is still controversial (Lawrence 1991).

1.2.3 Ionization cones

Extended narrow emission line regions have been observed in some intermediate and type 2 Seyferts. With the obscuring torus model in mind, interpretations of these anisotropic emissions as *ionization cones* were quick to materialize (Pier and Krolik 1992). The idea is that the dusty torus defines an opening angle of continuum emission escaping from the central engine which will ionize the surrounding interstellar medium (ISM) along preferred directions. The resulting narrow emission line regions are visible out to hundreds of parsecs in some cases (See Antonucci 1993 for a review). Based on the observed fact that Seyfert 2's are somewhat more numerous locally than Seyfert 1's, the opening angle of the torus cannot be larger than about π steradians (Edelson et al. 1987, Rush et al. 1996).

Early observations bore little similarity to the hypothesized sharp cones which should exist if the torus model were the cause of the features (Goodrich 1990). However, recent HST results (Hutchings et al. 1998, Wilson et al. 1994) are more convincing, where the improved spatial resolution has shown a definite cone-line morphology of ionized gas. However, there certainly remain many cases where a cone or bi-cone would be expected yet observations have clearly shown NLRs which are not consistent with such a morphology.

1.3 Fueling the nucleus

Another outstanding problem in current AGN research is what role, if any, the host galaxy plays in the fueling of the central engine. For the observed luminosities of Seyferts, mass accretion rates of $\sim 1\ M_\odot\ yr^{-1}$ are required for reasonable mass-to-energy conversion rates. Although the interstellar medium of the host galaxy contains enough mass to be a possible fuel source, it is not clear how matter on kiloparsec scales is transported to the small scales of the nucleus.

1.3.1 Bars as a fueling mechanism

From a theoretical standpoint, galactic bars are perhaps the most viable candidate for facilitating the transfer of mass from large to small scales (Schwartz 1981, Norman 1987, Shlosman, Frank & Begelman 1989).

Such a non-axisymmetric disturbance of the galaxy will exert gravitational torques on the gas within the bar vicinity (Sempere et al. 1995), and is capable of inducing global shocks, thereby driving the inflow of gaseous material towards the galaxy center. Even rather weak bars can drive large non-circular motions (Binney and Tremaine 1987). The gaseous component has been shown numerically (Athanasoula 1992) to lose angular momentum in a pair of shocks along the leading edge of the bar, and to flow toward the center of the galaxy in about 10 rotation periods. The formation of spiral density waves trailing off the bar ends will transport angular momentum outwards leading to further collapse of the central concentration.

Stellar bars represent solid body rotation which implies uniform density along the bar major axis. This is clearly the case in observed bars (Quillen et al. 1996). The angular speed decreases outward in most galaxies, and thus there is a corotation radius at which the angular speed (Ω_{CR}) is equal to the pattern speed of the bar (Ω_b). An *Inner Linblad Resonance* (ILR) occurs when $\Omega - \Omega_b = \kappa/2$, where κ is the epicycle frequency describing the radial oscillation of a star in orbit. When this condition can be met within the bar, gas tends to become trapped in a ring at the resonant radius. This can halt the

inflow of material.

1.3.2 Observational evidence for bars

There have been many attempts to determine the importance of such bars in Seyfert galaxies, but the results have proved inconclusive. MacKenty (1990) imaged a sample of Markarian Seyferts in optical broad-band filters and concluded that many of the galaxies contain a substantial bar component in the stellar distribution. However, other Seyfert samples show little or no evidence that Seyfert nuclei occur more frequently in barred systems than in normal spiral galaxies (Heckman 1980; Simkin, Su, & Schwarz 1980; Moles et al. 1995).

The failure to find evidence for bars in most Seyfert galaxies may be due to the fact that most studies have concentrated on optical wavelengths, where the presence of extinction or a young stellar population might mask any bar structures. For example, the prototypical Seyfert 2 galaxy NGC 1068 is classified as an unbarred spiral at optical wavelengths, but a strong bar is clearly seen in near-infrared images (e.g. Scoville et al. 1988). The near-infrared is expected to be a good place to study the host galaxy of Seyferts because the galaxy energy distribution peaks at $\sim 1\,\mu$m, while the energy distribution of the active nucleus is at a minimum here (Sanders et al. 1989). Furthermore, since neither dust nor young luminous stars strongly affect the observed emission at K band, the light at this wavelength is a good tracer of the mass distribution, and thus bars (e.g. Rix & Rieke 1993).

With the proliferation of large format near-infrared cameras, several ground-based near-IR surveys of Seyferts have recently been undertaken (Kotilainen et al. 1992; Zitelli et al. 1993; McLeod & Reike 1995; Mulchaey, Regan & Kundu 1996). The first two studies were concerned mostly with the nucleus, while the latter studies have focused on the host galaxies. Not surprisingly, the latter two studies have revealed infrared bars in many galaxies previously classified as unbarred based on optical images. Still, a small percentage ($\sim$ 20%) of the Seyfert galaxies studied show no evidence for bars in the infrared.

Even if large-scale bars do exist in all Seyferts, they cannot be entirely responsible for the AGN phenomenon. Nearly all of the "normal" galaxies studied also show evidence for bars in the near-IR,

but none of these galaxies displays strong nuclear activity. In addition, theoretical models indicate that gas inflow generated by a rotating bar extends only down to approximately the inner kiloparsec of the galaxy, not close enough to the central engine for viscosity or cloud-cloud collisions to take over and directly feed the central engine (Piner, Stone, & Teuben 1995).

1.3.3 A bars-within-bars model

Shlosman, Frank & Begelman (1989) have proposed a "bars within bars" mechanism that could continue to drive material towards the nucleus. In their model, gas driven inward from the large-scale stellar bar accumulates in the central few hundred parsecs in a rapidly rotating disk. If the mass of the gas in this disk is an appreciable fraction ($> 20\%$) of the dynamical mass at that radius, the disk may become unstable and a gaseous bar can form. A dynamically unstable series of such bars may exist, driving inflow until the point where the central supermassive blackhole dominates the gravitational potential ($\sim$ inner 50 pc). Nested bars have been observed in the optical (Wozniak et al. 1995) and near-IR (Friedli et al. 1996), but these ground-based images are not able to resolve the bars required to fuel AGN. Although gas collected by a kiloparsec-scale bar may form an initial gas disk, tidal encounters with nearby galaxies may also lead to a "bars within bars" scenario (Mihos & Hernquist 1996), possibly explaining the activity in those objects without large-scale stellar bars. In addition to feeding the central engine, the inflowing material might also produce the dusty tori believed to exist in the centers of Seyfert galaxies (e.g. Antonucci 1993), as discussed in the previous section.

While a sequence of nested bars may develop in some galaxies, several processes may suppress the instability of the gaseous disk and thus prevent fueling of the central engine. For example, star formation may consume most of the transferred mass and stop the inflow. In particular, an inner Lindblad resonance (ILR) may collect the gas in a ring that eventually forms stars. Furthermore any system with a relatively low gas content will never reach a stage where the disk becomes unstable to self-gravity and a gaseous bar forms. All of these processes may explain why the majority of spiral galaxies, even though barred on large scales, do not currently host strong nuclear activity.

1.4 Instrumental Challenges

1.4.1 Resolution

The actual region of activity will likely not be imaged for decades, when optical/near-IR space-born interferometry becomes established with large aperture telescopes. However, it is clear from the above discussion, that there is much to be learned about AGN from highest currently obtainable resolution views of the core regions of these galaxies.

Ground-based images have revealed direct and indirect evidence for the central dusty torus, in the form of small linear structures, and extended anisotropic emission line regions. Space-based HST results were quick to improve on this picture, but suffered from the patchy dust obscuration which plagues the optical wavelengths. Longer wavelength imaging at a similar resolution to the HST has the capability to circumvent some of these obstacles.

Ground-based work has also demonstrated that large-scale bars are a rather common feature of both normal and active spiral galaxies, however they generally do not have the resolution required to test the "bars-within-bars" scenario described above. For nearby Seyferts ($\sim$ 40 Mpc), the resolution of typical ground-based images ($\sim 1''$) corresponds to linear scales $\sim$200 pc. (Distances are calculated throughout assuming the recession velocity is proportional to the distance as $v_R = H_0 D$ and a Hubble constant $H_0 = 50$ km s^{-1}Mpc^{-1} is used.) This is comparable to the scales where we expect the inner gaseous bars to form. Thus, to test the theoretical models for fueling the central engine, even higher resolution images are required.

1.4.2 Atmosphere

The available atmospheric windows impede certain crucial wavelength ranges from being fully utilized. The infra-red region poses many problems for observation (chapter 2). Sub-mm wavelengths observable from the ground are even more difficult to work with, given the large background fluctuations, and redshifts which are constantly placing the regions of interest into unobservable windows. There are also

many wavelengths which simply cannot be observed from the ground at all (e.g. all wavelengths shorter than the far-UV).

The multi-wavelength approach, bringing high-resolution studies from the entire spectral energy distribution (SED) together at the same time for scrutiny (e.g. Ivison et al. 1998, Chapman et al. 1999) appears to be the best way to get a comprehensive picture of AGN galaxies. However, until resolution-matched data across the wavelength spectrum are available for many objects, the full solution to many of the AGN puzzles may lie further in the future.

1.5 Summary - how to attack AGN problems

The outstanding questions of AGN research can be divided broadly into three categories:

1) What is the physical structure of an active galaxy?

2) What causes the activity?

3) What is the time evolution of the activity?

Two approaches can be taken to answer these AGN questions:

1) A statistical approach: obtaining a large sample of objects with the aim of determining common properties, and identifying the underlying correlations between observed parameters.

2) A detailed study of individual objects: attempting to explain simultaneously all of the observed properties.

These two approaches are clearly complementary; a study of an individual object will assume the context of what appears to currently be true statistically, while new statistical studies may be motivated by peculiarities noted in a particular object.

This thesis takes both approaches, first studying specific active galaxies in detail to elucidate rather complicated morphologies and implied processes, and then addressing a statistical question with a sample of 37 galaxies. Chapter 2 describes the instruments and observing techniques along with a presentation of the galaxy sample properties. Chapter 3 outlines the detailed data reduction and image processing

required with adaptive optics observations, highlighting some of the unavoidable associated perils. Chapters 4 and 5 present a multi-wavelength study of two nearby Seyfert galaxies, NGC 2992 and NGC 3227. With these objects, the unification and fueling scenarios described above are scrutinized in detail to see if they continue to be compatible with observations at the fine scales probed by adaptive optics in the near-IR. In Chapter 6, maps of dust extinction are constructed, with the penetrating view afforded in the near-IR. The question is then addressed as to whether the classification of Seyfert galaxy types can be explained via patchy dust at fairly large distances from the actual central engine. The final chapter concludes and summarizes the results, with recommendations for further work in the area.

Chapter 2

Observations

2.1 The Instruments

All the new observations in this thesis were obtained at the Canada-France-Hawaii Telescope (CFHT), using the Adaptive Optics Bonnette (AOB), over three observing runs in March (4 nights) and August (2 nights) 1997, and March 1998 (3 nights). The 1997 runs used the MONICA camera, while the 1998 run used the KIR camera with improved sensitivity and field size. In the following sections, the AOB and the cameras used are described.

2.1.1 PUEO - The adaptive optics bonnette (AOB) on CFHT

Optical aberrations in ground based astronomical images result mainly from random phase distortions of the incoming wave-fronts, induced by atmospheric turbulence above the telescope. The concept behind adaptive optics is the correction of the wave-fronts in real time by a deformable mirror, whose shape is continuously updated to match the current state of the atmospheric turbulence. The CFHT AOB (also called PUEO after the sharp eyed Hawaiian owl) is based on curvature wavefront sensing (Roddier et al. 1991), and uses a 19 zone bimorph deformable mirror (Rigaut et al. 1997) to correct the wavefront distortions.

The atmospheric seeing is characterized using the Fried parameter, r_0, which describes the characteristic coherence length of a thermal turbulence cell. The Fried parameter is wavelength dependent, $r_0 \propto \lambda^{1.2}$ (see for example McLean 1997), so that the median value $r_0 = 17\,\mathrm{cm}$ at $500\,\mathrm{nm}$ (the V-band window in the optical) corresponds to a median value of $102.2\,\mathrm{cm}$ at $2.23\,\mu\mathrm{m}$ (K-band). The corresponding seeing disk in angular units, typically reported at a telescope, is proportional to λ/r_0, where λ is the

Table 2.1: Performance Summary For Median Seeing Conditions at CFHT

Waveband	*V*	*R*	*I*	*J*	*H*	*K*
Wavelength [μm]	0.54	0.65	0.83	1.25	1.65	2.23
Median $r_0(\lambda)$ [cm]	17	21	28	46	65	93
FWHM [arcsec]	0.24	0.19	0.12	0.095	0.11	0.14
FWHM/(λ/D)	7.6	5.1	2.5	1.34	1.18	1.12
$\text{Gain}_{\text{FWHM}}$	2.6	3.2	4.8	5.9	5.0	3.6

† Parameters taken from Rigaut et al. (1998).

wavelength of observation. The resulting profile of a point source which is imaged through the atmosphere by a telescope and camera is designated the point spread function (PSF). The diffraction limit is most closely approached at longer wavelengths, where the performance of the instrument is better. The Strehl ratio describes how close the PSF corrected for atmopheric distortions is to the diffraction limited PSF. It is given by the intensity at the peak of the actual seeing disk divided by the intensity at the peak of the true Airy diffraction pattern.

The performance of the instrument is presented in Table 2.1 with rows 1 and 2 listing the central filter wavelength and median atmospheric Fried parameter respectively. The corrected FWHM of the PSF under median CFHT seeing conditions is reported for different wavelengths (row 3). Also noted are the FWHM as a ratio of the diffraction limit of CFHT (row 4 – λ/D where D=3.65 m is the diameter of the CFHT telescope), and the adaptive optics improvement in FWHM over the uncompensated case ($\text{Gain}_{\text{FWHM}}$), row 5.

2.1.2 The Cameras: MONICA and KIR

The 1997 runs used the MONICA near-IR camera (Nadeau et al. 1994) mounted at the f/20 focus of the Adaptive Optics Bonnette (AOB). The detector is a Rockwell NICMOS3 array with 256 × 256 pixels and a 0.″034 per pixel scale. This camera experienced continual decrease in sensitivity from its use in the commissioning of PUEO to our observing runs through 1997 and 1998. Table 2.2 shows the decrease in photometric zeropoint (providing the calibration in photons/mJy for example), which

Table 2.2: Degradation of the MONICA instrumental zeropoint with time.

Waveband	March 1996	December 1996	March 1997	August 1997
J	23.3[†]	23.1	23.0	22.8
H	22.8	22.7	22.5	22.4
K	22.4	22.2	22.1	21.9

[†] Units of 2.5logADU (analog to digital converter units - proportional to flux). Variations in gain (photons per ADU) have been taken into account.

provides a measure of the throughput of the instrument, and thereby charts the achieved sensitivities over time.

Despite this decrease in sensitivity, and the inherent problems with this generation of near-IR arrays, such as the many bad pixels, amplifier glow, and persistent images (see Clark et al. 1993), MONICA was an extremely well built camera, outperforming many of its contemporaries. There is essentially no correlated noise, and the read noise is ~ 3 times less than for similar cameras used on ESO telescopes such as SHARP II (Beuzit et al. 1997). The dark current is very stable, and does not fluctuate at the edge of the field, permitting the construction of mosaics without prominent edge-effects. This is crucial given the small field of view.

The 1998 observing run took advantage of the newly commissioned KIR camera (Nadeau et al. 1998) which uses the larger 1k×1k Hawaii Infrared detector, and uses a similar chip technology to the MONICA camera (multiplexed HeCdTe material). When mounted at the f/20 focus of AOB, it also has a similar plate scale of 0.″034 per pixel. This camera boasts a superior and larger format near-IR array. The amplifier glow and bad pixels are substantially less noticeable than with the NICMOS3 arrays such as that used in MONICA. The improved sensitivity and 36″ instantaneous field of view make this a far superior science instrument.

2.1.3 HST WFPC2

To complement our near-IR AOB images, HST archive images were downloaded from the Canadian Astrophysics Data Center (CADC). The images were obtained with the Wide Field / Planetary Camera 2 (WFPC2) with the galaxy centered on the 0.″046/pixel CCD (the PC part of WFPC), as part of various snapshot surveys of nearby active galaxies (Malkan et al. 1998, Illingworth et al., in preparation).

All images were taken using the F606W filter centered on 606 nanometers with a mean wavelength

of 5940Å and FWHM of 1500Å. This includes both the Johnson R and V filters. This high throughput filter allows a large number of objects to be obtained rapidly with the Space Telescope. Typical exposure times were 500 seconds.

2.2 Observing Techniques

Observing in the near-IR has many difficulties (Mclean 1997). When coupled with adaptive optics, it presents a whole new set of challenges. First we outline the problems associated with the near-IR night sky. We then describe the actual approach used in obtaining our observations. It will become clear that finding galaxies which can be successfully observed with a natural guide star AO system is a rather difficult undertaking. This will have important implications for the sample completeness issues discussed in section 3.

2.2.1 The near-IR sky

Observations in the near-IR present an increasing number of problems over the optical, as the wavelength increases into the near-IR wavelengths (Sanford et al. 1992). Atmospheric emissions are the first consideration. There are two major sources of the solar-induced non-thermal emission that dominate the near-IR night sky from 1 to 2.5 μm . The first is the polar aurora, due mainly to emission from N_2 molecules, but which is negligible at mid-latitude sites such as Mauna Kea. The dominant problem is *airglow*, which has three components:

- OH vibration-rotation bands
- O_2 IR atmospheric bands
- the near-IR nightglow continuum

The strongest of these is the OH molecule which produces a dense "forest" of emission lines. These OH lines come from a thin layer of the atmosphere at an altitude of about 90 km and the strength of the emission can vary by a factor of 2 or more in half an hour (possibly due to large-scale wave motions in the mesopause).

The second consideration is thermal emission. The atmosphere emits blackbody radiation with an emissivity ϵ depending on the atmospheric opacity at a given wavelength. The emissivity may be less than 0.1 in good atmospheric windows where absorption due to water vapour is low. The thermal

emission by the telescope and warm optics also contributes to the background, since both are typically warmer than the effective water vapour temperature.

As an example of the brightness of the near-IR night sky, we can make a comparison with the optical. The surface brightness in the blue ($\lambda = 0.43\,\mu$m) is V=24 magnitudes/arcsec^2 without moonlight. At 2.2 μm (K-band: see table 2.1), K=13.5 magnitudes/arcsec^2. Fortunately, moonlight is almost negligible in the near-IR (Simons 1992), and time on the telescope is not compromised as it is for bright moon nights at optical wavelengths.

2.2.2 Target acquisition

It is necessary to have the expertise to rapidly determine whether or not a galaxy core will be suitable for guiding. This includes analyzing all available data ahead of time and making quick judgements at the telescope based on the initial performance of the AOB upon locking onto the core. However, choosing a guiding source is also a strong function of the observing conditions - there are many marginal AGN cores which are adequate under first class weather, but become useless as the PSF is smeared out too much when the weather deteriorates. In chapter 3, we pursue this issue further and analyze in detail the available information and how it correlates with observing success. We shall see that results can be rather unpredictable with artifacts and poor guiding becoming significant factors.

Strictly from the point of view of being able to lock onto a given target galaxy core, we have listed the photons seen by the wave-front sensor (WFS) and V-magnitude in the central 1″ in Table 2.3 for all our target galaxies. We have also plotted the V-magnitude of the core region as a function of WFS counts in figure 2.1. The core magnitudes were obtained through photometry of HST optical images, using a 1″ diameter aperture, while the WFS counts were read directly from the observing console during the observations.

There were several galaxies for which we were unable to close the loop on the AOB at all. These all have core V-magnitudes fainter than $V \sim$17 and would lie within or below the marginal guides in figure 2.1 (those near the bottom left of the plot). A best fit has been plotted to quantify the relation and compare with other values in the literature. We find that galaxies with a central magnitude brighter than $V \sim$17 can serve as a guiding source for useful AO correction, depending on atmospheric conditions. It is clear from the scatter in this plot that a tight correlation does not exist between these two quantities. The variation in the observing conditions is a strong factor, as is the actual radial profile of the guiding source – steeper sources provide a better guide. In order to see the effect of profile steepness, we have

plotted all unresolved cores as squares, and all resolved cores as crosses. Essentially all the resolved sources carry either a late-type Seyfert classification (Sy1.8/1.9) or Sy2. All the unresolved sources are Sy1.

Once it is determined that the galaxy core is bright enough (usually $V < 17$) and not too extended, the instrument parameters must be set to match the observing conditions. The optical gain, which governs the response of the deformable mirror actuators, and the order of correction (from tip/tilt only all the way to full 19 mode correction) are the only real decisions available to the observer with the current instrument interface. Once these are set at the optimal range, then the observing strategy comes into play, as the atmospheric conditions may reduce the practicality of certain programs. Typically the gain is set to an intermediate value (e.g. Gain=90), and full correction is used for an extended object like a Seyfert galaxy with a reasonable guiding core, as long as the atmospheric seeing disk is $< 0.8''$ FWHM.

2.2.3 Observational strategies

The three standard broad-band filters covering the near-IR wavelength range (J, H, K) provide a means to quickly image a sizable sample of galaxies whilst gaining considerable spectral information. The different emission properties contributing to the 3 bands allow for discrimination of physical conditions and their relation to structural features of the galaxy (bars, disks, spiral arms etc.). These properties will be studied in detail for the sample galaxies in chapters 4 and 5.

The wavelength dependence of the Fried parameter and the diffraction limit (table 2.1) imply that it may be more desirable to obtain J-band images under the best conditions to get the highest resolution view possible of the core regions of the galaxies. At longer wavelengths (K-band), the diffraction limit can be reached under less than optimal atmospheric conditions, using a reasonably bright guiding source. However, given a finite amount of observing time, the goals of the program must be carefully weighed - the K-band images provide the deepest, least dust-obscured views of the galaxy cores and are perhaps the most scientifically unique at the present time, given the HST's capabilities are in the optical bands.

Further complications arose in the second observing run using the MONICA camera. The filter wheel control malfunctioned, and any filter change required slewing the telescope to zenith and walking up to the dome to manually rotate the desired filter into place. We therefore decided to observe all objects in K-band the first night, followed by H in the second night. In two cases we were also able to observe in J-band. Throughout all the observing runs, single filter images were obtained for some

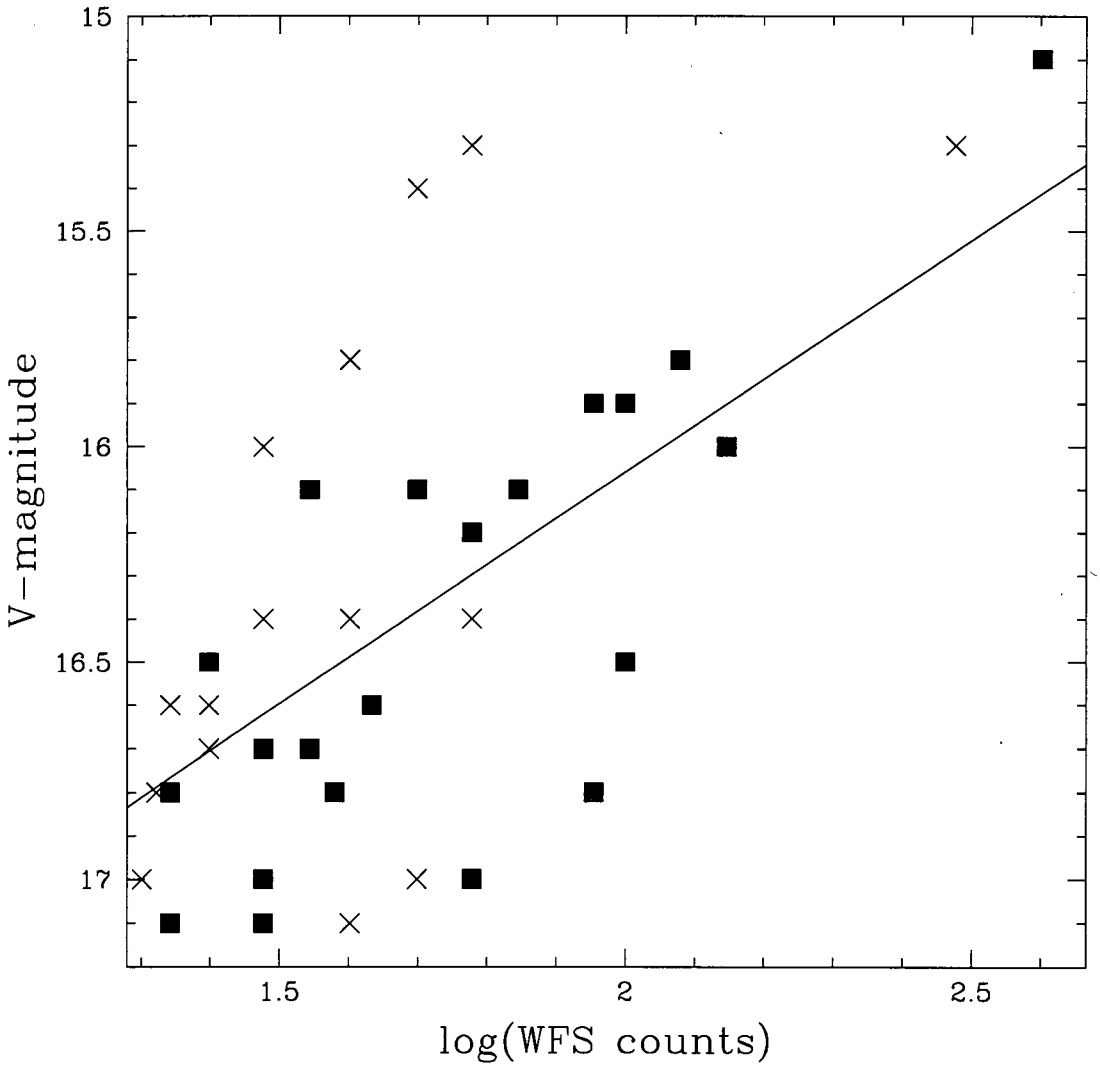

Figure 2.1: The V-magnitude of the core region as a function of counts on the wavefront sensor. Squares represent Seyfert 1 (generally unresolved), crosses Seyfert 2 (resolved in all cases). The solid line represents the best linear fit to the data points.

Table 2.3: AOB Seyfert sample – guide strength

Galaxy	Alternate name	redshift	Sy class	WFS counts	HST V-mag core
Seyfert 1					
ic 4329a	eso 445-g50	0.016	S1	100	16.5
mrk 744	NGC 3786	0.010	S1.8	35	16.7
mrk 766	NGC 4253	0.012	S1.5	38	16.8
mrk 1330	NGC 4593	0.009	S1	90	16.8
ngc 1275		0.008	U1.9	22	17.1
ngc 2639		0.011	R1.9	35	16.1
ngc 2992		0.007	R1.9	43	16.7
ngc 3227	UGC 5620	0.003	S1.5	100	15.9
ngc 3516	UGC 6153	0.009	S1.5	120	15.8
ngc 3998		0.009	S1.5	140	16.0
ngc 4051		0.002	S1.5	90	15.9
ngc 4151		0.002	S1.2	400	14.8
ngc 5033		0.003	U1.8	60	17.0
ngc 5273		0.006	U1.8	30	17.0
ngc 5506	MRK 1376	0.007	R1.9	22	16.8
ngc 5548	MRK 1509	0.017	S1.5	60	16.2
ngc 5728		0.008	R1.9	30	17.1
ngc 6814		0.009	U1	50	16.1
ngc 7469		0.016	S1	70	16.1
Seyfert 2					
mrk 3	UGC 3426	0.014	2	50	15.4
mrk 348	NGC 262	0.014	2	22	16.6
mrk 620	NGC 2273	0.006	2	40	16.4
mrk 1066	UGC 2456	0.012	2	30	16.0
ngc 1068		0.003	2	300	15.1
ngc 1241		0.013	2	20	17.0
ngc 1386		0.002	2	60	16.4
ngc 3081		0.007	2	25	16.6
ngc 3393		0.012	2	30	16.4
ngc 4968	ESO 508-g6	0.009	2	25	16.5
ngc 5005		0.003	2	15	17.1
ngc 5135	ESO 444-g32	0.013	2	43[†]	16.6
ngc 5929	UGC 9851	0.008	2	21	16.8
ngc 5953		0.007	2	40	15.8
ngc 7465	MRK 313	0.006	2	50	17.0
ngc 7582	ESO 291-g16	0.005	2	40	17.1
ngc 7590		0.005	2	25	16.7
ngc 7743		0.007	2	60	15.3

galaxies when the guiding was found to be marginal after acquiring the object. Thus overall, the sample is somewhat heterogeneous in the filter coverage and the level of correction obtained. This will be taken up in subsequent sections.

As the MONICA field size is small ($9'' \times 9''$), blank sky images were taken intermittently between science frames to estimate the true sky background level. It is common practice with near-IR observations to alternate between the sky and source with equal integration times in order to get a statistical sense of the sky variations and thermal telescope glow. We found that we were able to reduce the amount of time spent on the sky to 20% without noticeable loss in photometric accuracy. This algorithm is detailed in chapter 3. On-source images were taken in a mosaic of 4 positions, alternately putting the galaxy core in each of the four quadrants of the array. This allows bad pixels and artifacts to be removed from the final image during the data reduction stage. Even with the larger field size of KIR ($36'' \times 36''$) the galaxies often contribute significantly to the flux at the edge of the frame, and similar observing techniques were used.

Exposure times were estimated using ground-based images and derived magnitudes (J. Mulchaey, private communication), in addition to HST optical images. The central regions of the sample galaxies have surface brightnesses in the range 13–15 H mag/arcsec^2. Our desired exposure time depended on the level of correction generated by the AOB, with the associated Strehl ratio. For a typical near-diffraction limited correction level at H-band, we estimated a signal-to-noise of $\sim$10–40 per pixel for this magnitude range in a 30 minute exposure.

2.3 The observed sample of galaxies

The entire sample of 37 galaxies observed over the three runs is presented in Table 2.4, along with basic parameters related to the galaxies and observations. Seyfert types have been listed using the standard classifications outlined in chapter 1. We note that those galaxies that do not carry an intermediate spectroscopic classification (e.g., Seyfert 1.8) may not have been studied carefully enough to distinguish them from a basic Sy1/2 classification. The Malkan et al. (1998) AGN brightness designation is also listed: S – saturated unresolved, U – unsaturated unresolved, R – resolved. This brightness designation has a rough correlation with the WFS counts from our observations, with S $>$ 50 counts, U $<$ 50 counts. This system will be taken up further in chapter 6 with regard to unification of Seyfert types.

The morphological classes are listed in column 6, first based on $20''$ HST images of the inner regions

of each galaxy (Malkan et al. 1998), followed by that given in the Third Reference Catalog (RC3, Corwin et al. 1994). The morphological classification uses the Hubble tuning fork system running from ellipticals (E) through spirals with increasingly less contribution from the bulge component (E,S0,Sa,Sb,Sc,Sd). The spirals are further divided into barred and unbarred (the "tuning fork" part of the classification scheme). This latter classification agrees with the one given in the RC3 more than 80% of the time to within one full class (e.g., from Sb to Sc).

In the following sections, the reasons for choosing the observed sample are outlined.

2.3.1 Sample completeness and bias

A well defined sample of galaxies is highly desirable if one is to make inferences about galaxy type in general. Our sample of 37 galaxies is drawn mainly from the 91 Seyfert galaxy sample assembled by Maiolino & Rieke (1995) from the Revised Shapely-Ames galaxy catalog, meeting a magnitude requirement of $B < 13.4$. As noted by these authors, the proximity of the RSA Seyferts reduces the dilution of their nuclear spectra by the host galaxy light, so this sample is less biased against low-luminosity nuclei and edge-on galaxies than other Seyfert samples. The galaxies were chosen based on their core brightness for AOB guiding. The objects in our sample have recessional velocities in the range of 1000–5000 $\mathrm{km\,s^{-1}}$, corresponding to a resolution (4 pixels) of 10–50 pc with AOB. All of our galaxies have been imaged with HST in the optical (i.e., the wide band F606W filter at 606 nm) as part of snapshot surveys (mainly Malkan et al. 1998), allowing detailed multiwavelength comparisons to be made at similarly high resolution scales. Some of our galaxies are also currently being imaged at H-band in the near-IR using the HST NICMOS camera (Regan & Mulchaey 1999, in preparation). This will provide a very useful comparison in the future of adaptive optics on large telescopes, in the lead up to the Next Generation Space Telescope (NGST).

Inevitably, our Seyfert sample likely suffers some selection biases. The principal one is that Seyfert 2's are less likely to be included unless they are relatively prominent (i.e., with unusually high nuclear luminosities or star formation rates). This is certainly less of an issue with the RSA sample galaxies. There is however the possible bias of choosing galaxies with bright nuclei for guiding with AOB. This affects all of our targets, but may figure more prominently in the Sy2 population which typically have obscured and extended nuclei. This raises the danger that we are comparing the Seyfert 1 galaxies with Seyfert 2's which are intrinsically more luminous, or less dust obscured. At the extreme, there is a population of heavily dust obscured Seyferts identified by the IR satellite, IRAS, which do not appear

in optical surveys (Bonnato et al. 1988).

For the statistical questions addressed in chapter 6, we seek to characterize our Seyfert sample using the relatively orientation-independent low-frequency radio fluxes (Ulvestad 1986, Ulvestad & Wilson 1984) and [OIII]λ5007 emission line fluxes (Dahari & DeRobertis 1988). We find similar distributions in both these quantities for our Sy1's and Sy2's, which lends confidence to any comparative results. Seyfert galaxies which were not selected in the traditional optical/UV searches may also shed light on possible sample biases. We find that 10 of our Sy1's and 10 of our Sy2's are members of the IRAS 12 μm galaxy sample which is thought to avoid the usual biases of these other methods (Spinoglio and Malkan 1989; Rush et al. 1993).

We compare the morphologies of both the total sample and the 12 μm subsample and find in both a preference for Sy1 nuclei to reside in earlier-type galaxies than Sy2 nuclei. The median morphological class is similar in both samples with Sa for the Sy1's and Sb for the Sy2's. This is consistent with results found by previous studies (Maiolino et al. 1995, Malkan et al. 1998).

2.3.2 Control sample of normal spiral galaxies

Although observing a control sample of non-active spiral galaxies would have been useful as a comparison, instrumental and weather difficulties made it impossible to achieve such a sample within the telescope time awarded. It took 3 observing runs spread out over almost 2 years to obtain just a satisfactory sample of bright Seyfert galaxies. Out of 9 nights allocated on CFHT for this project, 5 were useful scientifically. It was proposed after the first observing run that a sample of the various Seyfert galaxy types would allow certain scientific questions to be properly addressed, thereby making the best use of the time available. An incomplete sub-sample of Seyferts and non-active galaxies would have made it difficult to address the desired questions. It is hoped that normal spiral galaxies will be observed by us and others over the coming years, to allow this comparison to be made.

Table 2.4: The AOB observed Seyfert galaxy sample

Galaxy	Alternate	z	filters	Sy class[a]	Morphology[b]	instrument	b/a[†]
Seyfert 1							
IC4329a	ESO 445-g50	0.016	J,H,K	S1	Sa,S0	KIR	0.2
MRK 744	NGC 3786	0.010	J,H,K	S1.8	Sb,Sa	KIR	0.8
MRK 766	NGC 4253	0.012	J,H,K	S1.5	SBc,Sa	KIR	0.73
MRK 1330	NGC 4593	0.009	J,H,K	S1	Sbc,SBb	KIR	0.7
NGC 1275		0.008	K	U1.9	Sa	MONICA	0.61
NGC 2639		0.011	J,H,K	R1.9	Sb,Sa	KIR	0.55
NGC 2992		0.007	J,H,K	R1.9	?,Sa	KIR/MON	0.27
NGC 3227	UGC 5620	0.003	J,H,K	S1.5	?,SBa	MONICA	0.69
NGC 3516	UGC 6153	0.009	J,H,K	S1.5	S0,S0	KIR	0.82
NGC 3998		0.007	J,H,K	S1.5	E	KIR	n/a
NGC 4051		0.002	J,H,K	S1	Sb,SBbc	KIR	0.77
NGC 4151		0.002	J,H,K	S1	Sa	KIR	0.86
NGC 5033		0.003	J,H,K	U1.8	Sab	KIR/MON	0.43
NGC 5273		0.006	H	U1.8	Sa	KIR	0.60
NGC 5506	MRK 1376	0.007	J	R1.9	edge/Sa	KIR	0.17
NGC 5548	MRK 1509	0.017	J,H,K	S1.5	Sa,S0/a	MONICA	0.88
NGC 5728		0.005	K	R1.9	Sa	MONICA	0.71
NGC 6814		0.009	J,H,K	U1	Sa	MONICA	0.83
NGC 7469		0.016	H	S1	Sb/c,SBa	MONICA	0.69
Seyfert 2							
MRK 3	UGC 3426	0.014	J,H,K	2	S0,S0	KIR	0.72
MRK 348	NGC 262	0.014	H,K	2	Sa,S0a	MONICA	0.65
MRK 620	NGC 2273	0.006	J,H,K	2	SBb,SBa	KIR	0.43
MRK 1066	UGC 2456	0.012	J,H,K	2	Sc,SB0	KIR	0.66
NGC 1068		0.003	H	2	Sbc	MONICA	0.49
NGC 1241		0.013	H	2	Sbc,SBb	MONICA	0.57
NGC 1386		0.002	H,K	2	Sbc,SB0	MONICA	0.29
NGC 3081		0.007	K	2	SB0a,SB0a	KIR	0.43
NGC 3393		0.012	K	2	Sa,SBa	KIR	0.58
NGC 4968	ESO 508-g6	0.009	H	2	Sa/SB0a	KIR	0.47
NGC 5005		0.003	H	2	Sc	MONICA	0.49
NGC 5135	ESO 444-g32	0.013	K	2	Sc,SBab	KIR	0.8
NGC 5929	UGC 9851	0.008	J,H,K	2	S0,Sab	MONICA	0.71
NGC 5953		0.007	H	2	Sc,Sa	MONICA	0.74
NGC 7465	MRK 313	0.006	J,H,K	2	Sb	MONICA	0.52
NGC 7582	ESO 291-g16	0.005	H,K	2	?,SBab	MONICA	0.46
NGC 7590		0.005	H	2	Sd,Sbc	MONICA	0.39
NGC 7743		0.007	H,K	2	S0,SBab	MONICA	0.78

[a] Seyferts types have been listed using both the Goodrich (1987) subclass designation, and the Malkan et al. (1998) AGN brightness designation: S – saturated (> 50 APD counts), U – unsaturated (< 50 APD counts), R – resolved

[b] Morphology class: [Malkan et al. (1998), RC3]. The Malkan classifications are based on the central 20″ of the galaxy imaged with HST.

[†] Axis ratio: $\sin i = b/a$, where i is the disk inclination.

Chapter 3

Image Processing

3.1 Reductions

In the reduction of digital images for astronomical use, several processing steps are required to obtain the highest precision results. Defects in the image (termed 'bad pixels'), whether cosmetic defects in the detector itself or cosmic ray produced bright spots, must be removed. Flat-field images are crucial to account for variations in the pixel-to-pixel response of the detector. Dark current generated by thermal processes in the detector and amplifier bias levels must be subtracted. Varying sky background levels must be subtracted. With longer wavelength observations, thermal glow of the telescope and instruments must be taken into account. Finally the images must be calibrated against reference stars imaged during the observing run. These steps are detailed in the following sections. All data reduction was done with either custom IDL routines (Interactive Data Language), or IRAF scripts (Image Reduction Astronomy Facility).

3.1.1 Pre-processing

Bad pixel removal was accomplished by forming a bad-pixel map using all the sky and flat-field images taken. Various clipping algorithms were attempted in order to find all the bad pixels, but ultimately were forced to identify remaining bad pixels by eye and add them manually to the bad-pixel map. Although somewhat tedious, this only needs to be done once per observing run. The use of all the data in forming the bad-pixel map ensures that cosmic ray hits will not be mis-identified as bad pixels, since they will not appear in the same place in more than one exposure. The bad pixels are then fit using surrounding pixels by linear interpolation. Cosmic rays are identified and removed during the mosaic reconstruction of the final image. A *sigma clipping* algorithm is first run over all the source frames to remove and interpolate over cosmic rays with large deviation from the surrounding pixels. A similar filter is used in construction of the mosaic to leave out any deviant pixels which differ by more than 3σ between the 4 overlapping frames.

Flat-field images were taken on the dome with the lamps turned on and off to account for the thermal glow of the telescope. Light from the flat lamps results in a differential response from each pixel element multiplied by the exposure time. However, a thermal component due to the telescope and instruments (and the read noise) is additive. Since we only want the multiplicative component when we divide each image by the flat-field, subtraction of the flats with the lamps off from those with the lamps on provides the desired flat-field image. Although claims have been made that sky or twilight flats can provide better results due to more uniform illumination, we found the dome flats to be accurate enough for our purposes given the uncertainties in the calibrations.

3.1.2 Thermal background subtraction

In order to maximize the time spent on source for our survey observations, we devised an observing approach to minimize the sky chopping typically used with near-IR observing with small area detectors. The non-standard approach we used incorporates the following ideas:

- the sky level is a constant to be subtracted from each integration on the source, which varies with time on a scale of roughly 30 minutes. This assumes that gradients across the field are negligible, there being only a DC component to subtract.
- thermal emission from the telescope and optics remains roughly fixed with time.

We therefore image the blank sky once every 4 integrations on the object, spending 20% of the total observing time on blank sky. Each sky frame allows us to estimate the sky level in the source frame immediately following the sky, and subtract this constant value with no additional noise injected. Any variations in the median signal from the 3 subsequent source frames are then assumed to be due to sky variations, and these are subtracted as additional constant levels. Note that the rising and setting moon will add a small component to the sky level variations, most noticeable at shorter wavelengths. This is easily taken into account by our method.

An image of the thermal emission from the telescope and optics is then built up from all the sky frames in a given filter from the entire observing run, once the various DC sky levels have been subtracted. This results in a high S/N image which can be subtracted from all the data.

This method has been checked against the traditional method with sky chopping (50% of the observing time on the sky) for the one object, NGC 3227, for which we used the sky chop. There was no significant loss in noise or calibration accuracy found.

3.1.3 Image rotation

All images were rotated such that North is up and East is to the left. For the MONICA images, the prescription for rotation described in Rigaut et al. (1998) was used, with a rotational accuracy of 0.1°. This involved rotation by -100.4°, followed by flipping over the y-axis. The KIR images were roughly aligned with the cardinal poles already, and only required a slight rotational correction ($< 2°$). We used as a cross-check, any images which had stars in the field to transform to North using the HST optical images.

3.1.4 Calibrations

All our flux calibrations were performed using UKIRT faint standard stars (Casali and Hawarden 1990). In general with AOB corrected PSFs, one has to obtain an aperture measurement by including flux in the aperture far from the central diffraction spike. The halo can be extended easily 1.5 to 2 arcsec, especially if the Strehl ratio is less than optimal ($< 20\%$ at K-band for example). This is easy to take into account, and photometric accuracy of better than a tenth of a magnitude are typical for our observations. The extended halos do however present problems for photometric accuracy within the field, especially for aperture photometry of crowded fields. It is difficult to accurately measure the true colour gradients in extended objects for similar reasons.

If we assume we know the PSF, then we can estimate the error with artificial star fields and Monte Carlo simulations, effectively generating an aperture correction. However, PSF variations across the AOB field make this a lower limit to the true correction.

Possible calibration problems with MONICA and KIR involve the 4 quadrants of the detector, which are biased at 4 different levels or zero points. Although the balance of the amplifiers is not guaranteed, recent globular cluster results (Davidge and Courteau 1998) indicate that the gain is balanced to better than 1% in the 4 quadrants for both cameras.

Flux estimates were derived from the calibrated magnitudes using the prescription in Thuan (1983). This involves convolving the atmosphere-corrected filter responses with the model for the star Alpha Lyrae (Vega) and normalizing to the 0.56 μm flux of Oke and Schild (1981) for a 15th magnitude star: 1.61 mJy at J; 1.02 mJy at H; and 0.65 mJy at K.

Corrections for Galactic reddening (Thuan 1983) follow a simple cosecant law and reddening curve, such as described in Rieke and Lebofsky (1985). The effect is minimal for near-IR colours at reasonably

high Galactic latitude.

3.1.5 Assessing image quality

In the cases where the HST core is unresolved, our resolution estimate is based on the FWHM of the galaxy core in our images. For a resolved HST core, we use the HST FWHM as a guide to the level of correction in the AOB image. In some cases, stars in the field or other unresolved structures are used to estimate the image resolution. The PSF reconstructed from the AOB control commands (see Veran et al. 1998 and next section) tends to underestimate the FWHM of the galaxy core except in the brightest, unresolved nuclei. We therefore do not include this in our assessment of the image resolution.

We note that the PSF degrades away from the guiding source isotropically. The degree of this degradation depends on time, colour, and guide brightness. Models of the off-axis PSF behaviour have been studied by Hutchings et al. (1998), who generate the off-axis PSF from an image of the guide source and a map of the off-axis correction. At a distance of 15″ from the guide source, a well corrected PSF will be degraded to around 0.″3.

3.2 Problems inherent in AOB imaging

Although before the commencement of this study, it was assumed that the behaviour of the corrected point-spread function was well understood in adaptive optics systems, it became apparent through analysis of this dataset that there were in fact several problems inherent in the use of at least the AOB on CFHT, and perhaps other AO systems as well. The first, an artifact associated with bright point sources superposed on a diffuse background, we uncovered through comparison of the core structures in the galaxy sample. The cause of this is still unknown. The second effect is the distortion caused by guiding on certain objects which are not true point sources. This was uncovered largely through comparison with HST-NICMOS data.

3.2.1 AOB artifacts - the difficulty of identifying physical structure

The exciting results on AGN cores emerging from AOB studies are tempered with the discovery of AOB-related artifacts in the central arcsec surrounding the bright nuclei of observed AGN galaxies. These artifacts can masquerade convincingly as the expected types of morphologies in the centers of Seyfert galaxies: small-scale spiral arms, edge-on disks or tori, double nuclei, and outflows.

Table 3.1: Artifacts associated with the AOB PSF

Galaxy	resolution (FWHM)†	artifact (raw)	artifact (model-subtracted)
Seyfert 1			
IC4329a	diff.	trefoil?	ghosts+trefoil
MRK 744	diff.	trefoil,cross?	
MRK 766	near diff.	weak cross, NE offset?	distorted cross
MRK 1330	diff.	cross	strong cross
NGC 1275	0.3″	weak cross	cross
NGC 2639	0.2″	none	none
NGC 2992	diff.	none	trefoil in KIR
NGC 3227	diff.	E elongated	trefoil
NGC 3516	diff.	cross	cross/trefoil/ghosts
NGC 3998	diff.	strong cross	strong cross
NGC 4051	diff.	trefoil?	ghosts/trefoil/irref.
NGC 4151	diff.	trefoil?	ghosts/trefoil
NGC 5033	0.2″	weak cross	trefoil+cross
NGC 5273	0.25″	weak cross	cross
NGC 5506	<0.25″	none?	
NGC 5548	diff.	cross + trefoil?	cross+trefoil
NGC 5728	<0.35″	none	
NGC 6814	0.25″	cross	cross
NGC 7469	diff.	partial trefoil	trefoil
Seyfert 2			
MRK 3	0.3″	weak cross	extended PSF?
MRK 348	0.25″	E lobe	trefoil/extended?
MRK 620	diff. (?)	cross?	extended PSF/cross
MRK 1066	0.2″	none	
NGC 1068	0.25″	cross	strong cross
NGC 1241	0.3″	none	
NGC 1386	<0.25″	none	elongated?
NGC 3081	<0.3″	none	none
NGC 3393	<0.3″	cross?	weak cross
NGC 4968	0.25″	weak trefoil+cross	same
NGC 5005	0.3″	none	none
NGC 5135	0.45″	guiding prob.	3 bright cores
NGC 5929	0.25″	none	weak trefoil
NGC 5953	0.3″	none?	
NGC 7465	0.2″	hints of cross?	trefoil/cross
NGC 7582	0.2″	N extent	cross
NGC 7590	0.3″	none	none
NGC 7743	0.25″	none	weak cross

† Diff. indicates diffraction limited correction – 0.″14 at K-band.
Cross – a 4-lobed artifact, Trefoil – a 3-lobed artifact, Ghost – spurious reflections of the bright central PSF appearing near the position of the galaxy core.

To highlight the underlying artifact structure, residual maps were constructed. First, elliptical isophotes were fit to the galaxy core region using the IRAF task **ELLIPSE**. A smooth model was then built from the resulting fit (IRAF task **BMODEL**), and subtracted from the raw image. Alternatively, images were smoothed with a median filter with box size three times the image FWHM and the results were subtracted from the core with a similar result. The most pronounced effect in all the raw images is an extended lobe to the North, which is emphasized in the residual maps. Figure 3.1 shows a representative sample of AGN cores imaged with KIR, while figure 3.2 shows the same for those imaged by MONICA. The bright regions indicate emission excess above the elliptical model, while dark regions are negative relative to the model. All images are in the K-band where PSF correction is generally best, however the artifact is clearly achromatic, with morphological features lying in identical points relative to the nucleus in J, H and K filters, for a given galaxy. Figures 3.1 and 3.2 clearly show that these structures exist at the same scale with similar shape and orientation relative to North, regardless of Seyfert type or distance to the galaxy. In particular NGC 3998, NGC 3516, and Mkn 348 all show a cross-like (4 lobed) pattern suggestive of small-scale spiral arms plus a bar or edge-on torus, similar to NGC 1068 (figure 3.4). In Table 3.1, we list and describe the artifacts associated with each target galaxy. Column 3 lists artifacts apparent in the raw images, while column 4 lists additional artifacts revealed by the model image subtraction described above.

The KIR K-band image of NGC 3998 is displayed in Figure 3.3, and shows the effect of this cross pattern artifact is visible even in the raw image. The northern component of the cross encompasses more than 10% of the peak of the central core. A similar cross-shape is present in K-band images of NGC 1068 (figure 3.4). This cross structure is visible in the multi-band near-IR AO images of this galaxy presented by Rouan et al. (1998), and Alloin et al. (1998). Such a cross is not observed in the Keck telescope speckle imaging of Weinberger et al. 1999. In this image, there is extended structure, but it lies along the NW-SE axis, between the extended lobes of the AO images. The Seyfert 1 galaxy M81 observed by Davidge & Courteau (1998), also displays such a strong cross pattern, but the skew of the southern lobe is east rather than west as in NGC3998 and NGC1068 (figure 3.5).

A trefoil-type pattern (3 lobes) is visible in many of the galaxy cores, rather than a 4-lobed cross, especially those with a very bright unresolved nucleus. This feature has been identified previously with curvature-based AO systems in the stellar PSF (F.Rigaut, private communication).

Finally, some galaxies with extremely bright nuclei, show ghost images of the bright central PSF from reflections in the optical train in addition to the trefoil pattern (NGC 4151, and NGC 4051 for instance).

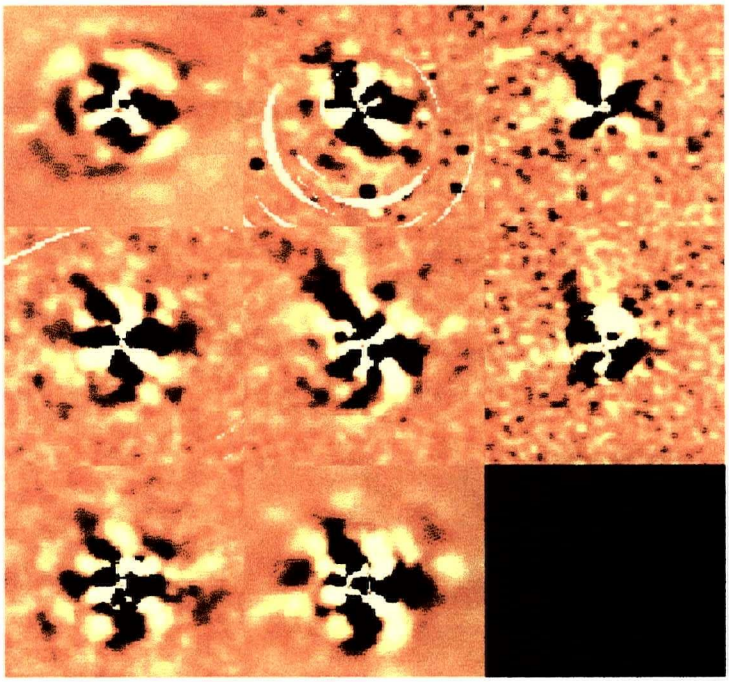

Figure 3.1: Artifacts in KIR model-subtracted K-band images (see text for details). All images are 4″ to a side with north up and east to the left. From left to right starting on the top row: IC4329A, Mkn744, Mkn766, NGC2639, NGC3516, NGC3998, NGC4051, and NGC4151

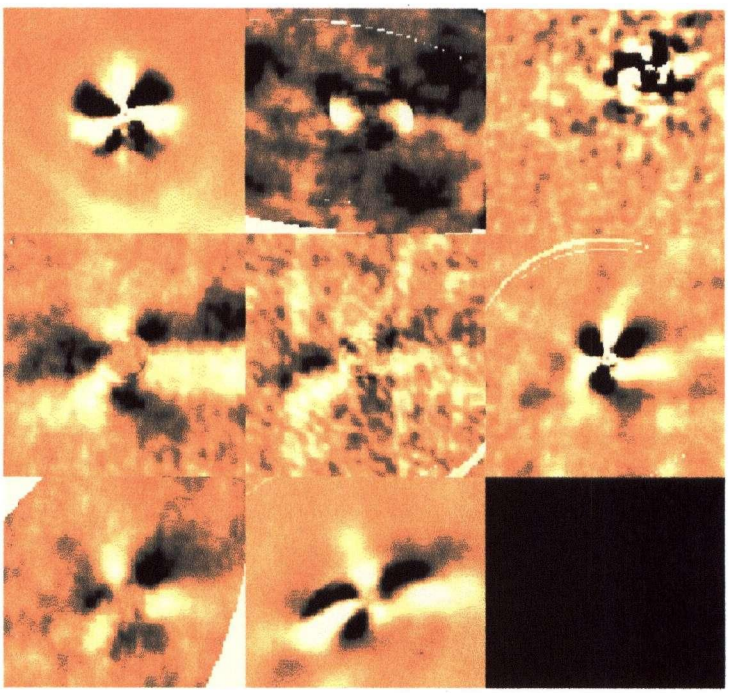

Figure 3.2: Artifacts in MONICA model-subtracted K-band images. All images are 4″ to a side with north up and east to the left. From left to right starting on the top row: Mkn348, NGC1386, NGC3227, NGC5033, NGC5929, NGC7465, NGC7582, and NGC7743

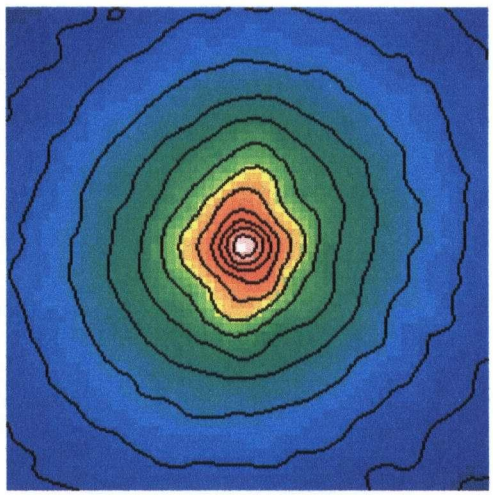

Figure 3.3: Artifacts in NGC3998. Image is 2″ to a side with north up and east to the left. A cross shape is apparent at about the 6th contour level.

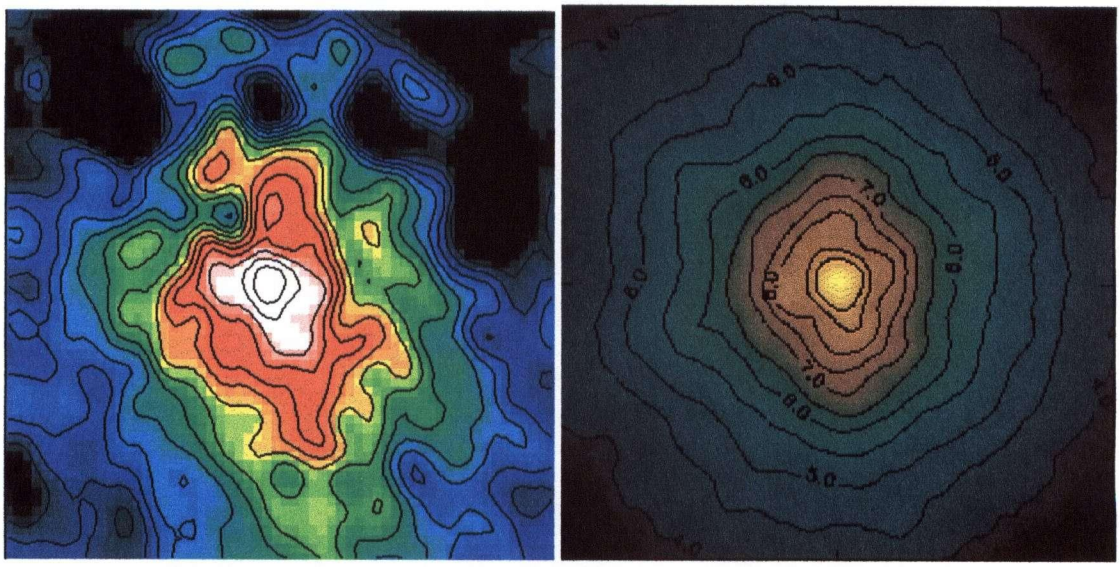

Figure 3.4: Artifacts in NGC1068. Images are 2″ to a side with north up and east to the left. **left panel** Our K-band image deconvolved with the LUCY algorithm (section 3.3). **right panel** K-band image, first presented by Rouan et al. (1998). A similar cross-like pattern is apparent in both images, observed many months apart. This is indicative that it may indeed be the underlying structure in the galaxy which triggers the AOB to distort the trefoil into a cross. The similarity to NGC 3998 (figure 3.3) suggests that the cross distortion resulting from the AOB system cannot be very sensitive to the detailed structure in the galaxy.

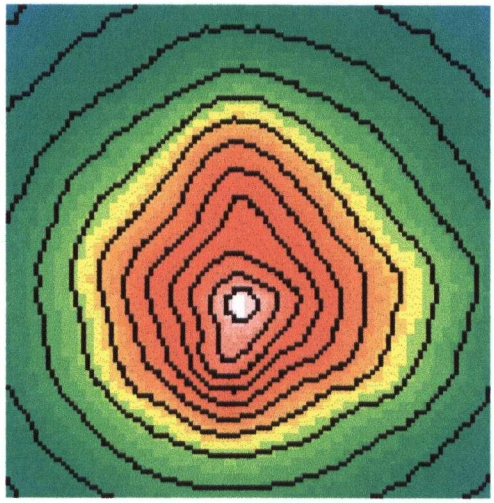

Figure 3.5: Artifacts in M81. Image is 2″ to a side with north up and east to the left. The skew of the cross-shape is more to the east than in figures 3.3 and 3.4, almost giving the appearance of a mirror image.

These can typically be avoided by using shorter exposure times, since the ghosts only become apparent past the saturation point of the bright core.

The artifact structures are most prominent when a bright point source dominates the core, and are less apparent in the weaker or more extended cores, possibly indicating that they are strongest when the AOB correction is at its best. This trend is clear in table 3.1 where many of the cores which have the worst correction or an extended nature do not show any evidence for the cross pattern. However there are certainly examples of strong, unresolved cores which are indistinguishable from a stellar PSF with only the trefoil artifact and no sign of a cross pattern.

The artifact morphology is also not dependent on the camera used with AOB (both the 1024^2 pixel KIR and 256^2 pixel MONICA show identical artifacts, once the images have been rotated to the same orientation on the sky).

None of the stars imaged with AOB for calibration purposes show well defined, extended cross-patterns. On the other hand, the trefoil pattern is always apparent in well corrected stellar PSFs (figure 3.6), and can vary in shape and position in different objects. We find substantial variability in the flux present in the lobes of the trefoil, most notably in the northern lobe. The ubiquity of the trefoil, and lack of the cross, in stellar point source images suggests that the cross pattern may be the result of the extended underlying galaxy, or a combination of the brightest part of the galaxy image on top of the trefoil.

All the above evidence suggests a similar origin for both the trefoil and the cross patterns, since (1) there is always a northern lobe regardless of the other morphology, and (2) following the images in figures 3.1 and 3.2, a sequence could be drawn which gradually transforms the cross into the trefoil. We will keep this possibility in mind as we explore various causes for the artifacts.

We also note that even with these artifacts, the AOB system is reliable in identifying systems such as binary stars or galaxies with true double nuclei, if the relative flux is less than a factor of 10, or if the artifact is carefully taken into account. Knapen et al. (1997) and Lai et al. (1998) appear to have resolved double nuclei at similar angular scales in the starburst galaxies Mkn273 and Mkn231 respectively, which may be unrelated to the artifact and would thus be real structure in the galaxy. The extended core to the West at K-band in Mkn273, however (Knapen et al. 1997), which they attribute to a secondary double nucleus, is very similar to the artifact morphologies observed in our galaxy sample. The achromatic peak to the west of the nucleus in Mkn231 (Lai et al. 1998) may also be related to a weak cross pattern which is accentuated by the deconvolution algorithms applied to the image. We note

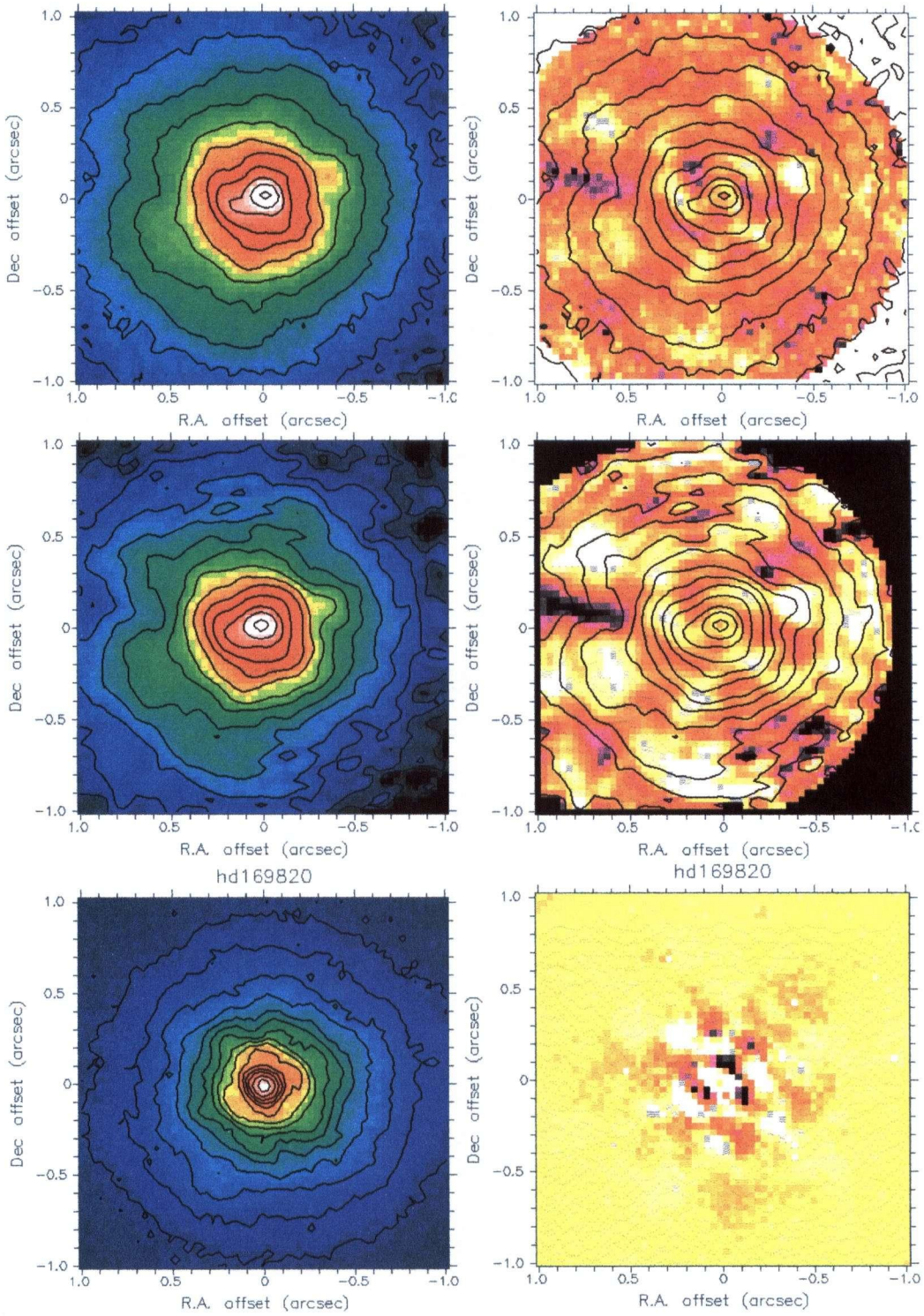

Figure 3.6: **top row** Trefoil artifact within the central 0.″5 of the PSF star FS 23 imaged with the MONICA camera (left), with a residual map (right) obtained by subtraction of elliptical fit contours. Numerous ghost images (reflected images of the star) appear at larger radii. **middle row** Comparison with a reconstructed PSF (see section 3.2.3) using the modal control commands used during the observation of NGC 1275 (left) along with a residual map (right). **bottom row** PSF star HD 169820 imaged with the KIR camera (left) and a residual map (right). Images are 2″ on a side, and contours are logorithmic. The different lobes of the trefoil have variations in flux of order 20%, between the 2 stars.

also that the achromaticity of the artifact means that identifying structures in all three near-IR bands (as applied in Lai et al. 1998) is no longer any measure of its reality in the vicinity of the guide source.

When HST data are available at a similar wavelength, this provides the best check on the reality of any observed structures. NGC 3227 shows evidence for the artifact cross-pattern. The AOB core was compared with HST-NICMOS data (Alonso-Herrero, private communication) and the actual structure beyond the cross was found to be genuine.

Image deconvolution is subject to artifacts, but they are typically wavelength and algorithm dependent (see below). However, in the presence of the multi-lobed artifact structure, all deconvolution methods will accentuate these features if the correct PSF is not used. At the present time, no satisfactory method of obtaining the true PSF in the presence of these varying artifacts is known.

Work on the host galaxies of quasars with AOB imaging is also subject to artifact contamination (see for example Hutchings et al. 1998). Extensions to the central unresolved core could be taken as possible evidence for the expected compact stellar clusters surrounding the nucleus. However, the cross/trefoil patterns appear exactly as extensions to the PSF in the raw image, and a fair range of orientations are produced by a combination of the artifacts. Thus caution should be taken in the direct interpretation of any satellite structure observed around the cores of galaxies.

Caution should also be taken when using binary or elongated systems for guiding sources, particularly where the flux in the two components is comparable. The AOB system will tend to oscillate along the separation axis producing a distorted or elongated PSF, in addition to any possible artifacts. This may have compounded the artifact problem in several of our extended guide sources (see Table 3.1).

Deconvolution techniques may be able to account sufficiently for these artifacts, once their true nature is uncovered. This will allow the central arcsecond of active galaxies to be probed with more confidence using AOB.

3.2.2 Trefoils and possible causes

Although the 4 point cross has never before been observed and identified as an artifact in AO systems, the trefoil pattern occurring in the stellar point sources is not new. Indeed, the trefoil is the outstanding puzzle of AO. It is present in any low order AO system's PSF (F. Rigaut, Private Communication). It varies in amplitude and to some degree in rotation. It seems however to be much reduced in medium to high order systems such as the University of Hawaii curvature-based AO system, Hokupa'a (Close et al. 1998). Currently, there has been no satisfactory explanation proposed to explain this. Some attempts

have been made to simulate AOB with extended objects as guides (Rigaut, in preparation), however in no cases did they lead to any artifacts, trefoil or cross.

In a recent simulation (performed for purposes other than analyzing artifacts), Rigaut (paper in preparation) showed that a decentering between the deformable mirror and wavefront sensor can induce effects, which could in principle resemble such multi-lobed artifacts. However, thus far, the simulations have not produced anything close to the cross patterns seen in our images.

We note that the AOB at CFHT is not the only system to show such cross patterns. The AO system on the ESO telescope at La Silla, Chile, (ADONIS - Beuzit et al. 1997) is based on curvature wavefront sensing, and is similar to the AOB in many ways. The AOB control system was actually modeled on that used in ADONIS. Motivated by our results with NGC1068, we have analyzed the diffraction-limited ADONIS images of the same object in L- (3.1 μm) and M-bands (4.5 μm), presented in Alloin et al. 1998. These clearly show a similar cross pattern as our images and those presented in Rouan et al (1998). We suggest that this is strong evidence for the control system being related to the artifact problem, perhaps interacting with various circumnuclear structures to distort the trefoil pattern into a cross.

3.2.3 PSF reconstruction

A technique has been developed to reconstruct the AOB PSF from the modal control used during the actual observations (Veran et al. 1998). The algorithm requires a fairly bright guiding source (greater than 80 APD counts) to accurately reproduce the PSF, and not all our galaxy cores satisfy this criterion. Reconstructed PSFs for 4 of the model-subtracted galaxies depicted in figure 3.1 (all with bright cores), are shown in figure 3.7 also with a smooth model subtracted. Structures are similar in scale to the actual galaxy data, showing some kind of "lobe" configuration. The actual galaxy counterparts to these reconstructions display a broad range in core morphology from the extremely bright point source in NGC 4151 to the bright but extended Seyfert 2 galaxy Mkn 1066. The reconstructed PSF has essentially the same morphology in all cases, and does not reproduce the actual artifact morphology in the galaxy cores. There is some evidence for a cross-like pattern in the first diffraction ring, but it does not fall onto the same location as the peaks in the corresponding images. However, the reconstruction does not take into account the extended nature of the underlying galaxy and the nuclear core, and would not be expected to reproduce the artifact if it was related to this. The non-common light path to the wavefront sensor and IR array may also contribute to the discrepancy.

Initial versions of the PSF reconstruction algorithm showed that the reconstructed PSFs would

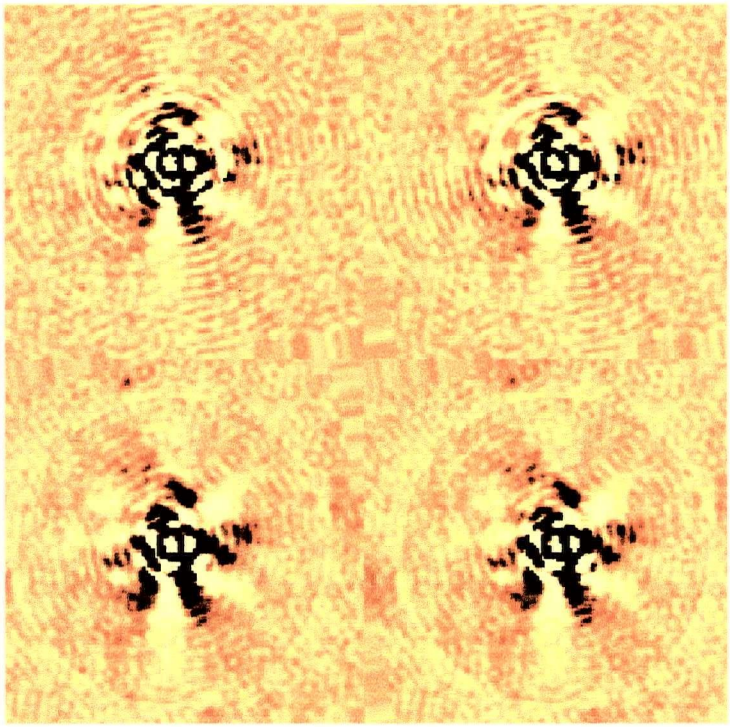

Figure 3.7: Artifacts in reconstructed PSFs for smooth model-subtracted images of (clockwise from top left) NGC4051, NGC4151, NGC3998, MRK1066. Each box is 4″ on a side

sometimes differ from the measured PSF by some low order, slow moving aberrations, such as a triangular coma (J.P. Veran, Private Communication). This triangular coma could not come from the atmosphere since, as it was slow moving, it would have been perfectly corrected by the AO. It could indeed be a non-common path aberration in the AO bench. However an artificial star was used to calibrate the non-common path aberrations and thus should not significantly evolve in time. The only possible explanation would be that this triangular coma originated from a much higher order aberration, which was seen by the wave-front sensor as a triangular coma and improperly corrected as such by the control loop.

This effect is related to aliasing error. Atmospheric aliasing cannot create patterns which deviate from circular symmetry, so these high order aberrations may be due to a very thin turbulence layer, slowly moving across the primary mirror, due to thermal effects. Then, as the structure of this thin layer evolves with time, it would be seen by the wave-front sensor sometimes as a coma, sometimes as a trefoil, and possibly sometimes as a cross pattern. If this were indeed the root of the effect, it should be possible to get rid of it using the image of a point source as calibration instead of the image of the artificial source. Then if the time between the acquisition of the object and the acquisition of the calibration source were relatively small, there would not have been significant evolution of the thin turbulent layer.

We checked this possibility thoroughly with our data. As we noted above, the reconstructed PSF does appear to have associated lobe structure, but this structure is identical in all the galaxy images, whereas the actual core artifacts vary considerably. The morphology of the reconstructed PSF is not identical to the morphology of the core artifacts, for acquisitions taken shortly after or before the reference star used to compute the PSF. In addition, they do not become increasingly different as the time between the acquisitions of the object and the reference source increases. Thus it is not likely that the type of problems mentioned above are entirely responsible for the artifact. However they may be related to the problem, especially given the trefoil similarities in the reconstructions at larger scales, and the cross/ring at smaller scales. If such moving aberrations are found to be a significant effect, then reference point sources should be observed fairly often with AOB observations to let the reconstructed PSF keep up with these moving aberrations. However, the fact that NGC 1068 was observed on two separate occasions with a very similar cross pattern is further evidence that the slow moving turbulence is not the main source of the cross artifact.

3.2.4 The CFHT secondary mirror mount

It is also possible that the artifacts could be related to the 3-point mount of the secondary mirror. The secondary support mount has a 3-point defining mechanism with a vacuum/pressure system which is supposed to keep the system correctly registered but not too tight against the 3 points. If this is not adjusted properly, it may be possible to get a trefoil aberration produced on the images.

The mirror surface must always be continuous, but fairly high order effects could arise if the system were not precisely registered. Curvature wavefront sensing uses defocused images to correct for wavefront distortions (Roddier et al. 1998), and is sensitive to derivatives and not the absolute intensity in the wavefront. Since high order distortions in the mirror surface would approach a *flat spot* in the extreme (i.e. discontinuous second derivatives), the AOB might have problems correcting for such high order effects due to aliasing. This is similar to the situation described in the previous section with slow moving turbulence crossing the primary mirror.

The strong argument against the secondary mirror being responsible for the artifact is the 4-lobe cross pattern appearing in certain cases. Three- or even six-fold symmetry would be conceivable, but four is difficult to explain. Nonetheless, this scenario may be related to the trefoil artifact, and should be investigated further.

3.2.5 Solutions and directions

The cause of these artifacts unfortunately still remains unclear. It is perhaps most plausible that the deformable mirror and control system may be at the root, given the similarities between the AOB and ADONIS systems. The strong feature to the north in most images is also suggestive that certain deformable mirror actuators are continually being driven in response to diffuse structure surrounding the bright nuclear point source. However, this could not explain the presence of the northern lobe of the trefoil pattern for stellar point sources.

The possibility that guiding on a somewhat extended object may not always provide a stable lock for the wavefront sensor is certainly real, given the number of bright, but extended sources we were unable to lock onto for more than several seconds. Such an unstable guiding lock might induce the deformable mirror to try correcting for a strong aberration that is too high a mode for it. But again, this could not explain all artifact situations encountered.

If the secondary mirror is the problem then artifacts should not appear in the University of Hawaii

AO (UHAO) results, unless the UH 88 inch telescope had a secondary mirror support which was similarly out of adjustment. Certainly it is conceivable that any such mirror mount would be out of adjustment at a level which would lead to a trefoil pattern when detected by a sensitive AO system. The fact that the trefoil is smaller with UHAO could be evidence for either a mirror mount in better adjustment, or a higher order correction in the AO system. Alternatively, the artifacts could be of different origin in the two systems. It would be of interest to observe NGC 1068 with the UHAO and carefully compare with the AOB results.

Defocusing the science camera and re-observing some of the objects with the most prominent artifacts might be useful to see if the artifact lobes grew with the amount of defocus. This might imply some problems with the decoupling of the tip-tilt mirror from the deformable mirror, whereby the dynamic range of the deformable mirror was reduced, limiting its use for higher mode correction. A similar situation might arise if the dynamic range of the deformable mirror was taken up with excessive focus compensations. The latter has been observed during our CFHT runs.

Also, the tip/tilt mirror (or some mirror in either the wavefront sensor path or the science path) could be oscillating. If the axis of any of these mirrors lined up with cardinal directions (NSEW), the cross pattern might be produced. In this case, however, we would expect the cross shape to be broader near the source and get narrower as you move away, which does not appear to be the case in our images. Traditionally one would think of something like a cross shape as a diffraction pattern off the telescope struts supporting the top end. This cannot be completely ruled out either.

Further modeling of the response of the curvature based wavefront sensing AO system will probably be required to ultimately ascertain the root of such structures. In the meantime, the analysis described here has certainly underscored the need to exercise caution when interpretting faint structures in AO images.

3.3 Deconvolution

The correction of AOB images is never perfect and the long exposure images acquired with an AO system are still affected by a residual blur which reduces the contrast of the fine details. This residual blur is of course much less severe than the aberrations in the uncorrected images and may be further reduced by means of data processing techniques. Deconvolution provides a means to invert the PSF blurring of the image.

Any image (I) formed as a result of passing through some system, is the result of the convolution of the object (O) and the impulse function of the system (PSF):

$$I = O * \mathrm{PSF} + b,$$

where b is the noise added to the image (Andrew & Hunt 1977). Without any noise component, the equation is easily inverted and our problem is solved. When the signal to noise of the image is large enough (the high frequency components of the image are dominated by the signal, since these are the ones which will be amplified in the inversion process), we can use direct deconvolution methods. In this case the flux is conserved and the photometric accuracy is preserved, given that it is a linear technique. For scientific studies where morphologies are the primary driver rather than photometric colours, we can use non-linear iterative techniques such as the well known LUCY algorithm (Lucy 1974) and its variants. These non-linear algorithms typically do not conserve the relative flux of various components in the image.

Magain (1997) has shown that a deconvolution algorithm using a PSF with better resolution than that in the actual image produces optimal results, which are photometrically accurate. For AOB observations of extended galaxies, this is in effect our only alternative given that the PSF reconstructions or estimates typically have a smaller FWHM than the actual PSF in the galaxy core. Nonetheless, for our scientific results, we avoid relying exclusively on photometry originating in deconvolved images.

A brief summary and discussion of the deconvolution techniques used is presented in the following sections. The outcome of the deconvolution can depend critically on the methods employed for the different types of structures seen in our galaxy sample. These range from smooth distributions to small point structures and extended structures, to an image dominated by a bright central point source.

3.3.1 Direct deconvolution

This technique consists of a direct inversion of the above equation. In the fourier plane, the equation becomes:

$$O(\nu) = \frac{I(\nu) - b(\nu)}{PSF(\nu)}$$

with $\nu = 2\Pi/\theta$ is the spatial frequency. The fourier transform of the PSF is the modulation transfer function (MTF) of the system (telescope+atmosphere+AO). The MTF falls to zero (to within the noise) at the cutoff frequency of the telescope (where the cut-off frequency is $\nu > \nu_0 \sim D/\lambda$). There is only noise at frequencies larger than the telescope cutoff frequency in the Fourier transform of the image.

Thus we see that a direct division of the above equation results in noise domination for $\nu > \nu_0$. To deal with this problem requires that the highest frequencies be suppressed with a low-pass filter.

To overcome some of the problems inherent in direct deconvolution, non-linear iterative algorithms have been developed. The Lucy-Richardson algorithm (Lucy 1974), used to deconvolved our AOB data, generates a restored image through an iterative method. The essence of the iteration is as follows: the $(n+1)$th estimate of the restored image is given by the nth estimate of the restored image multiplied by a correction image.

3.3.2 Structures formed and revealed by deconvolution

We would like to be able to discriminate carefully between structures which are artifacts of the deconvolution process and structures which are inherent in the galaxy which have been sharpened by deconvolution. This requires a thorough understanding of the mechanisms involved in the deconvolution process which might lead to spurious structure identification. Three separate issues should be considered:

Noise

Various residuals from the preprocessing stage may become amplified by the deconvolution: remaining bad pixels or cosmic rays, flat-fielding, and correlated noise. These features are, respectively, very localized, of fairly low frequency, and periodic. The cosmic rays are perhaps the most troublesome, becoming point source-like in the deconvolved image, and may be mistaken for a knotty or unresolved feature. None of these features would lead to erroneous identifications of the torus or disk-like structures hypothesized in AGN models, however.

Number of iterations

With the non-linear, iterative procedures, it is difficult to know when to stop the deconvolution process (i.e., after how many iterations, or at what cut-off frequency). We can attempt to impose somewhat subjective criteria on the resulting image: the deconvolved image must have some minimum deviation (i.e., 1σ) from the original image when convolved with the PSF.This is still unsatisfactory, as it relies on the noise present in the original signal. For the case where the image has excellent signal to noise, it is easy to deconvolve and obtain a "super-resolution" image, beyond that of the diffraction limit of the telescope. However, there is clearly no new information in such a result.

Some of these ambiguities can at least be reduced through the use of multiple algorithms for deconvolution, since each reacts differently to the noise. Structures which appear in images deconvolved with different methods are more likely to be real, than those seen only using a single algorithm. The risk of "super-resolution" is reduced if the noise is limited by the number of iterations.

In all cases, we have the identification in more than one filter as a first check on structure reality. For example, NGC 3227 shows a series of point-like knots circling the nucleus down at the range of the brightest diffraction rings. They appear prominently in J,H,K and V band images and are likely related to star-formation (see chapter 5)

Estimation and quality of the PSF

The problem of assessing the PSF and its stability is difficult to overcome, especially in the case of diffuse galaxy cores used as guiding sources. In general there are two possible evolutions:
a) if the conditions are relatively poor, the modulation transfer function will stretch further in frequency, and the deconvolution will amplify these frequencies in the image – i.e., amplify the noise.
b) if the conditions improve during the acquisition of the object, we do not reproduce the high spatial frequencies with the deconvolution. The deconvoled object will then be dug out around the point-like structures, to compensate and augment the contrast. With this, it is easy to create rings, and the effect will be the same for all algorithms.

We therefore must be cautious in the interpretation of any observed structures without careful cross analysis between filters, and use of the photometric colours to help separate the deconvolution artifacts.

With all these warnings about the dangers of over-interpretation of AO images, and suggestions for how to be confident about the reality of faint structures, we are now ready to tackle the data for the best-studied AGN.

Chapter 4

Individual objects - I. NGC 2992

The structures in the core regions of active galaxies are clearly of enormous interest for the paradigms of AGN research, as outlined in chapter 1. However, identifying structures and their function in the cores of galaxies using broadband imaging data alone is a difficult task. In the following chapters, we have chosen two galaxies from our sample to study in detail through comparison with other wavelength data, including HST optical, VLA radio interferometric, and larger scale near-IR.

4.1 Introduction

NGC 2992 is an Sa galaxy seen almost edge-on with a nearby, likely interacting, companion (NGC 2993). It possesses an active Seyfert 1.9 nucleus. A large and prominent dust lane runs through the center of the galaxy roughly north to south, splitting the nuclear region in two. Ulvestad and Wilson (1984) found that the radio structure of the nucleus of NGC 2992 has the shape of a "figure-8", with a maximum extent of about 550 pc, oriented out of the plane of the galactic disk (assumed distance 37.3 Mpc using the recession velocity relative to the Local Group of $1864\,\mathrm{km\,s^{-1}}$ (Ward et al. 1980) and $H_0 = 50$ km $\mathrm{s^{-1}Mpc^{-1}}$, angular scale of 182 pc / 1″). Most of of the 6cm radio emission from the center of the galaxy arises in the loops of the figure-8 rather than in the nucleus.

There are several favored models for such figure-8 radio emission. The loops could result from expanding gas bubbles which are seen preferentially as limb-brightened loops (Wehrle et al. 1988). Such outflows may be associated with the AGN core. The continually diminishing X-ray emission has been interpreted as a dying active nucleus (Bassani et al. 1998), possibly because fuel is no longer being channeled down to an accretion disk region. However, this would not likely affect the appearance of the surrounding region at our resolution of ~20 pc since even at outflow speeds close to c the timescale is ~ 50 years.

Alternatively starburst driven superwinds could result in expanding gas bubbles leading to such emission (Heckman et al. 1990). Extended X-ray and Hα emission (Colbert et al. 1996, Colbert et al.

1998) perpendicular to the plane of the galaxy may be an indication for the superwind. If the superwind were produced by an energetic burst of supernovae in the past, the current radius of the loop would then imply that the SNe explosion occurred over 2.35×10^5 years ago for a typical expansion velocity of 1000 km/s (Koo et al. 1992, Tenorio-Tagle et al. 1998).

A different model proposes toroidal magnetic fields which result in a loop-like emission of synchrotron emission (Wehrle & Morris 1988). Here, strong differential rotation in the galactic nuclear disk builds up the magnetic field having some radial component, until an instability occurs leading to an expanding magnetic arch. The field configuration upon expansion away from the nucleus is then a pair of loops. The synchrotron emission results when particles are accelerated to relativistic energies in the magnetic arches.

Our new high resolution imaging in the near-IR unveils emission features (dust obscured in optical wavelength HST imaging) which may be related to the VLA radio emission. This discovery allows a consistent model of the radio emission to be formulated, incorporating the larger scale bi-polar morphology observed in Hα by Allen et al. (1998).

4.2 Observational Details

4.2.1 CFHT AOB imaging

The core of this galaxy is sufficiently bright as a guiding source to enable near diffraction limited resolution under favorable natural seeing conditions. We obtained an H-band image with MONICA under good observing conditions (seeing FWHM $< 0\farcs6$ resulting in $0\farcs15$ resolution. The J, H, K- band and narrow-band CO images obtained with KIR had worse natural seeing ($>0\farcs9$) and the corrected PSF has a FWHM of $\sim 0\farcs45$ at H and K, and $\sim 0\farcs60$ at J.

The continuum image for the vibrational transition CO(2-0) absorption ($\lambda_c = 2.296\,\mu$m $\Delta\lambda = 200$ Å) was estimated by fitting a line to the average flux as a function of wavelength, within the disk of the galaxy, for the J, H, and K images. This extrapolation was then sampled with a Gaussian of the same width as the CO narrow filter centered at 2.296μm. This flux level was then used to normalize the K-band image for subtraction of the CO image. The outer regions of the image have normal stellar colours and are likely to be relatively free of dust emission. Thus the above procedure was checked by matching the continuum image in flux to the CO image at this point becoming the zero-point in the [continuum - CO] image.

Obtaining an accurate measure of the resulting PSF of the image with AO is problematic, since the atmospheric conditions are continually changing, and a stellar image taken before or after the science exposure will likely not resemble the PSF of the science frame. An accurate PSF must be temporally and spatially coincident with the actual region of interest in the field, since the PSF degrades away from the guiding source. Even when there is a star within the relatively small field of view of the near-IR cameras used with AOB, the PSF is frequently quite different from the core of the active galaxy (guiding source). Attempts have been made to model the off-axis PSF in these cases with some success (Hutchings et al. 1998).

A technique has been developed to reconstruct a model PSF for the nuclear region of the galaxy using the adaptive optics modal control loop information obtained during the actual observations (Veran et al. 1997). For the core brightness as seen by the wavefront sensor (V=16.5) in the MONICA H-band image, simulations have shown that the reconstructed PSF should match the true PSF to an accuracy of approximately 10% (Veran et al. 1997). The factors degrading such a reconstruction are mostly the faintness and extension of the particular galaxy core, and superior results are obtained with brighter, point-like galaxy nuclei (or stars). The error in our reconstruction is mostly in the Strehl ratio and outer artifacts with the FWHM being very close to that of the actual PSF.

The image is then deconvolved to the point at which the LUCY algorithm (Lucy 1984) converges ($\sim$25 iterations), using the model PSF as input. The LUCY deconvolution can create ringing artifacts around bright unresolved galaxy cores. However the core of NGC 2992 is extended while many of the structures surrounding the core are point-like. This is ideal for LUCY since the core region consists essentially of point sources superposed over a varying background. The algorithm was found to provide a believable deconvolution, with no new features appearing which were not in the original image at some level. The estimated final resolution in the image is 0.″12 corresponding to 4 pixels.

4.2.2 Existing HST and UKIRT data

An archive HST F606W filter image was obtained with the WFPC2 camera in 1994 as part of a snapshot survey of nearby active galaxies (Malkan 1998). The pixel scale with the PC camera is 0.″044 per pixel. In order to compare this directly with our AOB image, we have interpolated and rebinned the image after rotating it to the proper orientation. The prescription to calibrate the HST F606W image to Johnson V-band as outlined in Malkan et al. (1998) is used for NGC 2992.

NGC 2992 was also observed at the United Kingdom InfraRed Telescope (UKIRT) in the near-IR

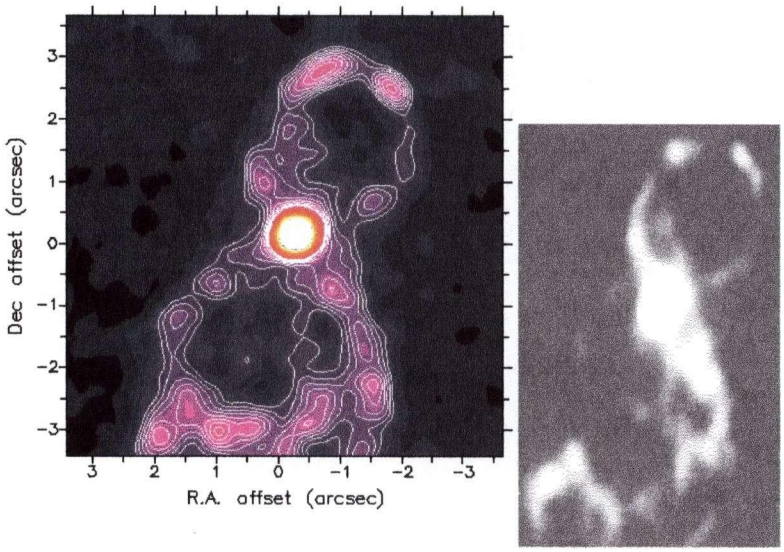

Figure 4.1: Top: 8.4 GHz image with contours overlaid (Peak flux: 7.0 mJy - contour levels from 0.14 mJy to 0.54 mJy, with intervals 0.045 mJy). Bottom: reproduction of the 5 GHz image (Wehrle and Morris 1985) (Peak flux: 7.2 mJy). The peak flux at 1.5 GHz is 27.8 mJy (Ulvestad & Wilson, 1984)

bands J, H and K. The plate scale is 0.29″/pixel. These data were originally presented by Alonso-Herrero et al. (1998).

4.2.3 VLA radio maps

A VLA image at 6 cm (5 GHz) was obtained in 1987 by A. Wehrle and is reproduced here with her permission (figure 4.1, right panel).

An image at 8.4GHz (3.57cm) was also obtained from the VLA archive (courtesy of H. Falcke) in C-configuration which resolves more clearly into knot-like structures (figure 4.1, left panel).

4.3 Results

The morphology in the central region of NGC 2992 is a complicated superposition of various components, appearing most prominently in different wavelength regimes. In Table 4.1, we list the various structural components in the core along with the figure which best highlights the feature.

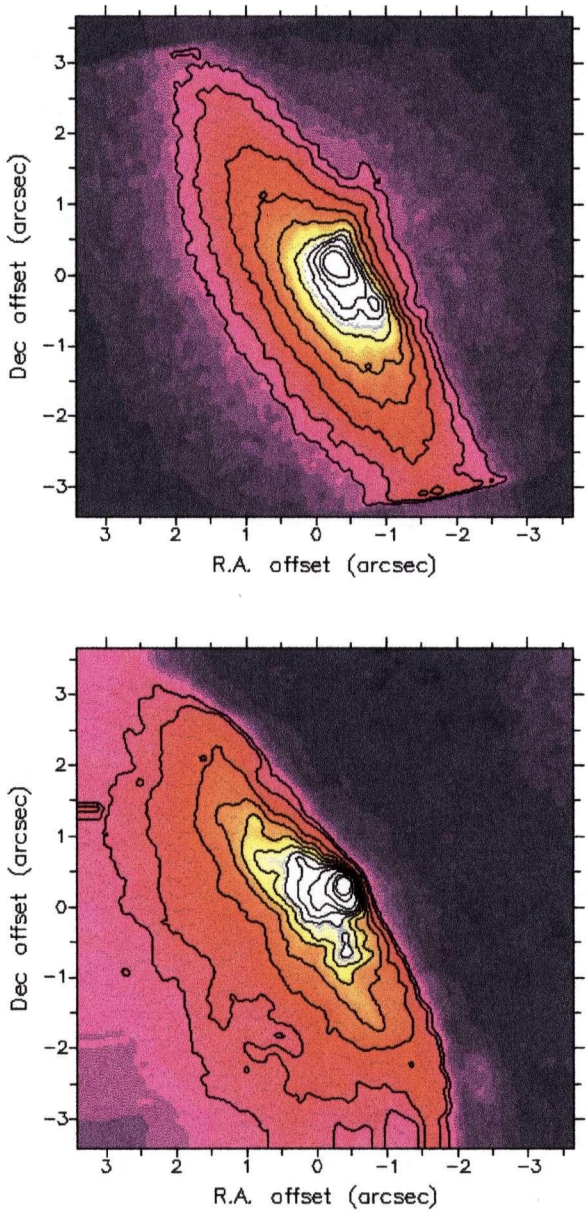

Figure 4.2: Upper panel: CFHT/AOB H-band image deconvolved with the LUCY algorithm. Lower panel: HST F606W (R+V band) image - subsequently called R-band. Contour levels are 1,3,5,8,11,15,20,30,50,80 percent of peak (H=14.1, F606W=17.7).

Table 4.1: The structural components of NGC2992

Feature	property	flux	size	best figure	location
resolved core	SF+AGN	H=13	0.3″	All	
knots near core	SF	H=16	unresolved	raw, smooth (4.2,4.5)	S of nucleus
radio loops			2″	8.4&5 GHz (4.1)	NW,SE
near-IR extension	nonstellar colours	H=15.3	1″	model subtract (4)	NW
inner loop	SF		1″	R-H (4.3)	N
diffuse radio	SF		1″	radio (4.1)	N
spiral arms	knots		3+″	model& smooth (4.4,4.5)	NE-SW
assoc. radio?			3+″	radio (4.1)	NE-SW

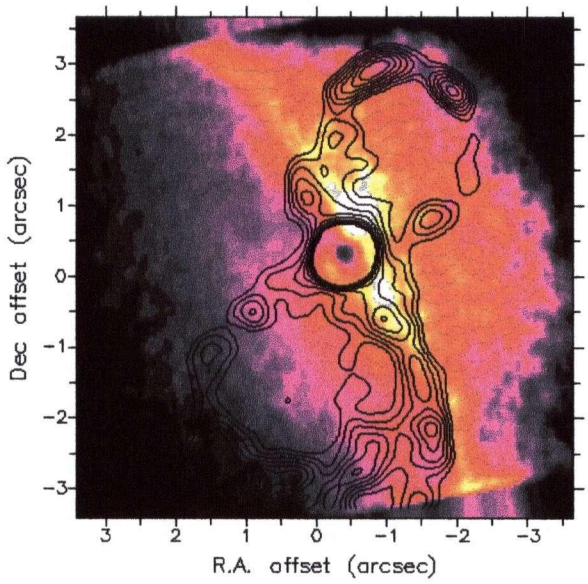

Figure 4.3: R-H colour map with 8.4 GHz contours overlayed. The radio map core centroid was registered to the near-IR core. Brightest colours indicate the reddest regions with a maximum of R-H=4.8, where the nucleus R-H=3.6.

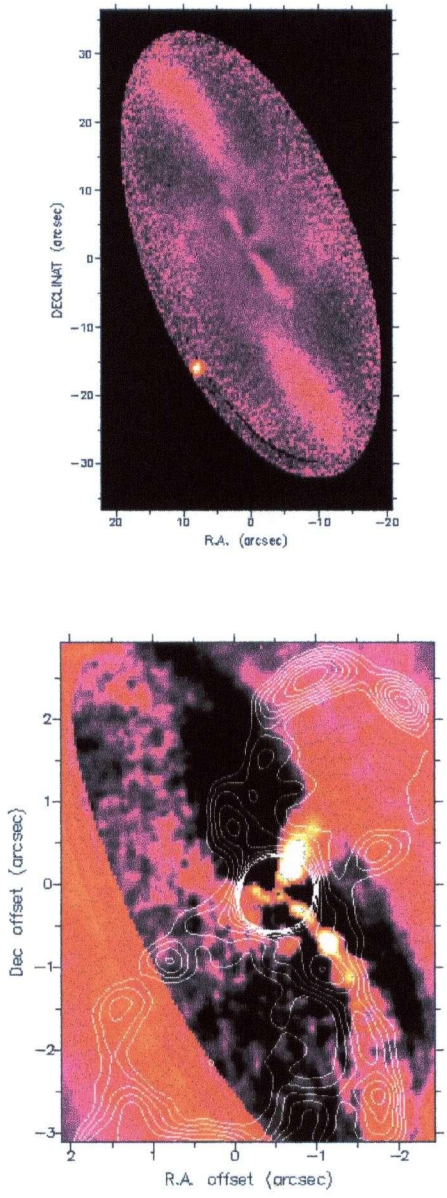

Figure 4.4: a) above: large-scale H-band UKIRT image with 0.″29 pixels, elliptical isophote model subtracted. b) below: AOB H-band isophotal model-subtracted image of the central 6″ × 4″ of NGC 2992 with 8.4 GHz contours overlaid.

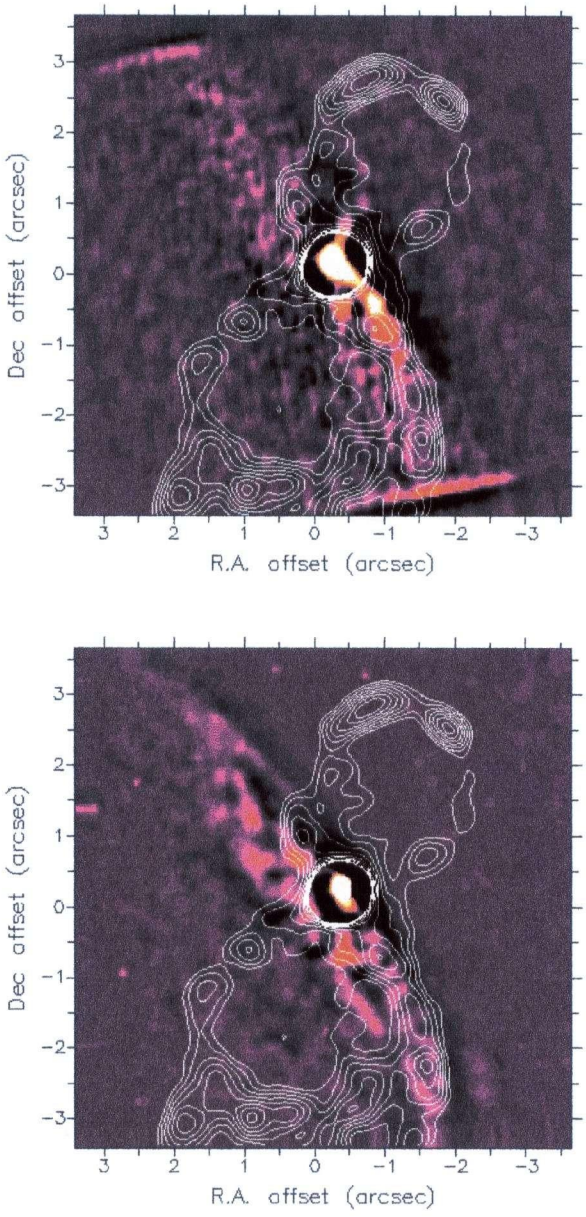

Figure 4.5: N2992 at H (above) and R-band (below), where a median filtered image has been subtracted to remove the contribution of the low order galaxy component. The 8.4 GHz radio contours have been overlayed.

Table 4.2: Aperture magnitudes for the AOB H-band image, and HST F606W filter image corrected to V-band.

Aperture Diameter	H(deconvolved)	H(raw)	V(HST)
0.″5	14.08	14.50	17.46
1.″0	12.84	13.16	16.71
1.″5	12.29	12.50[a]	16.22
2.″0	11.96	12.08	16.17
3.″0	11.56	11.57[b]	16.14

[a] H = 12.57 from Alonso-Herrero et al. 1998
[b] magnitudes agree past the 3rd Airy ring

4.3.1 The Core Region

In figure 4.2 we present the near diffraction limited H-band image of the central 7″ of NGC 2992. The HST F606W (covering V+R band - hereafter called R) image is also depicted. The galaxy core is resolved in both the H and R filters, with a FWHM ∼0.″26 corresponding to 47.2 pc. For the mediocre correction in the KIR J and K images the core is essentially unresolved with FWHM 0.″45 (K) and 0.″6 (J). We estimate the contribution to the extended galaxy core from the unresolved H-band component. Our model-constructed PSF (see section 2 and Veran et al. 1998) is a reasonable estimate of the true PSF for the diffraction limited H-band image. We first produce a surface brightness profile of the galaxy, and another one for the PSF. The PSF is then scaled to match the peak of the galaxy brightness. Both profiles are integrated out to a radial distance of 1″ with the result that the an unresolved component contributes 38% at H in a 0.2″ diameter aperture, and 17% in a 0.5″ aperture.

In Table 4.2 we present aperture photometry of the core region. The V-H colour of the nucleus (V-H = 3.4) is typical for a reddened stellar population (Glass & Moorwood 1985). Note that the deconvolved magnitudes agree with the raw data at an aperture radius of 3″. This would be as expected given that the deconvolution process restores flux to the central spike from the surrounding pedestal. This is encouraging despite the claims that deconvolved images may not be appropriate for photometry since the non-linear algorithm does not necessarily conserve flux (Magain et al. 1998). The disagreement with Alonso-Herrero et al. (1998) for the H-band apertures less than 3″ diameter is likely a result of the improved resolution of our image coupled with our absolute errors of 4% for the RMS of calibration star measurements throughout the observing run.

The radio core spectrum is flat to within 5% measured from our 8.4 GHz VLA image, in conjunction with archive 5 GHz and 1.5 GHz VLA measurements (mean of $\nu F_\nu = 3.4 \times 10^{-16} ergs\, s^{-1}$) Wehrle et al. 1988, Ulvestad et al. 1984. This is indicative of synchrotron emission arising in the AGN core dominating over any possible synchrotron emission associated with supernovae at these wavelengths (Robson 1996).

Examination of the cores in both optical and near-IR images (figures 4.2, 4.4 and 4.5) reveals a bright point-like knot to the south ~110 pc (0.6″) from the nucleus of the galaxy. A second knot to the southwest appears in the near-IR only. An [R-H] colour map is formed by first convolving the HST image with a Gaussian of width 0.″12 to match the AOB resolution. The colour map (figure 4.3) reveals the southwestern knot is almost one magnitude redder in R-H than the southern knot, likely as a result of dust. The SW knot is completely obscured in the HST image. We find the colours in these regions (V-H = 3.6 to 4.2) are consistent with reddened stellar populations.

We perform aperture photometry on these knots in H-band and find apparent magnitudes between 16.0 and 16.5 at H depending on aperture size used (the aperture measurements have relatively large error due to their proximity and overlap with the central AGN core). At the distance of NGC 2992, the absolute magnitudes lie between −15.3 and −14.8 which are comparable to the luminosities of stellar clusters detected in the interacting galaxy Arp299, which have an average H-band absolute magnitude of $H = -15$ (Lai et al 1998b, Alonso-Herrero et al. 1998). Arp220 (Scoville et al. 1998) also has compact stellar clusters of similar luminosities at 1.6μm (H-band). In the latter work, merger remnants have been suggested as an explanation for such bright knots near the galaxy core (> 10% of the AGN peak for NGC 2992).

4.3.2 Spiral Structure

The H- and R-band images (figure 4.2) show elongated isophotes to the southwest along the galaxy disk, and extending east from the nucleus. In the R-band case the galaxy morphology is much more distorted due to the effects of dust. These extensions and distortions in the isophotes suggest structure underlying the elliptical symmetry of the disk within the central regions of galaxy. We subtract a model image of the galaxy for both a large-scale H-band image (60″× 60″) and the AOB H-band image. The model is built from either elliptical fitted isophotes (figure 4.4), or a running median filter image of FWHM twice the resolution (figure 4.5). The elliptical isophote model has the advantage of highlighting structures deviating substantially from elliptical symmetry, while the median filtering tends to bring out fainter point-like structures. The profile in ellipticity (E) and position angle (PA) of the isophotal model shows

that this region has a substantial twist in both E and PA. In figure 4.4 (upper panel), the model subtracted large-scale image displays what appears to be a spiral structure along the disk, as well as a $\sim 3''$ extension to the west, also noted in Alonso-Herrero et al. (1998). Our new high resolution images show that both the spiral structure and western extension can be traced down to the very core. This latter extension will be taken up in the next section.

The image of the larger-scale galaxy shows a break in the spiral structures at $\sim 7''$ radius. This may indicate nested structures which are kinematically distinct, as in the multi-level spiral arm structure observed with adaptive optics in NGC 5248 (Laine et al. 1998). Indeed, the knotty morphology of the spiral structures seen in the AOB and HST images of NGC 2992 are suggestive of star formation in spiral arms. The high inclination of NGC 2992 makes deprojection unreliable and it is difficult to discern how these larger- and smaller-scale spiral structures relate. By the same measure, it is also difficult to know whether the isophotal twists in the core may be due to a bar, a triaxial bulge seen in projection, or simply the effect of the spiral arms (Friedli et al. 1996).

In figures 4.4 and 4.5, the 8.4 GHz radio contours are overlayed on the model-subtracted images. There is clearly some radio emission coincident with the southern spiral arm, which breaks up into a similar knotty morphology to the H-band model-subtracted image. Note especially the strong near-IR peak at the southern tip of the spiral arm has an associated peak in the radio, $\sim 3''$ south and $2''$ west of the nucleus. We find the radio spectrum to be steeper along the spiral arm to the south than in the core, possibly indicative of star formation.

The prominent southern knots near the core, outlined in the previous section, clearly lie along the southern spiral arm. By comparing the brightest knots within the spiral arms in the optical and near-IR images, it appears that the nuclei of the galaxy in H- and R-bands, determined by centroiding on the cores, do not line up precisely. The knots in the southern spiral arm, revealed in the model subtracted images, have similar geometric configurations in the two filters (H and R), but when these are superposed, there is a an (x,y) offset of ($0''.3$, $0''.15$) between the nuclei corresponding to a distance of ~ 70 pc. A true offset is possible due to dust obscuration and/or extended unresolved starbursts (see for instance NGC 1068 (Alloin et al. 1998 for a similar case). Given the much more distorted nuclear region in the HST R-band image compared to the H-band, such a scenario is plausible. However, the spiral arm morphology may be slightly different in the two wavelengths, due to the effects of both dust and unresolved, blended structures.

4.3.3 Figure-8 Loops

There is little sign of optical or near-IR counterparts to the radio loops out past the disk of the galaxy, even at K-band where the ability to see through the dust lane is greatest. However, as noted above, there is an extended feature to the northwest, observed as extended contours in the near-IR (figure 4.2) and as a prominent feature in the model subtracted near-IR images (figure 4.4), extending $\sim$1.5″ before becoming more diffuse and mixing with the stellar emission on the western side of the dustlane. In the optical HST image (figures 4.2b, 4.5b), there is no sign of this extended feature, likely due to the dust lane obscuration. This extension aligns with the mouth of the northern radio loop and appears to continue outward to fill the loop, indicating that the radio loop source may be connected to this feature.

Figure 4.3 shows that the extended feature is the reddest region in the central 7.″0 of the galaxy with an R-H colour of 4.5. The lower resolution KIR images in J,H,K show that the colours in this region clearly stand out from the surrounding disk colours, possibly as non-stellar (J-H=0.5, H-K=1.0). These colours may be related to a highly reddened ($A_V > 5$) burst of stars, possibly with a nebular component. However they are also consistent with a reddened continuum power-law emission (Glass & Moorwood 1985).

Artifacts associated with the AO correction have been shown to produce extensions to the PSF when guiding on extended objects such as as Seyfert nuclei (Chapman et al. 1998). Although caution must therefore be taken in associating such a structure with a physical interpretation, we have compared our AOB H-band image with an HST NICMOS K-band image, and found the same extended isophotes to the west of the core.

4.3.4 Diffuse Inner Loop

The R-H map (figure 4.3) shows extended red emission which takes on a loop-like morphology extending north of the nucleus from the 1″ to the 2″ declination offsets, an enhancement in H rather than a deficit in R. It does not appear to be associated with the spiral arm further to the east. In the median filtered H-band image (figure 4.5), it is also possible to discern knotty features in a loop-like morphology, however the emission lies deep within the dust lane and no counterpart is seen in the model subtracted R-band (figure 4.5).

The 8.4 GHz radio contours superposed over the above figures (4.3 & 4.5) reveal a similar loop-like diffuse emission embedded within the larger, well defined radio loop. The spectrum (from 5GHz/8.4GHz)

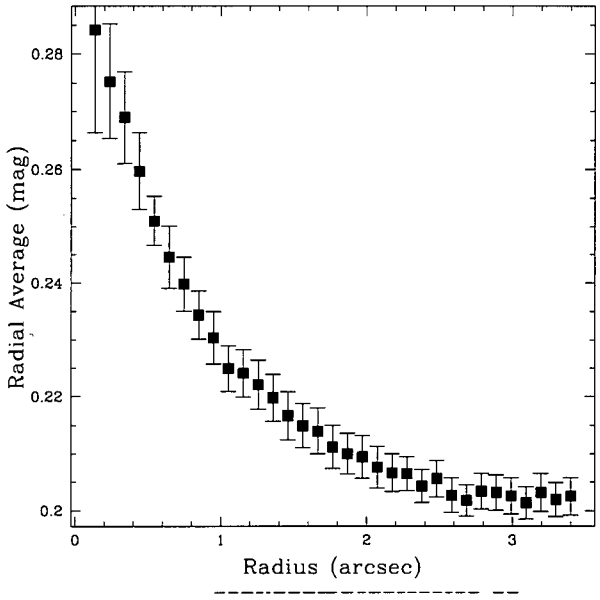

Figure 4.6: The CO index profile, (ctm - CO), near the center of NGC2992, where distances are measured with respect to the galaxy nucleus. The data points are azimuthal averages, and the error bars show the systematic errors introduced by uncertainties in the background.

is steeper here than in the core, consistent with star forming regions. Buried star formation regions have been identified in the dust lane crossing the nuclear region of Centaurus A (Schreier et al. 1996,1998), using HST-NICMOS images in H-band. The J,H,K colours in this region of NGC2992 however are difficult to interpret with the dust absorption gradient across the dust lane. It is not clear that the structure has a true *loop* morphology, and may be simply a result of the way the dust lane cuts through the core region. However, the coincidence of the radio emission suggests that the near-IR excess may represent more than the artifact of dust absorption.

4.3.5 The CO map

The radial distribution of the CO index, (continuum – CO), is shown in figure 4.6, where the plotted values are azimuthal averages in 0.1″ bins. Although the CO(2-0) filter used corresponds to the standard photometric index (2.296 μm center, 200 Åwidth) (Doyon et al. 1994), the subtracted continuum was extrapolated from the broad band colours (see section 4.2). There is then likely a systematic offset in absolute photometry, and we use caution in interpreting the CO magnitudes.

When $r < 1.5''$ the CO index strengthens implying much more CO absorption within the central

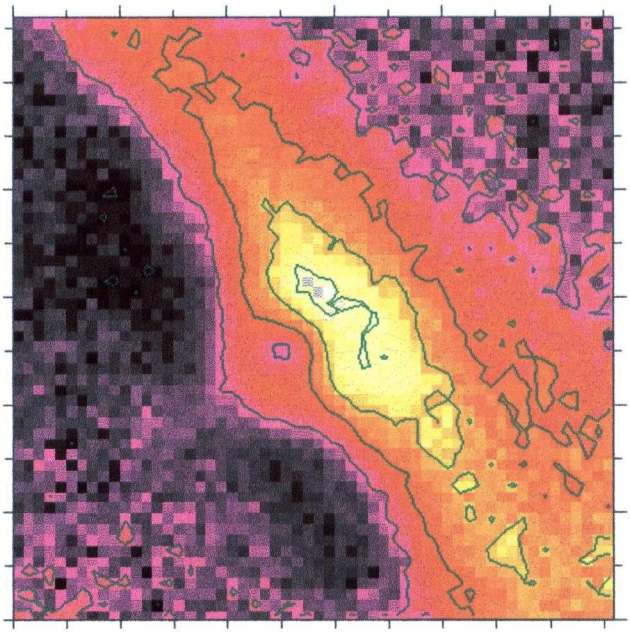

Figure 4.7: NGC2992 H-K map, central 5″, pixels binned to 0.″1. Contour levels are 2.6, 4.6, 6.6, 8.6 magnitudes of visual extinction A(V)

3″. The CO index depends on both the metallicity and the age of the stellar population (giants versus supergiants), and has been found to be difficult to model. If we assume that the metallicity is constant within the center, then the variation may be an age effect. In general, the CO index increases as the starburst ages (Vanzi, Alonso-Herrero & Rieke 1998, Doyon et al. 1994). The NGC2992 CO profile suggests that a somewhat younger population is present in a ring around the galaxy center, while the stellar population in the very core would be slightly older than the surroundings. Given the rather poor resolution in these images (0.45″), we are unable to discern at what level the stellar population contributes within the resolved 50pc core, evident in the HST R- and MONICA H-band images. However, it is clear that hot dust ($\sim$ 1000 K) emission does not contribute significantly to the core region. The power-law tail of a strong hot dust continuum contribution at K-band would swamp the CO absorption signature, leading to a weakening CO index. At larger distances the CO index shows a slight radial gradient, but this is not significant given the uncertainties in the background.

4.3.6 Characterizing the Extinction

The effects of dust absorption become noticeably less with increasing wavelength in our images of NGC2992. The K-band image has the most symmetrical appearance, with disk emission extending

through the dust lane. By referencing fiducial colours of expected stellar populations to the actual observed colours in NGC 2992, we can estimate the extinction due to dust. The H-K colour map is in general good for characterizing the extinction because it probes deeper within the dusty regions. However it has the problem that K-band may be contaminated by hot dust (1000 K) emission, resulting in possible overestimates of the extinction. Our CO-narrowband imaging confirms previous speculation from ground-based J-K and K-L colours (Alonso-Herrero et al. 1998) that hot dust is unlikely to contribute significantly.

We assume that the colour of a typical early-type bulge stellar population is $H - K = 0.2$ (Glass & Moorwood 1985), and that redder colours imply some degree of obscuration. Taking into account that the differential extinction between H and K is $A(H) = 0.175A(V)$ and $A(K) = 0.112A(V)$ (Rieke et al. 1985), we find

$$A(H-K) = -2.5\log(\frac{f(H)}{f(H_0)}) + 2.5\log(\frac{f(K)}{f(K_0)})$$

where $f(K_0)/f(H_0)$ is the flux ratio corresponding to $H - K = 0.2$. Thus $A(V) = A(H-K)/0.063$ in magnitudes.

Such an analysis is only true for extinction to the stars. Other emission processes (power law, nebular, etc.) will skew the results. The J-H and H-K colours show that there are two regions which can likely not be explained simply by reddened stellar colours. The first is within the dust lane, along the knotty spiral structure to the south and to the north along the diffuse loop described in section 3.4. The colours here tend to be bluer in both J-H and H-K, possibly indicative of nebular emission. The second is the extended region to the west of the nucleus where the colours are far from the locus of normal stellar colors, and different from both the disk/bulge to the east and the rest of the colours within the dust lane.

The extinction map (figure 4.7) shows that if the central peak of emission is in fact due mainly to a compact stellar core, then there is an optical extinction of A(V)$\sim$4 magnitudes. The J-H/H-K colours of the nucleus are consistent with a reddened supergiant population. Taken at face value, the extinction map contours indicate A(V) extinction from 2.6 to 8.6 magnitudes with 2 magnitude intervals, although non-stellar emission likely over-redden some of the circumnuclear regions as discussed above. Using the J-H map results in an extinction estimate which is lower, possibly as a result of the larger optical depth at shorter wavelengths.

4.4 Discussion

We have combined the various structures observed in the different wavelength regimes and depicted them schematically in figure 4.8.

The radio loops lack any optical or near-IR counterparts except along the galaxy disk axis. The bipolar outflows along the spin axis of the galaxy observed at larger scales in the optical (Allen et al. 1998) align along the same axis defined by the radio loops. These facts suggest the actual figure-8 loops likely lie out of the galactic disk plane. However, the strong radio contours, emanating from the nucleus to the southwest, lie along the buried spiral arm within the disk. Also, the red R-H loop to the north appears to be associated with the diffuse radio emission embedded within the larger radio loop.

Our hypothesis is then that the radio morphology consists of two components superimposed:
1) the loops out of the plane of the disk.
2) a component in the disk associated with the southern spiral arm, and a diffuse loop to the north. Starburst SNe remnants are the likely source of these radio components.
The appearance of the radio figure-8 becomes more symmetrical if the galactic disk components (point 2 above) are subtracted, which supports such a superposition scenario.

The assumption of trailing large-scale spiral arms, in addition to the prominent dust lane likely lying in front of the bulge, imply the NW edge of the galaxy disk is closer to us. This scenario places the southern portion of the Extended Emission Line Region (EELR) closer to us, with associated outflowing material (Allen et al. 1998). The southern radio loop would then also be closer to us, with the northern loop lying partially behind the dust lane. However, the larger-scale spiral arms extending radially out past 30″ appear to wind in the opposite orientation to the inner spiral observed in our high resolution imagery. This either forces the inner spiral arms to be leading, or else they are trailing in counter-rotation, with the inner region kinematically distinct from the outer galaxy. The case is not clear from the velocity fields presented in Allen et al. (1998), which have low spatial resolution coupled with a complicated superposition of rotation and outflow components.

The near-IR extended emission feature to the northwest gives the appearance of expanding into the northern radio loop, and the two emission features may be associated. The morphology and the rather extreme near-IR colours suggest that an AGN driven jet, possibly with some continuum component, could be directed into the radio loop. Hot dust present in an outflow is not ruled out for this feature either. This sort of near-IR "jet" may exist towards the southern radio loop as well at a lower level.

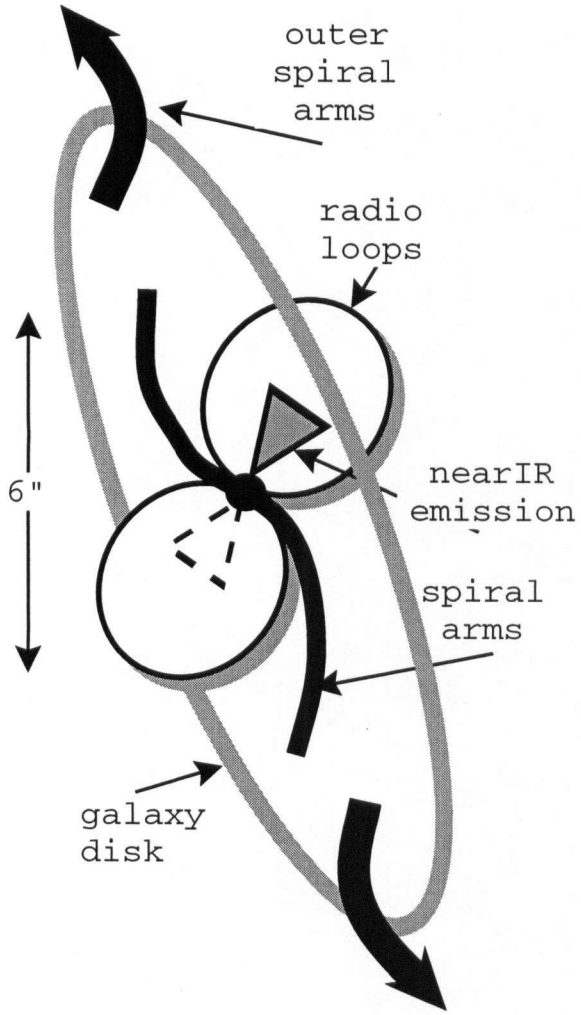

Figure 4.8: NGC2992 cartoon displaying the hypothesized geometry in the central 7″(∼ 1.3 kpc). The spiral arms lie within the galaxy disk (large grey ellipse), while the radio loops and possibly the nearIR extended emission are projected out of the plane of the disk. The speculative extended emission inside the southern radio loop is depicted as a dashed cone. The larger scale spiral arms extending out past 30″radially appear to wind in the opposite orientation to the inner spiral. The assumption of trailing large-scale spiral arms, in addition the prominent dust lane likely lying in front of the bulge, imply the NW edge of the disk is closer to us.

4.4.1 Interpretation

As noted in the introduction, there have been several models put forward for such figure-8 radio emission. The most convincing in light of our new near-IR imaging is that the figure-8 loops result from expanding gas bubbles which are seen preferentially as limb-brightened loops (Wehrle and Morris 1988). The northern loop may be related to the near-IR extended emission feature to the northwest. Further evidence for the outflow picture exists in the form of soft X-ray emission extended perpendicular to the disk of the galaxy Colbert et al. 1998), and Hα imagery clearly showing the location of an extended emission line region (EELR) (Colbert et al. 1996). These authors discuss two possible explanations for the extended X-ray emission: 1) an AGN driven hot plasma, 2) a superwind from a compact starburst.

A galactic-scale superwind can be generated by either a compact starburst in the galaxy core, or an AGN driven outflow which thermalizes the ISM at some distance from the core (Colbert et al. 1996). In both cases the superwind would blow preferentially out of the galaxy plane where the pressure is lowest, such as observed in NGC253 (Unger et al. 1987). With the resolved galaxy core in our images, it is not clear to what extent dust absorption, hot dust emission, scattered AGN light, or a compact stellar cluster contribute to the extended emission. The colours appear most consistent with reddened stellar light. Thus either picture could be consistent with our data since a stellar cluster and AGN (optical emission lines, flat radio spectrum) are likely contributing to core emission processes. However, the larger scale EELR need not be aligned with the 2″ diameter radio loops in the case of the AGN driven source. The orientation of the EELR observed at larger scales (Allen et al. 1998) is in fact roughly aligned with the radio loops. For superwind models, the anisotropic EELR, seen in [OIII] and Hα, is likely to be associated with the outflow regions. However, the superwind in itself does not yield a mechanism to produce continuum emission (Allen et al. 1998), thus our near-IR data may rule out this latter model.

If the near-IR "jet" is not actually related to the radio loops, the superwind model is still a plausible source of the loop emission. The CO index provides evidence for a substantial population gradient in the core. We consider the case where the radio loops are due to a energetic burst of supernovae in the past. The luminosity of the stellar cluster must be at least three times that of the bubble so the shock can reach a galactic scale height (Koo et al. 1992, Tenorio-Tagle et al. 1998) The stellar cluster luminosity is estimated from the H-band image. We determine the size of the "hypothetical" stellar cluster to be 0.5″ with an absolute H-magnitude of $-16.5 + M_{AGN}$, where the AGN contribution is unknown and may be almost zero if the supermassive black hole is no longer being fueled, as described in the introduction

(Bassini et al. 1998). The model PSF (section 3.1) scaled to the peak of the extended core revealed that an unresolved AGN component could contribute at most 37% to the emission within a 0.2″ diameter aperture.

The second model outlined in the introduction, with the toroidal magnetic fields causing the emission, is more difficult to explain in light of the near-IR extension and knotty emission along the southern radio loop. The outflow driven bubble model explains the currently available data much more naturally. In addition, a calculation of the magnetic energy in the loops from the 8.4GHz VLA data (Falcke et al. 1997, Werhle et al. 1988), makes it difficult to model consistently in this manner. Other problems with this model (Wehrle et al. 1988, Cameron 1985, Heyvaerts et al. 1987) associated with rotation timescales and the lack of twisting of the radio/near-IR loops, make it even less plausible.

4.5 Conclusions

We have presented adaptive optics near-IR and radio images of NGC2992 in conjunction with archive HST optical imagery. A spiral structure within the central 6″ and a 1″ extended feature are traced down to the core at the resolution of our images. We speculate that multiple radio components are superposed which contribute to the observed figure-8 morphology in the VLA images: one associated with the spiral structure in the galaxy disk, and another flowing out of the galaxy plane.

IR and optical spectra at high spatial resolution will likely provide the means of determining if the population gradients in the core of NGC 2992 are due to changes in age and/or metallicity. Such spectral imagery will also permit the nature of the extended structures to be explored, shedding light on the possible connection to the radio loops.

Our current hypothesis concerning the radio loops involves an AGN outflow powering the loop rather than a starburst superwind, as any near-IR emission related to the jet would be unlikely in the latter case. NGC 2992 represents yet another example of star formation and AGN components both existing in the galaxy core (Storchi-Bergman et al. 1997). There is no obvious indication of whether there is any connection between the two in evolutionary terms.

Chapter 5

NGC 3227

5.1 Introduction

It is generally accepted that pronounced activity in galaxies hosting Active Galactic Nuclei (AGN) results from accretion onto a supermassive black hole. However, the problems of overcoming the angular momentum barrier to fuel the nucleus (Shlosman et al. 1990) and also the unification of the AGN types (Antonucci 1993) have become especially vexing and controversial. Near-IR imaging has proven to be a powerful means to study these AGN problems as discussed in the introduction (chapter 1). Here, we focus on observations of NGC 3227, an SABa galaxy, interacting with its dwarf elliptical neighbor, NGC 3226. It has been much studied in recent years as it contains many of the elements thought to be related to the formation and evolution of active nuclei: emission line regions excited by both starburst and AGN continuum, strong interaction, and a stellar bar (Gonzales Delgado & Perez 1997, Arribas & Mediavilla 1994).

5.2 Observations

The images were obtained at the CFHT in March, 1997, using the MONICA near-IR camera (Nadeau et al. 1994) mounted at the f/20 focus of the Adaptive Optics Bonnette (AOB). The nucleus of the galaxy itself was used as the guiding source for the AO system, roughly a 15th magnitude point source. The natural seeing averaged $0.6''$-$0.8''$ throughout the observations resulting in relatively high strehl ratios in all bands, and FWHM of $0.14''$, $0.17''$, $0.22''$ at K, H, J bands respectively. At a distance of 15 Mpc for NGC 3227, $1''$=76pc using $H_0 = 50$ km s^{-1}Mpc^{-1}.

Image reduction and processing proceeded as described in chapter 3. The resulting images were then deconvolved using the classical Lucy-Richardson algorithm (25 iterations) with an input PSF reconstructed from the AO modal control commands obtained during the actual observations (Veran et al. 1998).

5.2.1 HST archive image

An HST WFPC2 image was retrieved from the archive for NGC3227 in the F606W filter, corresponding roughly to Johnson V and R bands, although with a greater contribution from R. The strong Hα line is contained in this filter, and contributes at several percent to some observed morphologies. The core of the galaxy lies on the PC chip with 0.4″ pixels. The image was rotated and rebinned to match the pixel sampling and resolution of our AOB images. The core of the galaxy is actually saturated and CCD bleeding is seen lying along the NE-SW axis.

5.3 Results

5.3.1 Core structures

The CFHT J, H, K and HST F606W (V+R)-band images are presented in figure 5.1, on a magnitude (log) scale. The high dynamic range of AOB (typically 1.3 x 10^4 at K) allows significant details to be seen at all flux levels. Subtraction of a smooth model galaxy (see below) reveals that this region is punctuated with bright knotty structures within a region 3″ x2″ (Figure 5.2). The knots appear to trace out several ring patterns, and are suggestive of a one-armed spiral. If the assembly is interpreted as a spiral, the winding sense is counterclockwise, in agreement with the large scale spiral arms. The colours of the knots are consistent with stellar and nuclear continuum contributions (section 5.3.2). We explored several methods of removing the low frequency galactic component, including various smoothing filters, a one-dimensional elliptical isophote model, and a multi-component (bulge, disk, point-source) elliptical isophote model. All methods consistently unveil the spiraling structure, with knots coincident in all of J, H, K and HST F606W bands. However, in the central 0.5 arcsec of the galaxy, subtracting isophotal fitting models results in prominent artifacts which obscure structural details.

We note that there has been some controversy over artifacts at the core of AGN galaxies imaged with AO, which imitate expected AGN structures (spiral arms, tori, etc.). Firstly, all structures treated as physical are either further from the nucleus, or else they are distinctly different and more extended than the artifacts cataloged in chapter 3. Secondly, we have compared the general morphology with HST-NICMOS images (Alonso-Herrero, private communication), which shows similar features, although at a lower spatial resolution at K-band and with 0.1″ pixels compared with our 0.034″ pixels.

Colour maps are formed by smoothing the images to the worse resolution of a given pair and taking the flux ratio (figure 5.3). The colour scheme used has redder colours darker (red) to emphasize dusty

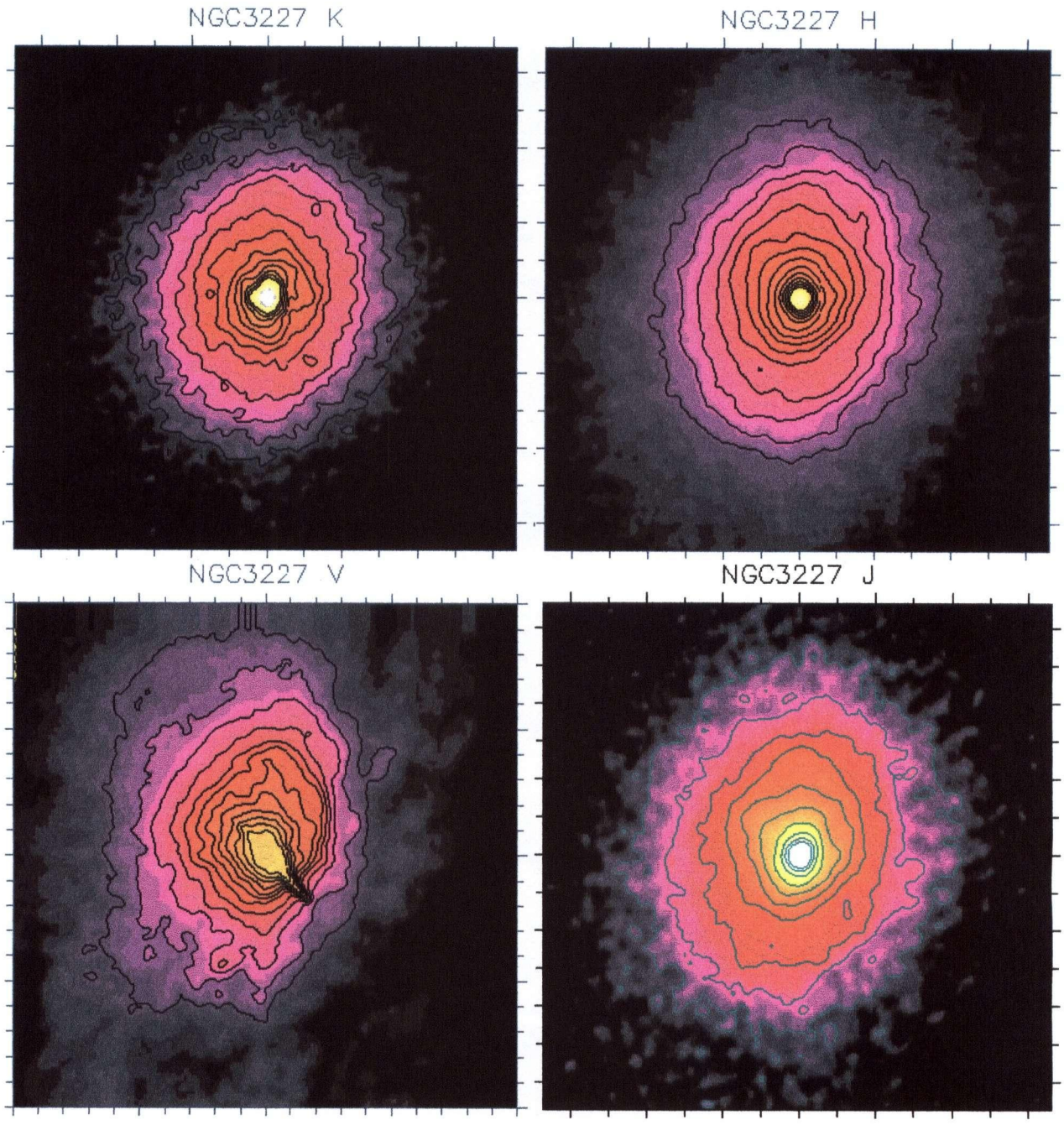

Figure 5.1: The central 6.7″ of NGC 3227 in K, H, J, F606W (R+V). In all images, North is up, East is left

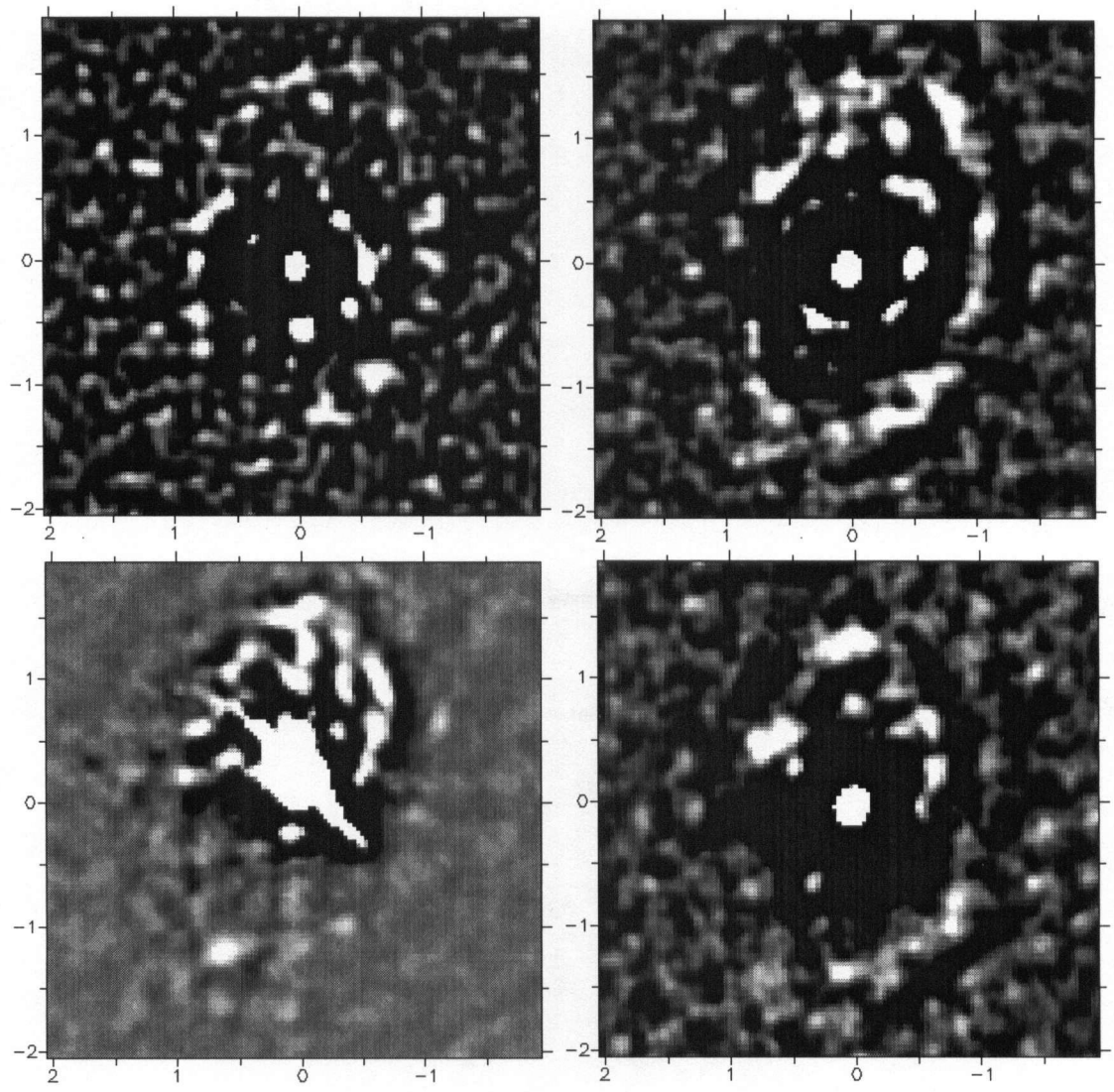

Figure 5.2: Close-up of central 4″ region with smooth model subtracted images of NGC 3227. Clockwise from upper left is K, H, J, F606W (R,V)

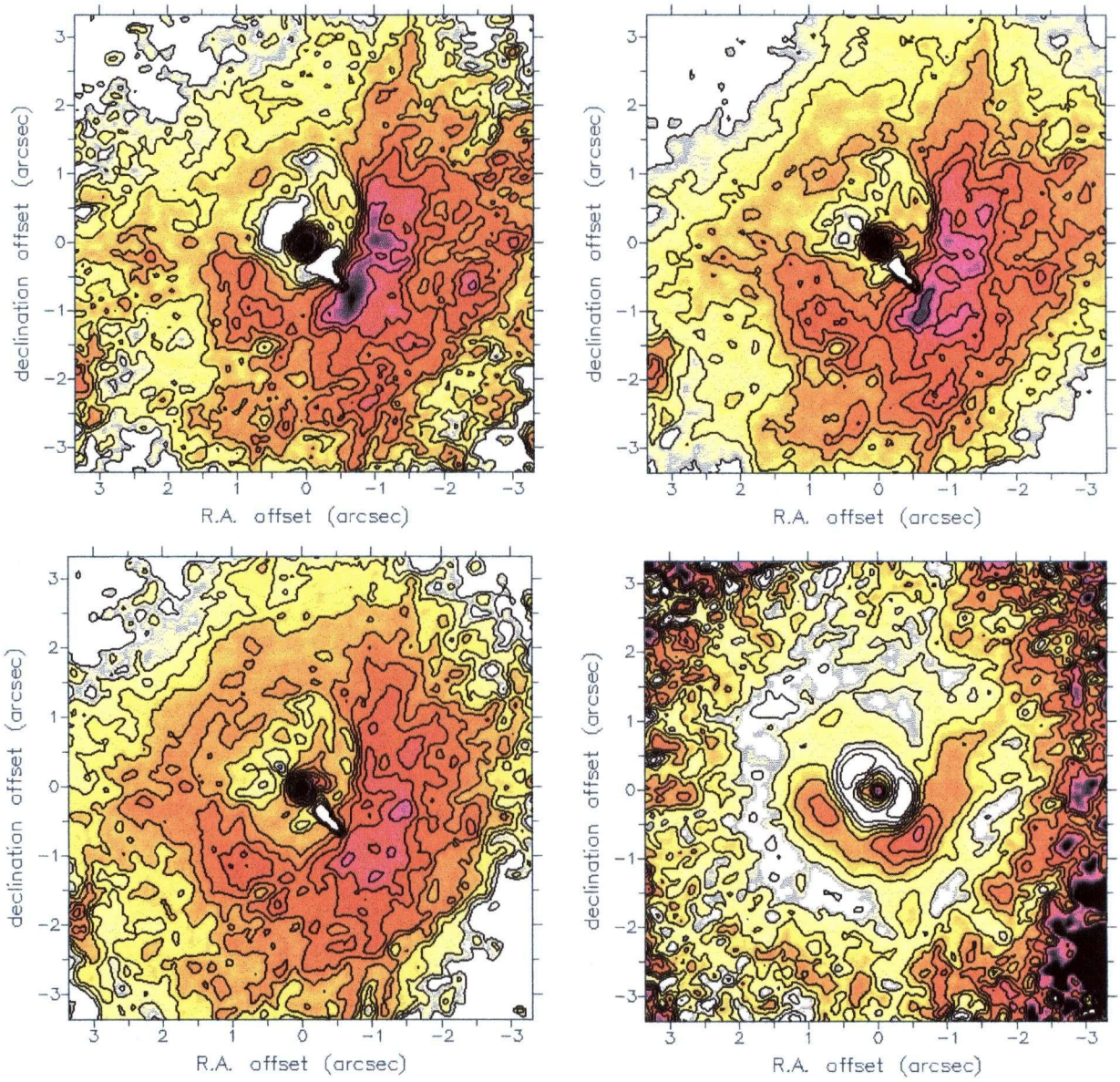

Figure 5.3: Colour maps of NGC 3227, clockwise from upper left is R-K, R-H, J-K, R-J. The colour scheme used has redder colours darker (red), and bluer colours lighter.

structures. Any colour gradients in these images can result from several different processes: 1) change in dust 2) change in stellar population 3) change in gas. The most prominent feature is an irregular-shaped patch to the southwest. The fact that this region appears clearly as a deficit in the V-band image, and takes on a patchy morphology is strong evidence for dust obscuration as the source of the colour gradient. The region is therefore most pronounced in the V-K colour map, since the K image is least affected by dust. The J-K and H-K images indicate that substantial dust still affects this region in the J, and even H-bands. We estimate A(V)$\sim$8 magnitudes in this region, assuming an intrinsic stellar index of H-K=0.22, J-H=0.78 (Glass & Moorwood 1985), and an extinction law A(K)=0.112 A(V), A(H)=0.175 A(V) and A(J)=0.282 A(V) (Rieke & Lebofsky 1985). The colour maps reveal that the nucleus itself is very red, consistent with a reddened nuclear continuum component, with possible thermal dust emission in the K-band. The red colours surrounding the region of bright pointlike objects described above stands out from a region slightly bluer than the larger scale bulge of the galaxy. To the northeast, the colours are generally bluer, but this may simply be in contrast to the very red colours of the SW dust absorption.

Although the HST R-band image has strong CCD bleeding from the bright nucleus, a northeastern nuclear extension of about 1″ to the isophotes is apparent in all the images (figure 5.1), where it appears to extend furthest, and with the largest PA, in the J-band image. This feature appears as an ellipse of $\sim$ 1″ extent is visible in all the colour maps, roughly orthogonal to the plane of the galaxy, with bluer colours than the surrounding regions. The images are distorted by PSF artifacts in the central 0.5″, plus the above mentioned CCD bleeding in the HST image. However, the extent and position angle (PA) of 43° indicate that this feature is unrelated to the AOB artifacts described in chapter 3. Although the HST CCD bleeding lies along a similar PA, the feature appears in all the near-IR colour maps by themselves. Figures 5.7 and 5.8 depict all of these structures relative to each other and the larger scale galaxy).

5.3.2 Colour-colour diagram and "chromatogram"

The colour-colour diagram of the point-like structures (hereafter called knots) revealed in figure 5.2 is displayed in Figure 5.4 (upper panel), highlighting the most clearly identified knots between model-subtracted J, H, and K bands images (figure 2). The colours are measured through aperture photometry, where apertures of 0.2″, 0.3″ and 0.4″ were used to derive an estimate for the uncertainty of 0.2 magnitudes for J-H and 0.1 magnitudes for H-K. The larger uncertainty in the [J-H] index is likely a result of the poorer resolution in J-band relative to H and K, and some of the knot regions blend with

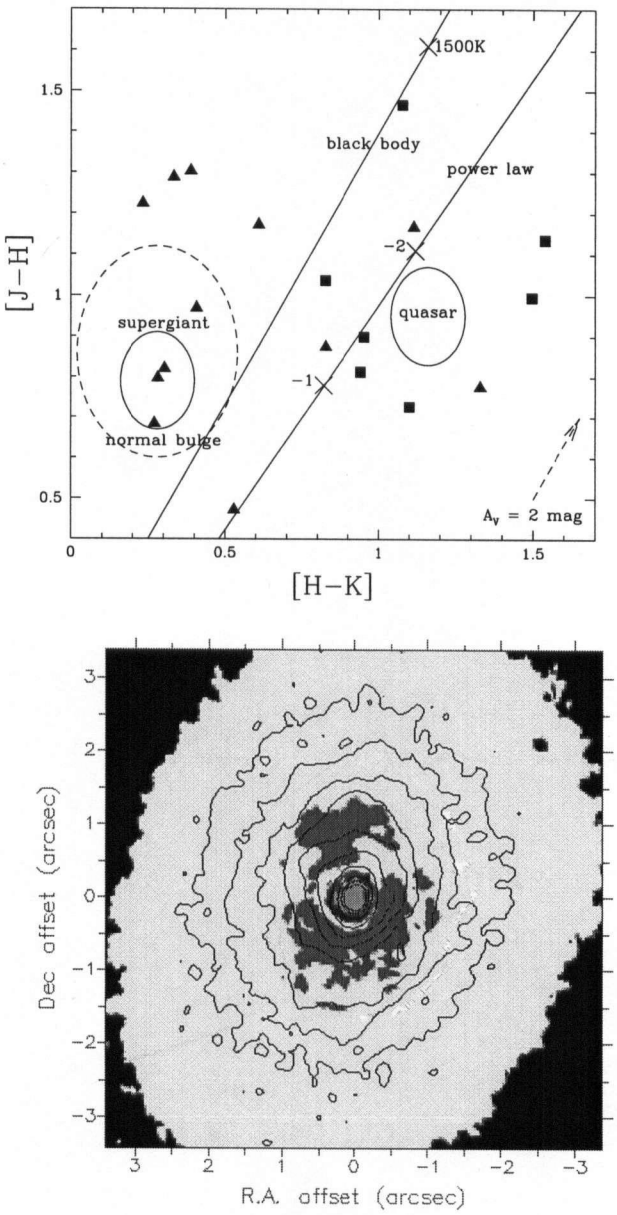

Figure 5.4: Upper Panel: Colour-colour diagram of the knot-like structures of in the core region. A vector showing the effects of 2 magnitudes of visual extinction is shown, along with the locus of colours for normal spiral bulges and continuum power law from quasar-type nuclei. The knots further from the nucleus tend to have colours near the locus of normal spiral bulge stars (triangle symbols), while those closer in are more centered on the continuum power law region (square symbols). Lower Panel: Chromatogram - a mapping of the colour-colour plane onto the image proper. Contours show NGC3227 J-band deconvolved image. Yellow represents normal stellar disk colours, while purple represents a supergiant population. The red colour of the nucleus is likely as a result of power law continuum plus dust reddening.

surrounding ones. The colours of the regions and visible knots were verified in the actual colour maps, where the estimated photometric accuracy is < 0.1 magnitudes. Within the uncertainty there is still a rather large spread in the colours for these knot structures. The knots further from the nucleus tend to have colours near the locus of normal spiral bulge stars (triangle symbols), while those closer in are more centered on the continuum power law region (square symbols). This can be explained if scattered nuclear light and thermal dust emission are superposed with a starbursting component for the nuclear knots.

To get a sense of the variation of near-IR colours with galaxy morphology, we can provide a mapping of the colour-colour plane onto the image proper, indexing each emission region with a different colour - a "chromatogram". We have expanded on a colour mapping used by Lai (1996), by varying the dust extinction and defining the emission regions to account for photometry error in our observations. The resulting chromatogram for NGC 3227 is presented in figure 5.4 (lower panel) with contours of the J-band deconvolved image overlaid as an additional guide to the galaxy morphology. The colour-colour diagram in figure 5.4 (upper panel) shows the main regions mapped onto the chromatogram: the loci of normal stars, quasars, and nebular emission, as well as power law and dust emission.

This chromatogram (figure 5.4-lower panel) shows that the bulk of the colours in the core region are consistent with stellar or reddened stellar colours (yellow). Several bands within the mini-spiral pattern have colours consistent with a younger supergiant population (purple). The red colour of the nucleus, with a small black ring surrounding it, are likely as a result of power law continuum plus dust reddening.

5.3.3 Isophotal analysis and small-scale bars

The transfer of mass from large to small scales is a vexing problem in AGN research. From a theoretical standpoint, galactic bars are perhaps the most viable candidate for facilitating this mass transfer (Schwartz 1981; Norman 1987; Shlosman, Frank & Begelman 1989). The relatively constant surface brightness along the bar results in a clear signature in the radial profile analysis of a galaxy. We follow the criterion for a nuclear bar discussed in Friedli et al. (1996). This involves a rise then fall in ellipticity (E) while the position angle (PA) stays constant over the rising E. Double bars would appear as two bumps in E, and a bar plus twist has the PA and E (or just PA) changing simultaneously after the bump. In the larger scale galaxy, the ellipticity would then decrease to reveal the inclination of the disk, but our field does not extend this far. If there is more than a 10 degree shift in position angle over a bump in E, then the feature is classified as a twisted isophote rather than a bar.

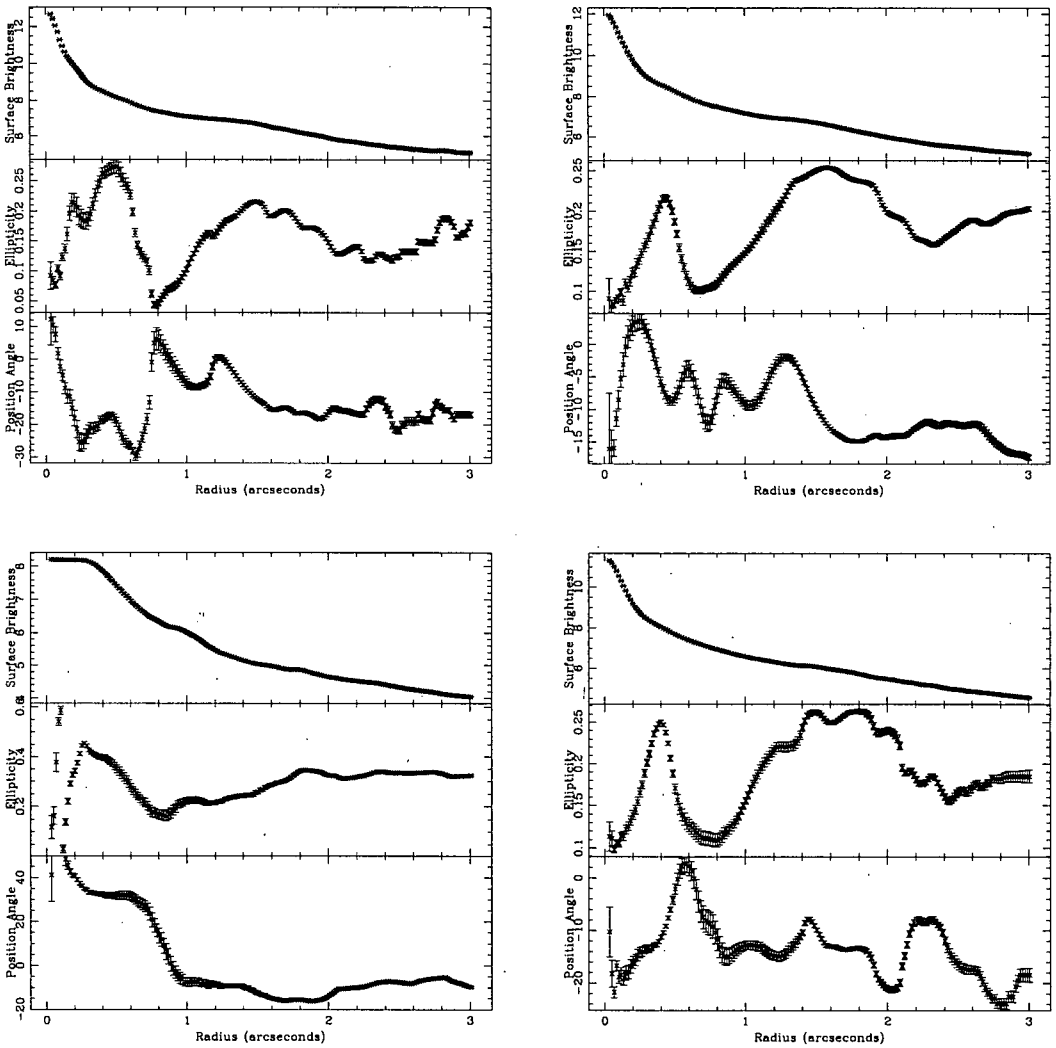

Figure 5.5: Profiles of NGC 3227 from 1D elliptical isophote fits. Clockwise from upper left: K, H, J, F606W (V). Note that the saturated HST V-band surface brightness is flat in the core. Error bars represent 1σ isophote fitting error.

The variations of surface brightness (SB), ellipticity (E), and position angle (PA) for the galaxies were extracted from the fitting of elliptical isophotes. The profiles are similar at J, H and K (figure 5.5), displaying bumps in ellipticity at 0.5 and 1.5 arcsec radius, confirming the presence and position angle of the nuclear ellipse (PA $\sim 40°$) and the larger enhanced region coincident with the spiral starburst (PA $\sim -10°$). The H and K bands are less obscured by dust and the profile is most clearly defined in at these wavelengths.

For the spiral starburst region, the isophotes are twisted of order 10 degrees. The images (Figure 5.1) show that the region extends to the south of the nucleus at H and K bands and would be consistent with a bar potential by our above criterion. At V-band, the region only appears to extend to the north due to the southern dust obscuration.

For the nuclear ellipse, the PA twists more significantly ($\sim 20°$), and its twist and orientation vary with wavelength. At the smallest scales, this is likely the result of the wavelength dependent AO/PSF artifacts dominating the signal. For the outer extent of the disk, the multiple emission components possibly contributing to the flux (see above) likely vary with wavelength, with a strong stellar component at a larger PA in the J-band. The twisted isophotes do not satisfy our bar criterion, but the profiles are difficult to analyze with certainty as the feature is near the limit of our image resolution and clouded by artifacts in the very core regions.

5.3.4 Comparison with MERLIN radio data

The images are compared to the 6cm and 18cm MERLIN radio continuum emission (Courtesy of C. Mundell. Originally published in Mundell et al. 1996), which align with the axis of the nuclear spiral (figure 5.6). Previous explanations for the radio structure (Mundell et al 1996), invoked the standard unified AGN model to explain this emission. Even at the low resolution of their optical images, it was apparent that there was an offset in orientation from the [OIII] "cone" and the small-scale radio features. A projection effect would be possible, but this would necessitate that the NE side of the disc is closer to us than the SW side. This would only be possible if the spiral arms were leading rather than trailing (Mundell et al. 1995, Pedlar et al. 1987). Our high resolution imaging suggests that the radio emission may be unrelated to any kind of jet outflow, and instead is associated with the nuclear knots observed in figure 5.2. The peak to the north is only observed at 18cm with no 6cm counterpart, likely indicating a steep spectrum consistent with supernova remnants in the regions of star formation. The southern peak spectral index is consistent with a compact active nucleus (Mundell 1995, Ho 1999), and

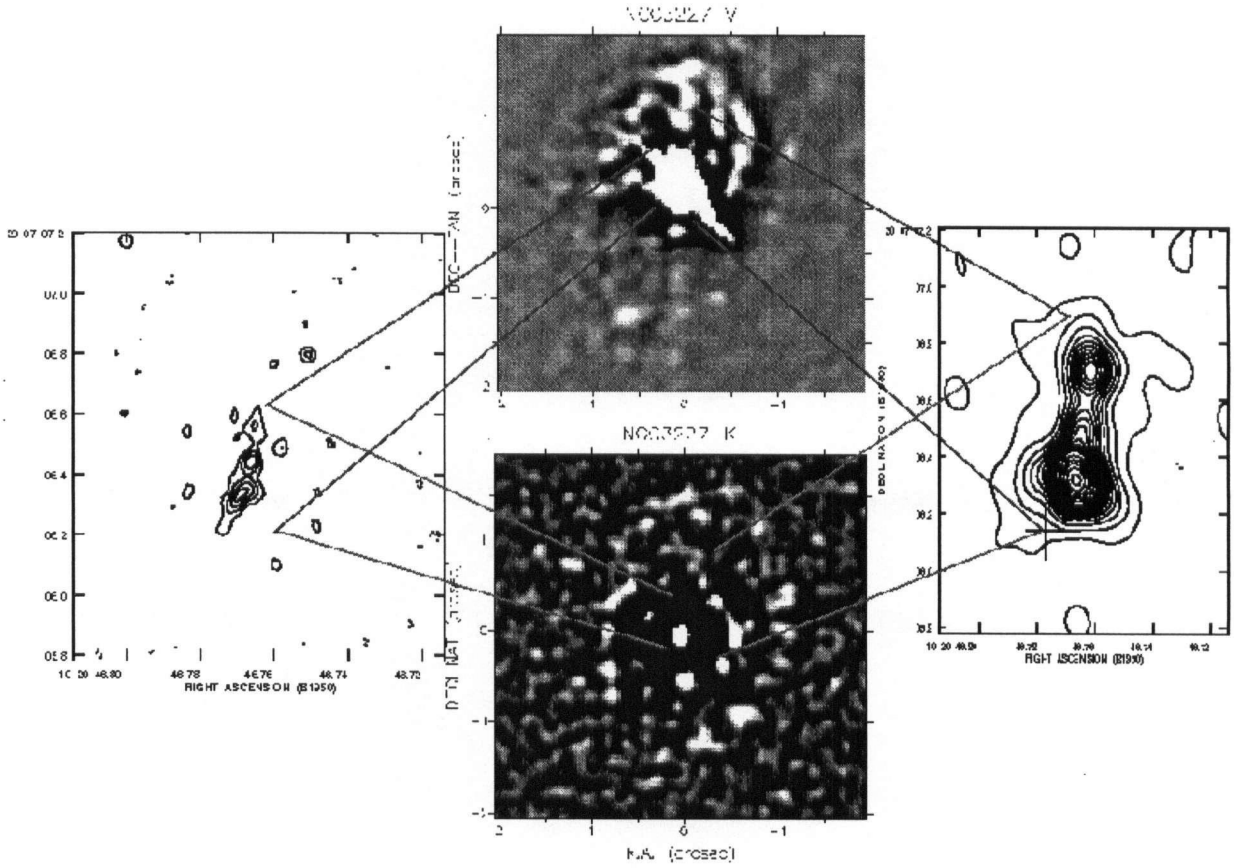

Figure 5.6: The 6cm (left contours) and 18cm (right contours) of NGC 3227 showing the location in the model subtracted V (above) and K (below) bands.

Table 1
The structural components of NGC3227

Component	Scale	PA (°)	E (1-$\frac{b}{a}$)	Observed with	Function in galaxy
Large Scale galaxy	1-10 kpc	-25	0.3	V-band	
Large Scale bar	1-5 kpc	-30	0.5	galaxy subtracted	funnel material to I LR at 7″
Extended [OIII]	1kpc	35		OIII filter/ OASIS [SIII]	collimated emission ?
Circum-nuclear ring	1 kpc			H_α	ILR
Medium Scale bar	100-1000pc	?		submm CO	funnel material to ILR at 2″
K-band ellipse	200 pc	-10	0.2	model subtract, colour maps	spiral starburst, ILR
Radio jets/blob	100 pc	-10		MERLIN 8/16cm	SN/outflow?
K-V blob	100 pc	-10	0.1	K-V map, raw Vband	bluer than galaxy
K-J annulus	100 pc	40	0.3	all colour maps & images	twisted disk/bars, scattered AGN light

we therefore align our near-IR nuclei to this point. As figure 5.6 shows, the radio aligns well with both the orientation and some of the knots of the starburst spiral, and a possible interpretation is that we are seeing synchrotron emission from SNe remnants.

5.4 Discussion

Several possible scenarios emerge from these results. We tabulate the observed structures in this galaxy from the largest to the smallest in Table 1. Refer to cartoons in figure 5.7 and 5.8 for a depiction of scales and relationships of the features. On the largest scales Gonzalez-Delgado et al. (1997) noted that a large-scale bar appears to transport material towards an inner radius which corresponds to the calculated Inner Linblad Resonance (ILR) at roughly 7″. At this point, prominent dust and HII regions indicate substantial star formation. Within this region, a molecular bar (see below) of length $\sim$ 1kpc is observed in CO with an ILR of $\sim$2″ (Schinnerer 1998) This radius corresponds with the outer extent of the knots (figure 5.2) suggestive of a ring or spiral structure in our images.

With such nested bar structure repeating itself at these two larger scales, it is natural to speculate that the small scale elongation seen in the colour maps and profile analysis may be yet another bar potential funneling material down to the scales where viscous forces may take over to fuel the AGN. However, a larger scale extended [OIII] region (Arribas et al. 1994, Mundell et al. 1995, Gonzalez-Delgado et al. 1997) lies to the northeast and has been interpreted as a narrow-line region ionized by the AGN, collimated into a cone by a small-scale ($\sim pc$) dusty torus. The fact that this collimation axis roughly aligns with our "bar" may be an indication that this elongation actually represents scattered AGN light. This is made all the more convincing by the blue colour of the elongation.

On the other hand, if our observed small-scale elongation is some sort of twisted disk as found in

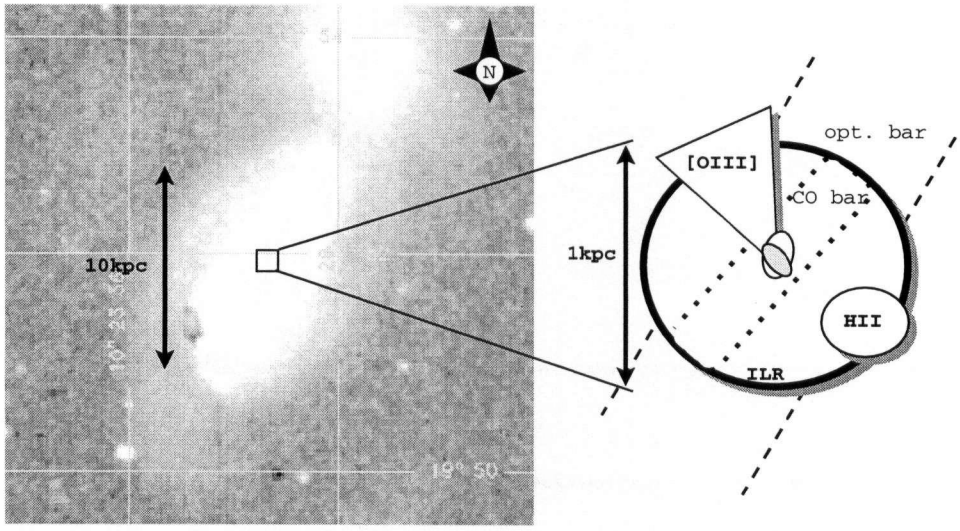

Figure 5.7: Palomar Digital Sky Survey (DSS) image of NGC 3227 interacting with the dwarf elliptical companion NGC 3226 to the North. Inset cartoon of the larger scale features: the large scale stellar bar funnels material to the ILR (depicted by the large circular region). A proposed smaller-scale molecular bar resides within (PA is approximate), presumably transporting material down to the scales probed with our AO images (overlapping ellipses in the very core). The [OIII] ionization cone and detached HII region are shown to scale.

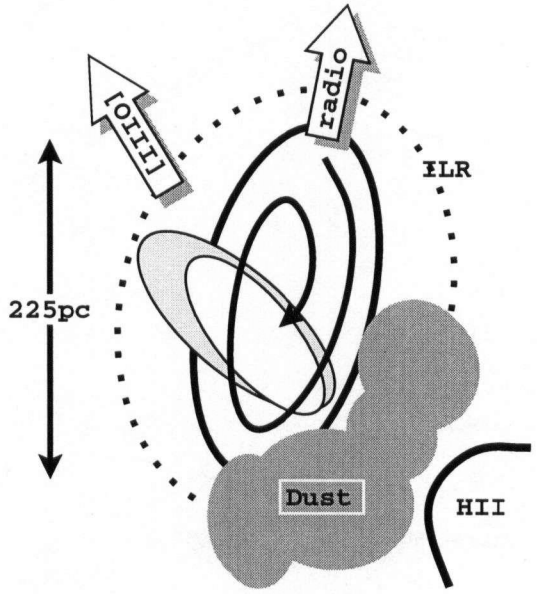

Figure 5.8: Cartoon of the smaller scale features probed by the CFHT AOB: the ILR of the proposed molecular bar (Schinnerer 1998) is depicted as the dashed ellipse surrounding the spiral starburst region. The radio "jet" ($PA = -10$) aligns with this spiral region. The dusty region to the SW may be a reason for the lack of [OIII] and the detached HII region. The two possible components of the inner nuclear disk are shown as overlapping ellipses. The direction of the extended [OIII] region is shown by an arrow. The solid black (one-arm) spiral is drawn to suggest the possible structure associated with the nuclear knots seen in figure 5.2.

Centaurus A by Schreier et al. (1998), its plane lies roughly perpendicular to the axis defined by the radio "jet" observed at 6 and 18 cm, and would be consistent with a collimated radio jet normal to an accretion disk plane. For the radio emission to be interpreted as an outflow, the picture describing the NLR [OIII] interpreted as collimated ionization would then likely have to be abandoned. We explore these scenarios below in light of new Integral Field Spectroscopy (IFU) with OASIS.

5.4.1 Fueling the nucleus

Schinnerer et al. (1998), using millimeter interferometry (IRAM), have identified a molecular gas bar within the central kpc (14″), with an associated ILR at $\sim 2''$. This radius corresponds approximately to the outer radius of red nuclear region with the knot structures embedded (figure 5.2). They also find an essentially unresolved molecular disk ($\sim 2''$) at the galaxy nucleus which would be coincident with the nuclear ellipse identified in our images. At least the outer rings of knots identified in the model subtracted images (figure 5.2) have colours which could be interpreted as star formation as the result of gas collected by the kpc molecular bar at the ILR. Schinnerer found that the gas motions at this radius can be successfully described by circular motion in a tilted ring system.

Both of the features identified as ellipticity peaks in the profile analysis, may also be associated with nested bar-potentials. The high density of starforming knots would be formed by the shocked gas along the leading edges of the bars. The nuclear knot structures, interpreted as a loose ring/spiral assembly within 200pc, could then be the result of starformation caused by several bar rotations. A succession of bars at smaller and smaller scales, twisting inwards, would thereby transfer material from the outer galaxy all the way to the core region (few pc) to fuel the active nucleus. This is similar to the model put forth by Sholsmann et al. (1989).

In the absence of any true bar potential in the nuclear region, the fate of knots of star formation generated near the 2″ ILR will then be to drift inwards with time (Morris et al. 1996), being carried apart by differential rotation. This process could mimic the spiral/ring assembly seen in the core region. In our own galaxy at roughly comparable scales, similar processes are thought to be at work (Morris et al. 1996). Although the Milky Way is thought to have a supermassive black hole in the core (Ghez et al. 1998), it appears not to be active currently, possibly due to lack of fuel, and the explanation for why some galaxy cores are fueled and some not would have to lie at even smaller scales.

Regan and Mulchaey (1998) claim to have found spiral dust lanes that appear to provide fuel for black holes at the centers of active galaxies, suggesting that that material does indeed spiral in towards

the center, rather than being forced down in the presence of a strong bar potential. Our images would be consistent with this picture as the core elongated starburst region is seen as interspersed wispy spirals in the colour maps and model subtracted images (Figures 5.2 and 5.3). However, there currently is no theoretical or numerical model supporting such a scenario, and it is not yet clear that such a mechanism could fuel the active nuclei.

5.4.2 The role of the radio feature: jet or starburst?

AGN origin to the radio feature

The radio extension may be a jet powered by the Seyfert nucleus. We could then interpret the twisting nuclear ellipse in the central 2″ as a disk/torus related to the collimation axis defined by the radio feature. Several arguments support this picture: 1) there is a molecular disk counterpart (although unresolved) at a similar scale (Schinnerer et al. 1998); 2) the near-IR disk/torus is roughly perpendicular to the jet; 3) the twisting of the disk/torus is in the orientation such that the structure would be more perpendicular with the jet at the smallest scales. The feature might even be associated with an extended torus as seen for instance in NGC4261 (Jaffe et al. 1996), and as described in the models of Maiolino et al. (1997). Since the radio jet aligns well with the ellipse of the starburst knots, and the radio peaks correspond to starburst knot features, we could interpret this blue starburst region as a narrow line emission region (NLR) excited by the AGN continuum. Kotilainen et al. (1997) also found a blue excess in their optical colour maps lying in 2 lobes surrounding the nucleus on the NW- SE axis which they interpreted as scattered nuclear light. Higher spatial resolution spectral imaging is required to confirm whether the line ratios and dynamics within this region are consistent with the continuum ionization of a NLR.

The suggestive spiral/ring morphology of the starforming knots makes it less likely that this region is a random assembly of starburst knots resulting from shocked gas in the NLR/radio jet entrainment. In addition, the nuclear disk may have two emission components at different PA associated as suggested in section 3. Although, within the disk, the more extended ellipse at larger PA certainly appears stellar in origin, the inner disk at smaller PA may be substantially scattered AGN light, implying that the radio jet does not necessarily define a unique collimation axis.

However a small scale ($\sim$ pc) dust torus which collimates the larger scale emission is not a mandatory feature of AGN. Indeed Malkan et al. (1998) have put forth a viable alternative scenario where patchy dust up to 100 pc from the nucleus would lead to the classification differences seen in many AGN.

Our near-IR extinction maps for a large sample of Seyfert galaxies show that this is a plausible picture (Chapman & Morris, 1999b). If this is the case for NGC 3227, then there is not necessarily a contradiction in a having a radio jet along the presumed spin axis of the AGN in addition to the continuum excited emission towards the NE where the larger-scale dust obscuration is much less than to the SW.

Starburst origin to the radio feature

Regardless of whether the extended [OIII] narrow-line region to the northeast defines a collimation axis of a small-scale obscuring torus, there does seem to be evidence for preferential continuum ionized emission towards the NE regions. The scattered light interpretation of at least part of the disk feature is consistent, and our colour maps show a bluer colour to the NE at larger scale which may well be further support of this picture. This scenario lends weight to our NE blue colour not just being a contrast effect with the dusty SW as described in section 5.3.1.

A case can therefore be put forth that there is a "classical" bi-conical emission structure in this galaxy, largely obscured to the SW, and collimated at small scales by some kind of dusty torus. The elliptical region surrounding the starburst knots might then represent a disk, orthogonal to the ionization axis, with well defined spiral arms and small-scale bar, facilitating mass transfer to the core region. With this geometry, in addition to the radio morphology extending along the axis of the ellipse of knot structures (figure 5.6) (possibly with knots coincident with the actual radio peaks), the most plausible explanation for the radio emission seems to be supernova remnants associated with the starforming clumps. If we accept this picture, it is difficult to interpret the radio feature as an AGN-driven jet mis-aligned with the ionization cone, since projection effects are not consistent with the known motions of the galaxy (Mundell et al. 1995). It does not necessarily preclude an outflow driven by starburst superwinds (Heckman et al. 1990, Unger et al. 1987), since the superwind outflows are preferentially blown out of the plane of the galaxy, consistent with the galactic motions with the SW side of the disk being closer to us than the NE side. An AGN collimation axis would not be expected to lie in any preferred direction (Malkan et al. 1998) and there is no problem interpreting the ionized regions within this geometric picture.

5.5 Conclusions

We have observed NGC 3227 at J, H, and K bands using adaptive optics on the CFHT. Despite recent controversy over artifacts surrounding the cores of bright point sources with adaptive optics, we are

confident that we have identified several structures in the central few arcseconds. An assembly of star formation knots lying in a spiral/ring pattern, is suggestive of embedded spiral arms within the larger-scale spiral of the outer galaxy. An elongation of $PA \sim 40°$ may be a nuclear disk or bar structure, although the blue colours are suggestive of some scattered nuclear continuum emission. The extended radio feature observed with MERLIN is coincident with near-IR knot structures in the spiral/ring region, and may be associated with some kind of outflow. There are still several conflicting pictures which appear consistent with the data. The situation will be further elucidated by higher spatial resolution imaging spectroscopy and perhaps NGST imaging of the even smaller-scale morphology.

Chapter 6

Challenging the unified AGN model

We have seen in Chapter 4 that the near-IR colour maps unveil structural details in the galaxy not apparent in the individual filter images. The near-IR colour maps were also useful for quantifying the extinction due to dust given the large optical depth of the longer wavelength near-IR filters. In this chapter, we build on these ideas in order to quantify and critique the classification picture proposed by Malkan et al. (1998) where clumpy dust at radial distances $> 100\,pc$ from the galaxy nucleus is invoked to explain differences in observed Seyfert types. We first characterize our sample of Seyfert galaxies in relation to other observed samples, in order to assess the applicability of our results.

6.1 Problems with standard Unification

The idea of unifying the various types of Seyfert galaxies has become well established (Antonucci 1993). The general picture is that each Sy2 nucleus actually harbours a normal Sy1 nucleus in its center (see for example, Peterson 1997). The hypothesis is that the point-like non stellar continuum and the broad line region (BLR) are obscured along the line-of-sight (LOS). to the central engine. The standard unification picture invokes a dusty molecular torus surrounding the nucleus at a scale of a few *pc*. Viewing angle is the sole factor which governs the amount of obscuration experienced along the line-of-sight to the observer. We will refer to this picture as the Accreting Torus Model (ATM). For some of the better studied AGN, there is certainly evidence in favour of the flavour of this unification paradigm. It is thus prudent to take this as a starting point and use our data to make further inferences.

There have always been problems with the ATM; there are significant data which refuse to be forced into such a simple picture. In addition to the usual difficulties with the simple unified scheme outlined in chapter 1 (see also Antonucci 1993), examples include the intrinsic differences between Seyfert types found in longer wavelength broad-band studies (Edelson et al. 1989, Ward et al. 1987, and Carleton et al. 1987). Edelson et al. (1989), for instance, noted more heavily reddened emission line ratios and different thermal dust emission spectra in the infrared for Sy2s. Several recent studies have also

pointed to possible intrinsic morphological differences between the host galaxies of Seyfert 1 and 2 nuclei. Maiolino et al. (1997) found that Sy2s are characterized by a fraction of non-axisymmetric potentials (including interactions and peculiar morphologies) about 20% higher than Sy1s

. Mulchaey et al. (1997) and Ho et al. (1997a) found the occurrence of bars in Sy2 to be 10–20% higher than Sy1s. Malkan et al. (1998) did not find any difference in the bar properties at small (10s of pc) scales, but did find that Sy2s were significantly dustier within the central 10″.

There are, however, several points which must be taken into account in considering alternatives to the ATM model. The first is obscuration, since X-ray data have now shown that considerable column densities of hydrogen (N_H) are found in the nuclei of many type 2 active galaxies. The second is collimation. This is a more difficult issue, since there do seem to be cases clearly where anisotropic ionization regions are observed in the extended narrow line regions (NLR) and could be explained as being defined by the opening angle of a dusty torus. The most clear-cut cases are Seyfert 2 types or intermediate types as expected from the supposed edge-on geometries (Mulchaey et al. 1995); a face-on cone appears as a circle. Such ionization cones found in true Seyfert 1 galaxies are less common and perhaps do not exist at all (Wilson et al. 1996). The third point to account for is polarization, since BLRs have been observed in many cases now in the polarized spectrum, implying a hidden Sy1 nucleus (Tran et al. 1992).

However, much of this evidence in favour of the ATM is not necessarily as sound as proponents would like to believe. In many cases the "cone" morphology of the NLR is at best an interpretive stretch of the data, and is sometimes quite implausible (NGC 3227 included - see chapter 6). Radio jets have been observed in Seyferts (Ulvestad & Wilson 1984, Nagar et al. 1999), and are thought to emanate from the black hole spin axis, as with the more powerful Radio-Loud Quasars (Antonucci 1993). Even if the continuum emission from the active nucleus is not collimated by some dusty parsec-scale torus, there are shocks associated with the jets and one can produce apparent asymmetrical or bi-symmetrical emission line structures through the entrainment. A "cone" of emission has strong implications however: it is the shadow cast by the hard edge of some object. There do remain, a few cases with HST narrow line imaging which have come close to appearing like the razor-sharp cones implied by an edge on dusty torus (Wilson and Tsvetanov 1994, Wilson 1996, Hutchings et al. 1998).

The polarization studies have also revealed that the amount of polarization is always less than predicted (Tran et al. 1995), and the number of cases where a hidden BLR is found is nowhere near 50%+ as expected from the distribution of Seyfert types. On the positive side, there are a number of

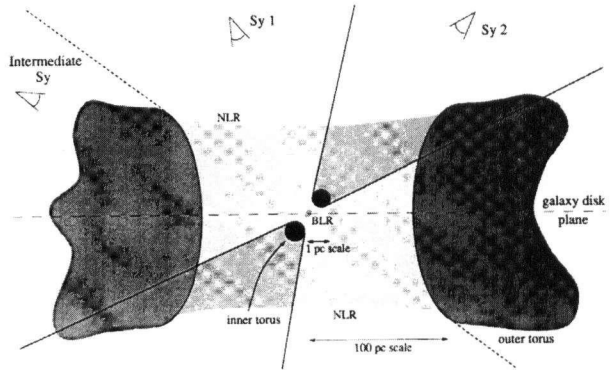

Figure 6.1: Outer dust torus model proposed by Maiolino et al. (1995). Intermediate Seyferts then provide a partially blocked view of the central engine, without the extreme extinction of the pc-scale molecular torus.

factors which would suppress the polarized view of the BLR (Robson 1997), not least of which would be the lack of a suitable reflecting medium.

The obscuration is clearly something that must be carefully explained, however it is certainly not obvious that the ATM can or must be the explanation in all cases. Maiolino et al. (1995) proposed an extended (100 pc) dust torus model to explain intermediate Seyfert types, where the outer dust torus lies in the plane of the galactic disk, at a different orientation than the central accreting torus directly surrounding the central engine at a distance of about a parsec (figure 6.1). This model retains the flavour of the ATM, leaving viewing angle to be the only deciding factor for a Seyfert's classification. Although such extended dusty tori are not typically observed in nearby Seyfert galaxies, several recent results (Jaffe et al. 1993, Simpson et al. 1996), as well as a few of our colour maps, do show evidence for such a structure. The extended torus is not particularly attractive from a numerical/theoretical perspective (Friedli and Benz 1993, Piner et al. 1995). The outer dust torus may provide a satisfactory answer in some cases, but cannot explain all the cases observed.

A new model to explain the different classes of Seyferts has been proposed by Malkan et al. (1998) based on high spatial resolution imaging with the HST. They propose a general picture where patchy dust at >100 pc from the nucleus is more abundant in Seyfert 2 galaxies and will tend to drift in front of the nucleus in certain cases.

6.2 Characterization of the Sample

Table 6.1 provides a listing of the criteria used for the various Seyfert classifications. Table 6.4 provides a list of brief galaxy descriptions based on the central 10″ of the galaxy for both the near-IR and optical images. The comments based on the optical HST F606W images were adapted from Malkan et al. (1998) for the 29/37 of our galaxies in their sample. The third column of Table 6.4 again presents the estimated resolution attained in each AOB image, since structures may be missed for the poorer resolution images in our sample. The fourth column provides an indication of whether the core artifacts described in chapter 3 might influence the near-IR descriptions.

The central 6.″8 × 6.″8 of each galaxy (corresponding to the central 200×200 pixels of each image) are displayed in H-band, which is generally the deepest image obtained, in figures 6.7 through 6.13, arranged by Seyfert type. The close-up of the nuclear region emphasizes features which are not detectable with uncorrected ground-based seeing limitations. The colour scales are in magnitudes (logarithmic), where the brightest pixel values in the galaxy center are set to white (lightest colours).

In general, the deeper views through dusty regions afforded by the near-IR images result in morphological descriptions based on optical and near-IR images to vary considerably in some cases, even after taking into account the AOB artifacts and differences in spatial resolution.

6.2.1 Sub-classification of Seyfert 1's

With the improvement in resolution afforded by AOB imaging, we are able to discern resolved from unresolved cores in our Seyfert sample down to the typical resolution achieved in our sample (mean corrected FWHM of 0.″23). At the median redshift of our sample ($z = 0.009$) the implied maximum AGN scale is 60 pc ($H_0 = 50\, km\, s^{-1} Mpc^{-1}$). Without exception, the Sy2 galaxies are resolved at this scale, while most of the Sy1 appear unresolved, in agreement with the optical HST results of Malkan et al. (1998). The time variability of the featureless continuum emitted by Sy1 nuclei indicates a scale-size of less than 1 pc. Thus we expect to view Sy1 nuclei as a bright point source on top of the background host galaxy in the AOB and HST images. Although with the near-IR, we might expect to observe an unresolved nucleus in some Seyfert 2 cases with the deeper views through the dust, our results confirm that the non stellar AGN continuum is not viewed directly in Sy2 nuclei, even with a factor of almost 10 greater dust penetration of the K- over V-band.

The ability to discern the bright central point sources in the Seyfert sample can be used as a method

of categorizing the Sy1's. As the F606W filter provides a reasonable estimate of the flux seen by the wavefront sensor (WFS), we found that we can use the fiducial value of $\sim$ 50 WFS counts as a measure of whether the HST images will have saturated versus unsaturated nuclei (i.e. $>$ 50 counts corresponds to a saturated HST nucleus). Following Malkan et al. (1998), when a nuclear point source is evident, we categorized it as either a Saturated Sy 1 (SS1) or Unsaturated Sy 1 (US1). The remainder of the galaxies which were identified as Sy 1 but showed no discernible point source are designated Resolved Sy 1 (RS1). For the 8 galaxies imaged by HST but not in the Malkan sample, we supplied optical classifications based on this system as well. In no cases did we classify a galaxy RS1 when the HST classification was US1. We are thus confident that poor AOB correction did not result in an erroneous classification based on the central AGN source.

If there is actually a buried point source in these galaxies, it must typically contribute less than about 30% of the light within the inner 1″. This was verified in several resolved cores where the AOB correction provided a resulting resolution element of $<$ 0.″2. We first produced a surface brightness profile of the galaxy, and another one for the PSF. The actual PSF was approximated using either a calibration star, or a model-constructed PSF (see chapter 3 and Veran et al. 1998). The model PSF will be the closest to the actual PSF in the image, provided the guide source is $\sim$50 WFS counts or more. The PSF was then scaled to match the peak of the galaxy brightness. Both profiles were integrated up to a radial distance of 1″. As an example, NGC 2992 could have an unresolved component contributing 38% at H-band in a 0.″2 diameter aperture, and 17% in a 0.″5 aperture.

We note that there is only one galaxy in our sample where an unresolved nucleus had a Seyfert type larger than 1.5 (Mkn 744 - SS1.8). However all 4 of the RS1's have Sy1.8 or Sy1.9 designations. This trend is confirmed in the results of Malkan et al. (1998). The implication is that the intermediate Seyfert classification system (*ie* 1.8 to 1.9, Goodrich 1995) appears to map onto the resolved/unresolved nucleus classification system. In addition, this implies that RS1's may be closer to Sy2's than the unresolved Seyferts given the tendency for relatively weaker BLR's. We will explore these implications in later sections.

6.2.2 Suitability of our sample for statistics

We noted in chapter 2 that our Seyfert sample suffers some selection biases. The principal one is that Sy2s are less likely to be included unless they are relatively prominent, whether because they fall under the limit of the magnitude cut for the RSA sample, or because they were not peaked enough for AOB

Table 6.1: Seyfert Classification Criterion

Classification	Description
SSy1	nuclear point source is evident, saturated in HST image, WFS counts > 50 on AOB.
USy1	nuclear point source is evident, unsaturated in HST image, WFS counts < 50 on AOB.
RSy1	identified as Sy 1 but showing no discernible point source
Sy1	Objects showing broad Hβ emission line and with [OIII]/Hβ < 0.3
Sy1.2	broad Hβ and with [OIII]/Hβ < 1
Sy1.5	broad Hβ and with 1 < [OIII]/Hβ < 4
Sy1.8	broad Hβ and with [OIII]/Hβ > 4 Hβ with decreasing ratios of [OIII]/Hβ
Sy1.9	detectable broad line component only in the Hα line
Sy2	[OIII]λ5007 to Hβ ratio > 3, and [NII]λ6584 comparable to Hα

guiding. Although this could lead to comparing Sy1s with Sy2s which are intrinsically more luminous, our sample appears to have similar distributions in radio flux and in [OIII]λ5007 emission line flux as described in chapter 2. Both of these are thought to be more or less orientation independent (Ulvestad & Wilson 1984, Ulvestad 1986, Dahari & DeRobertis 1988). We caution, however, that our sample has relatively small numbers for statistical purposes.

A further bias exists in the varying spatial resolution achieved in our sample, due to the changing weather conditions and differing guide strengths of the galaxy nuclei. The mean correction is 0.″23 with a range of 0.″14 to 0.″35 in the images used to classify and search for unusual structures.

In table 6.2, we compare the Seyfert class and median redshift of our sample to that of the 205 HST-imaged Seyfert galaxy sample of Malkan et al. (1998). Although the numbers are much smaller in our sample, there is no obvious distance bias beyond that of Malkan et al. (1998). We do have a slight excess of Saturated Seyfert 1 (SS1) galaxies, chosen since they provide the best AOB guiding candidates.

The Sy1/Sy2 ratio in the Malkan sample is 1.2/1, whereas the Maiolino et al. (1995) sample has a ratio of 1/1.5. Our sample has 1.3/1. If we include Sy1.8 & Sy1.9 in the Sy2 category, the numbers change to: 1/1.3 (Malkan), 1/4 (Maiolino) and 1/1.6 (Chapman). Both the Malkan and Maiolino samples purport to be relatively bias free, yet contain rather different classification ratios. This has important implications in discussing the applicability of torus opening angles to unified models. Some of the discrepancy is likely due to the different information and wavelength regions used in making classifications. Moreover, the above reaffirms the fact that choosing any unbiased sample of AGN is a difficult endeavor. At mid-IR wavelengths (the IRAS 12 μm sample - Malkan et al. 1993), there is an

Table 6.2: Statistics of Seyfert Classifications

Classification††	number AOB	Median z AOB	Number HST†	Median z HST†
SSy1	10	0.0095	30 (38%)	0.023
USy1	4	0.0105	14 (18%)	0.024
RSy1	7	0.0096	34 (44%)	0.025
Sy1	21	0.0097	78	0.019
Sy2	16	0.0081	99	0.016

† NOTE: HST sample corrected for distance bias (Malkan et al. 1998)
†† when a nuclear point source is evident, we categorized it as either a Saturated Sy 1 (SS1) or Unsaturated Sy 1 (US1). The remainder of the galaxies which were identified as Sy 1 but showed no discernible point source are designated Resolved Sy 1 (RS1).

excess of star formation and bright nuclei (Maiolino et al. 1995). The UV and Xray regimes favour type 1 Seyfert galaxies. Our particular sample appears relatively consistent with other chosen samples for Seyfert class distributions.

6.3 A Galactic Dust Model

6.3.1 Introduction

In the standard unified Seyfert model, the obscuring torus is proposed as a small extension of the central engine, which is relatively independent of the host galaxy. The implications are: 1) the obscuring torus will be too small to detect at typical scales of a few tens to a hundred parsecs probed by HST/AOB imaging; and 2) it will not be connected with the galactic dust lanes which can be observed hundreds of parsecs away from the galactic center. Therefore any differences between Seyfert 1 and 2 nuclei should not be manifest on the larger size scales probed by HST/AOB images.

Malkan et al. (1998) found that these expectations are not borne out by their HST optical observations. They observe instead a higher incidence of irregular dust absorption in the centers of Seyfert 2 galaxies. This suggests that in some cases the source of the nuclear extinction is directly observed as interstellar dust clouds which intercept our line-of-sight to the nucleus. These dust lanes are seen on scales of hundreds of parsecs, and may therefore have *little or no physical connection with the central engine.*

Their data therefore suggest that the difference in apparent nuclear dustiness between Sy1 and Sy2

galaxies does not result from viewing angle, but because *a greater fraction of the sky as seen from a Seyfert 2 nucleus is blocked by obscuration.* This is at least a complication to the simple "unified scheme" in which Sy2's are intrinsically identical to Sy1's except for the angle at which they are viewed.

This alternative to the ATM, the Galactic Dust Model (GDM), is illustrated schematically in figure 6.2. The figure depicts a central engine consisting of a black hole/accretion disk, but no dusty obscuring torus, oriented randomly with respect to the galaxy disk. Dust clouds arranged in a spherically symmetric patchy distribution result in a range of possible classifications depending on viewing angle. Those Seyferts which are classified as type 2 are more likely to have larger *dust covering fractions* than the average type 1's.

6.3.2 Testing the galactic dust model

The GDM can be considered a viable alternative to standard unification paradigms (i.e. ATM) if galactic dust outside the nucleus can produce sufficient extinction to transform a Sy1 nucleus into a Sy2. The amount of extinction required dictates the preferred technique to probe how much might plausibly be available on scales of a hundred parsecs. Extinction is usually measured by its dimming effect on a source, given in V-band magnitudes, A_V. Sy1 nuclei would typically have to suffer more than several magnitudes of visual extinction to appear to us as Sy2's. This is precisely the realm of sensitivity of the near-IR colours, given the extinction curve through these wavelengths (Rieke & Lebovsky 1981). The nature, scale and distribution of the obscuring medium must then be addressed.

If the visual extinction were to reach A_V of 25 to 50 magnitudes, even deep infrared searches at longer wavelengths ($\lambda > 10\,\mu$m) would likely not be able to detect buried Sy1 nuclei (Ward et al. 1991). However, even if the extinction is above A_V of 10 magnitudes, the UV and visible traces of a Sy1 nucleus (broad lines and compact continuum) would be substantially obliterated. These extinctions would completely block soft X-ray emission from the nucleus. Assuming a normal Milky-Way dust/gas ratio as well as normal dust (grain size, composition, emissivity), the visual extinction implied by the hard X-ray column densities is given by $A_V = 5 \times 10^{-22} N_H$ (Mulchaey et al. 1992). Therefore, for a typical Sy2 galaxy, the line of sight to the center would need to intercept 0.2–1.0 $\times$ 10^{23} atoms cm^{-2}. Such column densities are roughly consistent with the average values inferred in Seyfert 2's from limited hard X-ray spectroscopy (Awaki et al. 1991, Mushotzky 1982, Mulchaey et al. 1992).

Our line-of-sight (LOS) to the galactic nucleus would have to intercept roughly 10 diffuse molecular clouds, or a single dense molecular cloud core to result in the amount of extinction required for a typical

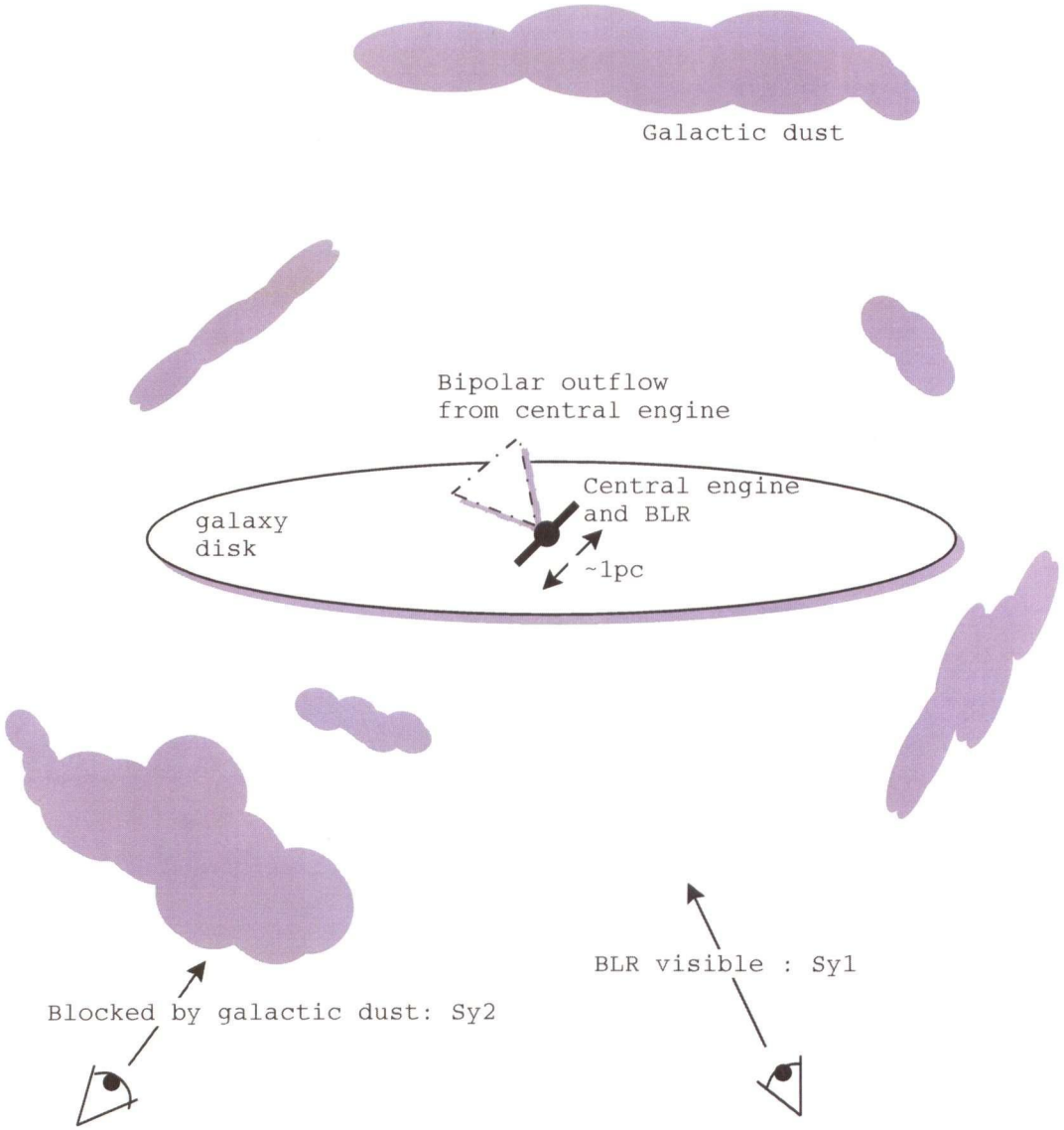

Figure 6.2: Schematic of GDM, adapted from Malkan et al. (1998) showing the outer galactic dust clouds drifting over the view to the central engine. A central engine consisting of a black hole/accretion disk but no dusty obscuring torus, is oriented randomly with respect to the galaxy disk. Dust clouds arranged in a spherically symmetric patchy distribution result in a range of possible classifications depending on viewing angle. Those Seyferts which are classified as type 2 are more likely to have larger "dust covering fractions" than the average type 1's.

Sy2 galaxy (Malkan et al. 1998, Morris et al. 1996). For a Milky-Way-type disk this would occur at a radius of about 100 parsecs. At this point, the vertical extent of the molecular gas is comparable to the distance from the nucleus (Sanders, Solomon, & Scoville 1984). The average surface density of molecular gas in the inner 500 parsecs of the Milky Way corresponds to $N_H = 4 \times 10^{22}$ atoms cm^{-2}, and this value is probably typical. In Maffei 2 (a nearby spiral galaxy) for example, the column density is 10^{23} in the inner few hundred parsecs (Hurt 1994).

If the GDM is truly causing the absorption, then there should be no preference for dust to lie exclusively over the nuclear point source - the A_V should be similar in several patchy regions near the nucleus. Nor should it necessarily appear confined to the disk plane. Our strategy will then be to probe the circumnuclear regions of our galaxy sample, constructing near-IR maps to highlight the extinction.

6.4 Developing Extinction Maps

6.4.1 Considerations

The H and K near-IR bands are the best to probe the levels of extinction (several magnitudes) typically required by unified models. An extinction curve from the optical to the infrared is plotted in figure 6.3 (Rieke and Lebofsky 1985, Candelli, Clayton and Mathis 1990). This shows that the relative extinction at K-band (A_K) is almost 1/10 that at V-band. This is clear in our images, where the effects of dust absorption become noticeably less with increasing wavelength. K-band images typically having the most symmetrical appearance, with disk emission extending through optically prominent dust lanes.

The extinction at a some wavelength is related simply to the optical depth at that wavelength through the relation

$$A_\lambda = -2.5 \log(I_\lambda / I_\lambda^0) = 1.086 \tau_\lambda$$

where I_λ is the intensity received by an observer from a star that emits an intensity I_λ^0, and is related by

$$I_\lambda = I_\lambda^0 \exp -\tau_\lambda$$

Thus a given wavelength is only sensitive to a limited amount of extinction before the number of photons penetrating a dust cloud becomes exponentially small. We use the point at which the number of photons arriving on the detector has dropped to a few percent of the intrinsic luminosity (3 e-folds) for a fiducial of the extinction sensitivity. The sensitivity of the different wavelengths to different amounts of extinction breaks down roughly as follows: optical: tenths of A_V, near-IR: few to 10 A_V, mid-IR: > 10

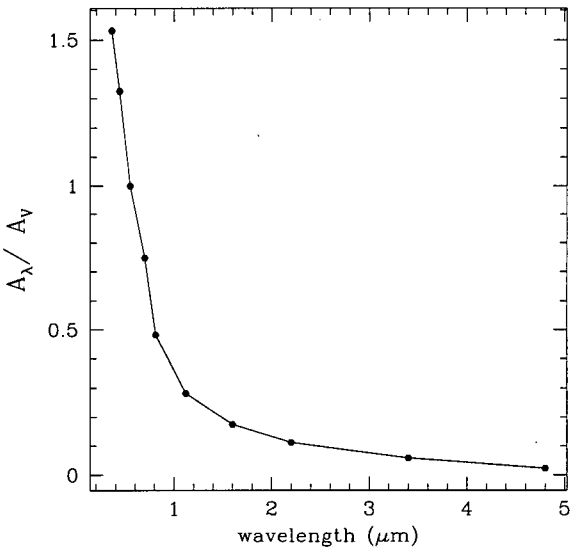

Figure 6.3: Empirical extinction curve adapted from Rieke and Lebofsky (1985), following roughly the $1/\lambda$ variation predicted if the dust grains are roughly the size of the light wavelength ($\sim 10^{-5} cm$). See also Candelli, Clayton and Mathis (1990).

A_V. Figure 6.4 illustrates the sensitivities of the different wavelength regimes to dust absorption, where an arrow which terminates within a dust cloud has effectively been blocked by the amount of implied extinction.

In addition to the optical depth effect, shorter wavelengths have strong contributions from patchy hot OB stars, and are contaminated by pronounced emission line regions. Near-IR wavelengths are dominated by the light of a more smoothly distributed older stellar population (McLeod & Rieke 1995). Even longer wavelengths ($> 3\mu$m) begin to be dominated by thermal emission from hot dust.

From an observational perspective, we are only sensitive to changes across a given wavelength range. Thus the best diagnostic of dust absorption is the reddening in a given colour relative to the fiducial color of an unreddened stellar population. Although longer wavelength baselines in principle provide a superior diagnostic, they probe substantially different emission processes in the two wavelength regimes. In addition, the differences in optical depth may lead to sampling differing morphologies within the galaxy. However, a long wavelength baseline such as V-K provides a slowly varying reference (K) over which the V-band extinction and morphology can be studied. Thus a combination of the near-IR colour H-K, and an optical-nearIR color (such as V-K) provides a valuable comparison, keeping the above in

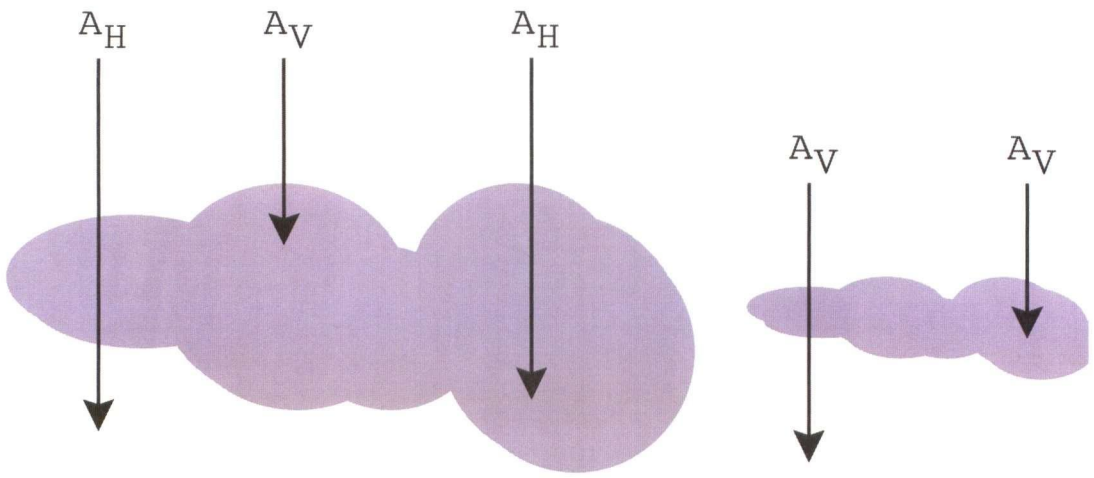

Figure 6.4: Cartoon illustrating the line of sight interception by dust clouds at optical (A_V) and near-IR (A_H) wavelengths. The dust clouds could represent either a torus structure surrounding the central engine, or the patchy distribution expected in the GDM scenario. An arrow which terminates within a dust cloud has effectively been blocked by the amount of implied extinction.

mind. Figures 6.14 through 6.25 show H-K and V-K colour maps. The colour scheme is in magnitudes with redder colors set to red or dark, and bluer colours lighter.

6.4.2 Extinction maps

By referencing fiducial colours of stellar populations to the actual observed colours, we can estimate the extinction due to dust. The H-K colour map is in general superior to J-H for characterizing the extinction because it probes deeper within the dusty regions. Using the J-H map typically results in an extinction estimate which is lower, likely as a result of the difference in optical depth. We expect this to be the case since the shorter wavelength filters effectively *saturate* with less dust absorption, in the sense that nothing behind the dust cloud is detectable.

However the K-band may be contaminated by hot dust ($\sim$1000 K) emission, resulting in possible overestimates of the extinction. L-band and CO-narrowband imaging can discriminate thermal dust emission from stellar emission (see chapter 4 and Alonso-Herrero et al. 1998). However the CFHT is not optimized for long wavelength L-band work, and CO-narrowband is expensive in terms of time required to obtain an adequate signal-to-noise ratio. None-the-less, the advantages of a smaller optical depth outweigh the possible hot dust emission. Alonso-Herrero et al. (1998) have shown that the hot dust contribution is relatively small for many of our galaxies relative to the stellar colours.

We assume that the colours of a typical early-type bulge stellar population are $H-K=0.2, J-H=0.78, V-K=3.2$ (Glass & Moorwood 1985), and that redder colours imply some degree of obscuration. With contributions from hot, clumpy OB stars, such as in Starburst or HII galaxies, V-K must be < 2 before the near-IR colours are affected substantially (Thuan 1983, Glass & Moorwood 1985). K-corrections (for redshift effects) are minimal for the implied distances of our sample, with factors of 0.5, 3, 5.1 $\times$ z for J-H, H-K and V-K (Thuan 1983). Galactic reddening for the latitudes of our sample galaxies is also small relative to the extinction in the Seyfert cores ($\tau(b) = \tau_1 \csc b$, where b is Galactic latitude and $\tau_1 = 0.37$ at V (Glass et al. 1985)).

Taking into account that the differential extinction between H and K is $A_H = 0.175 A_V$ and $A_K = 0.112 A_V$ (Rieke & Lebovsky 1985), we find $A_V = A_{H-K}/0.063$ in magnitudes.

$$A_{H-K} = -2.5\log(\frac{f(H)}{f(H_0)}) + 2.5\log(\frac{f(K)}{f(K_0)})$$
$$= -2.5\log(\frac{f(K_0)}{f(H_0)}) + 2.5\log(\frac{f(K)}{f(H)})$$

where $f(K_0)/f(H_0)$ is the flux ratio corresponding to $H-K=0.2$.

Similarly,

$$A_{V-K} = -2.5\log(\frac{f(K_0)}{f(V_0)}) + 2.5\log(\frac{f(K)}{f(V)})$$

with $f(K_0)/f(V_0)$ corresponding to $V-K=3.2$. Then $A_V = A_{V-K}/0.89$ in magnitudes.

6.4.3 Checking extinction maps for non-stellar components

The above analysis is only true for extinction of the stellar light. Other emission processes (power-law, nebular, etc.) will skew the results. The J-H and H-K colours can show regions which are difficult to explain only by reddened stellar colours. The J-H, H-K colour plane can also be mapped onto the image proper to form a *chromatogram* (see chapter 5, NGC 3227) to see if colours are expected to be partially non-stellar in various regions. Although we do not have J, H, and K images for our entire sample, we use the colour maps when available are used to search for structures and regions which should be excluded from the dust extinction analysis. In some cases, the strong Hα contribution in the HST F606W images can point to nebular colours in HII regions, or in the AGN continuum ionized NLR's. The results are tabulated in tables 6.5 & 6.6.

6.4.4 An index of dust patchiness

In the absence of any standardized classification for dust absorption in galaxies, we have attempted to outline a graded system which differentiates the amount of absorption and degree of patchiness associated with the presence of dust.

As outlined above, the degree to which a galaxy shows a patchy morphology due to dust absorption is strongly dependent on the optical depth afforded by the probing wavelength. Whereas the optical wavelengths are highly sensitive to small variations in dust absorption, the longer near-IR wavelengths require substantial variations in dust optical depth to demonstrate a sizable spatial variability in dust patchiness. Thus the scenario often exists where the optical image is high distorted and irregular, while the near-IR shows smooth elliptical profiles, virtually free from apparent patchy dust effects.

Nonetheless, the degree of general obscuration in the core region of Seyfert galaxies is best characterized through a longer wavelength analysis, showing the true degree of dust present along lines of sight towards the nuclear region. The spatial variability of the optical images (using the near-IR as a reference) can then be used as an additional aid to measure the degree of patchiness in conjunction with any irregular morphology in the near-IR maps.

We formulate a dust patchiness index (DPI) for both the near-IR and optical wavelength regimes, tabulating the results in tables 6.5 & 6.6. Both colour maps and model image subtraction (filtering the low spatial frequencies) discussed in chapters 3 through 5 are used to analyze the images for structures resulting from dust absorption or other processes (starbursts, nebular emission, hot dust, etc.). In the absence of multiple near-IR filters for some objects in our sample, only the techniques of model image subtraction are available to probe the single near-IR wavelength for underlying structure. The range of the index is chosen to cover the observed range of morphologies in our sample. Since dust can be associated with several different types of morphologies (dust lanes, circumnuclear clouds, rings of star formation etc.), we group all dusty structures together which are thought to result in a similar probability for nuclear coverage. Then any one criterion under a given heading is sufficient for that classification.

- $DPI = 5$ Prominent patchy dust is easily apparent over a large fraction ($> 1/4$) of the central $6''$. Clear examples of this type include the large-scale dust lane galaxies NGC 2992 and NGC 7582 where almost half the central region is obliterated by patchy dust. Galaxies such as NGC 3227 are also included with patchy dust in a more circularly symmetric distribution around the nucleus.
- $DPI = 4$ An easily recognizable *distorted morphology*, but where the dust covering fraction is

clearly not dominating the central 6″ . Examples of this type include the small-scale dust lanes in objects such as NGC 5929, or the distorted dust tracks in NGC 1386, and NGC 7465.

• $DPI = 3$ There are signs of patchy dust, but they are not obvious in a raw image and are only verified in the higher contrast colour maps. Dust associated with spiral arms or bars is traceable down to the nuclear region, which distorts the recognizability of the features. Examples of this type include Mkn 766 and NGC 7743.

• $DPI = 2$ There are small signs of patchy dust but at a lesser degree than $DPI = 3$. There are spiral arms or bars traceable down to the nuclear region but they do not appear be distorted or patchy as a result of dust. NGC 3516 and NGC 6814 are of this type.

• $DPI = 1$ There is no sign of dust present in the central 6″ region, with regular elliptical isophotes being a good fit to the core. There may be normal spiral galaxy features at larger radii but they cannot be traced down to the core region. NGC 3998 and NGC 5548 are characteristic examples.

We then form a global dust index (GDI) consisting of dust patchiness coupled with the magnitude of extinction seen regardless of dust morphology or spatial variability:

$$GDI = (DPI_{nearIR} + DPI_{optical}) * A_{V,max} * \kappa$$

The $A_{V,max}$ is the largest extinction observed in the central region ranging from $\sim$ 1 to >10 for our sample. The GDI is normalized against the DPI with the factor $\kappa = 0.5 * 14.3^{-1}$ which divides the GDI by 2 to account for the two DPI factors and by the maximum A_V found in our sample (A_V=14.3). The empirical index, GDI, provides a measure of the total dust present weighted by the chance that the dust might have a high probability of obscuring the nucleus.

When the DPI_{nearIR} and $DPI_{optical}$ are both large, the GDI is larger to acknowledge the extreme patchiness present, with some regions which are virtually free of dust and others with enough dust to block the near-IR. In the event that the A_V is less than the A_K, the GDI assumes a larger value based on the assumption that the optical wavelength has *saturated* and the near-IR is providing the true extinction.

6.4.5 Contamination from bright nuclei

The search for the signatures of dust absorption near the cores of Seyfert galaxies is inevitably hampered by the bright AGN dominating many of the Seyfert 1's. There may be some degree of bias associated with the detection of unusual, low contrast structures of any sort in Seyfert 1 cores. These include the

expected structures in AGN models such as small-scale bars, dusty tori, nuclear disks, and anisotropic emission line regions.

In addition, the measurement of colour gradients or excesses in the core regions will be contaminated by the bright non-stellar point source. The effect on our dust extinction maps is a contributing colour from the AGN continuum in the form of a power law $F_\nu \propto \nu^\beta$ with $-2 < \beta < -1$ empirically (Glass & Moorwood 1985).

However, in addition to the deeper view through the dust afforded by the near-IR, the contrast of the galaxy light to the nuclear point source is improved relative to the optical wavelengths. This is because the stellar emission from older stars peaks in the H-band, while the AGN continuum and thermal dust emission are at a minimum (McLeod et al. 1995). We therefore firstly expect to have less difficulty identifying features near the nucleus in our near-IR images than in the optical HST images. Secondly, the contamination of the near-IR colours is expected to be less than in the case of the optical colours. We test this in the following simulations.

We added observed point sources to a subsample of representative Sy2 and Sy1.8/1.9 images, thus converting them into artificial SS1's. Figure 6.5 shows the effect of adding a bright point source to the center of a dusty Sy1.9 galaxy. Even when the unresolved core is 150 times brighter than for NGC 2992, distorted isophotes deviating from elliptical symmetry, caused by a feature 10% the peak flux, are still identifiable at a distance of 0.6″ . In fact, a bright Sy1 nucleus such as NGC 4051 is only 15 times brighter than the NGC 2992 core at H-band. At this level even the faint emission extending northwest into the dustlane is visible in the contaminated image.

We also probe the colour contamination near the core by adding a similarly scaled V-band PSF to the V-band NGC 2992. Figure 6.6 shows the results of this test. The loop morphology to the northwest (<1% the peak flux) is still clearly visible when the added PSF is 6 times the NGC 2992 peak flux. However, at 30 times the peak, the feature is difficult to recover, and at 100 times the peak it is obliterated by diffraction rings and PSF differences. The colours at a distance of 0.5″ from the nucleus vary by 40% in the extreme case from the actual colour map to the 100×peak PSF color map. At 1.0″ distance, the variation is about half as much. As the nuclei in our sample are typically no more than 15-30 times the strength of NGC 2992, we treat the 0.5″ radial distance as a reference for reasonable colour recovery in the presence of a bright point source.

Attempting to subtract a PSF from the unresolved Seyfert core inevitably leaves artifacts. This is especially true with the variation of correction level with atmospheric conditions and observed wavelength.

Glare from the imperfectly subtracted wings of the PSF remained, whether we used reconstructed PSF's (Veran et al. 1998) or calibration stars observed throughout our runs.

The addition of AO artifacts generated around the bright guiding source further complicates the reliable subtraction of a point source associated with an unresolved AGN. With an unknown contribution from the achromatic artifact, simply forming colour maps is likely the best way to reduce the contamination from the central spike to probe faint structures. The AO artifacts are likely to affect the interpretation of both the colours and morphology within the central arcsecond.

Despite these concerns, the Seyfert 1.5 galaxy, NGC 3227, has a bright unresolved core with almost 50% of the strength of NGC 4151 (the brightest nucleus in our sample). When colour maps are formed, we find NGC 3227 to be one of the dustiest, most distorted galaxy nuclei in our sample. In a few cases with low level structures, we expect we will not be able to identify them in the presence of a very bright AGN component. However at distances of 100 pc there should be little bias associated with bright point-source contributions.

6.5 Results

In tables 6.5 & 6.6, the extinction properties of each galaxy are outlined along with any features observed in the colour maps. The convention used when quoting colours in the non nuclear region is to give first the colour at the outer edge of the frame, with the colour range providing an indication on how much the colours vary over the central region. We attempt to exclude the region where a contribution from the nucleus is expected to be large. The maximum A_V is measured over a non-nuclear feature in all cases, since contamination of non-stellar colours in the nucleus makes it difficult to obtain an accurate extinction estimate. Most of the galaxies have H-K colours which rise steeply in the core region, likely as a result of power-law continuum emission, possibly scattered to a region beyond the central point source. If there was no clear extra-nuclear maximum in the H-K colour, the A_V was either taken over a maximum in the V-K colour, or else in the annulus with a minimum radius indicated by the point source contamination results in section 4.5 ($R_{min} \sim 0\farcs5$)

The DPI and GDI indices both take on a maximum value of 5. When the dust patchiness index (DPI) is low (1 or 2), the colour range likely indicates some degree of a stellar population gradient from the edge of the field towards the nucleus. For higher DPI values, the colour range is dominated by the patchy extinction. The results of the DPI analysis are summarized in table 6.3.

Table 6.3: Dust patchiness index results

Seyfert class	A_V ave/max	DPI_{nearIR}	DPI_{opt}	GDI^a
Sy1	4.1/5.2	2.2	3.1	1.3
Sy2	4.3/5.6	2.7	4.0	1.8
earlySy1[b]	2.9/3.8	1.4	2.6	0.85
SSy1	2.8/3.6	1.9	3.1	0.8
USy1	3.0/4.1	1.0	2.0	0.95
lateSy1[c]	4.4/5.7	3.8	4.2	2.9
RSy1	4.5/6.0	4.0	4.2	2.6
Sy2+lateSy1	4.7/6.9	3.0	4.1	2.15

[a] The *GDI* is only included for those Seyferts which have a near-IR estimate of the extinction, either from our data or the literature.
[b] Seyfert 1,1.2,1.5
[c] Seyfert 1.8,1.9
[d] SSy1, USy1, & RSy1 are classifications based on whether the nucleus is unresolved and saturated in the fixed integration time HST image (S), unsaturated (U), or resolved beyond the PSF FWHM (R).

The Seyfert sample as a whole has a very high fraction of galaxies showing signs of a dusty morphology in the core region. No Seyfert 2 has a $DPI < 3$ in the optical. Only 7 of the 19 Seyfert 1's have $DPI_{opt} < 3$, while only 2 have $DPI_{opt} = 1$. This would appear to distinguish them from nearby *non-active* spiral galaxies (Carollo & Stiavelli 1998a, 1998b). However, such speculation must be tempered with the lack of a well-matched sample of non-active spirals at similar resolution and wavelengths with which to compare nuclear properties.

Amongst the Seyferts, the resolved Sy1 (RS1), late Sy1 (Sy1.8/1.9), and Sy2 samples are all very similar in dust properties. However, the Seyfert 1 sample clearly stands out as less dusty, especially when the RSy1/late Sy1 samples are excluded from the analysis. The dusty morphologies would usually not be observable with lower resolution imaging due to the small spatial scales or low contrast of the features.

The global dust index (*GDI*) provides a similar trend to the dust patchiness indices. However, the discrepancies between classes are no longer as pronounced, likely because the estimates of maximum extinction are unreliable in some of the galaxies with strong nuclei or non-stellar colours in their circumnuclear regions.

In our entire sample, 15 of the Sy2 (83%) show clear signs of dust lanes or irregular absorption patches which are not associated with spiral arm or other well defined morphologies. Of the 3 less-dusty

Sy2, two show a clear linear structure over the center (Mrk 3 and Mrk 620). The results of Maiolino et al. (1999) showed a clear trend for higher X-ray column densities in barred Seyferts. The known behaviour of a bar to funnel material towards the center is indirect evidence that in these cases, dust and gas are likely present to obscure the nucleus, despite a lack of patchy dust morphology in the circumnuclear regions.

The results for Sy2s are compared to 10 of the total Sy1 sample (53%) showing dusty morphologies. For the late intermediate Sy1 types (1.8/1.9), 6 out of 7 show extreme patchy dust. When these are included in the Sy2 sample, 21 out of 25 (84%) show direct evidence for patchy dust, whereas the remaining Sy1 sample has only 4 out of 12 (33%) dusty nuclei. Using the near-IR/HST colour maps (typically V-H or V-K), 2 of the galaxies in Malkan's sample classified as non-dusty were found to show clear signatures of dust.

When restricted only to the near-IR imaging, fewer galaxies show patchy dust morphology. However, only 4 showed regions of dust extinction less than $A_V = 3$. This indicates that even when irregular dust does not block the near-IR view, it does not necessarily mean that the GDM is not applicable.

Our near-IR colour map results are stronger than the results obtained from the HST F606W filter data alone (Malkan et al. 1998) where 45 of the Sy2 sample, comprising 39%, showed such dust features, compared to 23% of their Sy1 sample. However, the numbers of galaxies are about 5 times less in our sample.

Thus the results from this analysis indicate firstly that Sy2 appear dustier than Sy1 on the average. The Sy1's with the strongest nuclear sources (ie: SSy1) have a deficiency of dust relative to Sy2. This does not appear to be a result of glare from the unresolved point source (section 4.5). Secondly, the Sy1.8/1.9 and RS1 subsamples are clearly closer to Sy2 than Sy1 in optical through near-IR wavelengths as far as their dust properties are concerned. Within the Sy1 galaxy types, the bright unresolved nuclei are anti-correlated with larger intermediate classifications (i.e. Sy1.8/1.9). Since the intermediate Seyfert types indicate weak, partially extinguished broad lines, the nuclei are most likely being reddened by dust. Given that the dust magnitude and patchiness in the nuclear regions support this trend, this is further evidence in favour of a GDM scenario.

6.6 Discussion

6.6.1 Applicability of GDM

We see from the results of the extinction analysis that the amount of dust present in the circumnuclear regions of these Seyfert galaxies appears to satisfy the requirement for a GDM picture in many cases. In the cases where even the near-IR images show a patchy morphology as a result of dust absorption, the GDM model is exceedingly likely, since the implied dust distribution suggests the possibility of nuclear coverage, as we shall discuss below. Certainly in the HST images, and often in the near-IR as well, the interstellar dust frequently appears disturbed. A highly disturbed morphology in the near-IR requires large amounts of extinction in a very patchy distribution given the small optical depths of dust clouds to near-IR photons. The implication is that the morphology is likely not consistent with a *thick slab* in the plane of the disk. Rather it is more suggestive of a randomly distributed morphology in the circum-nuclear region.

However, there are a few examples of Sy2's in our sample, having an average A_V of only a few magnitudes, which do not show any circumnuclear dust morphologies capable of providing the necessary obscuration for a true Seyfert 2 classification, were they to reside directly along our line-of-sight (LOS) to the nucleus (these will be further explored in the next subsection). For these Seyfert 2, the ATM may indeed be a more relevant picture of the nuclear obscuring medium. For the near-IR estimates of extinction, we see N(H)$\sim 10^{22} cm^{-2}$ with a few magnitudes A_V. At this level, there would be no more broad Hβ, no UV emission, and perhaps even some reduction of the broad Hα wings. X-rays >1keV would still be visible at this level however. This is still less A_V than required to totally wipe out a Seyfert nucleus, resulting in a true Seyfert 2 classification. Thus for cases where there is a more uniform distribution of dust providing a few magnitudes A_V over the core region could result in a Seyfert 2 classification at a casual inspection (in this context meaning the absence of near-IR spectroscopy, or X-ray observations).

By contrast, there are also cases where a prominent dust lane or cloud crosses the nucleus, such as the Sy2's NGC 1386 and NGC 5929. These galaxies are all heavily absorbed X-Ray sources (Mulchaey et al. 1992). In these cases, it is this dust-lane which appears to have obscured the point source and the BLR, leaving only the hard X-ray emission from the central engine. Other RS1's or Sy1.8/1.9 galaxies have a large amount of dust which appears to severely redden the nucleus, but just misses complete obscuration. Certainly these examples (e.g. NGC 2992, NGC 5506, NGC 5033) provide good evidence

for a GDM over any well defined torus model (such as that proposed in Maiolino et al. 1995). This also further supports the notion that RSy1 and lateSy1 types are closer to Sy2 than Sy1. From the morphology alone, the SSy1 galaxy IC 4329a might be expected to join the ranks of the above examples given the dust lane crossing the nucleus. In this case, a combination of a bright nucleus coupled with a dust lane which does not have the near-IR deduced A_V of the other examples, and may be more patchy at smaller scales than it appears to be with our resolution, likely allows the full Sy1 nucleus to be observable. There are also examples where such patchy dust is within ~ 100 pc of the nucleus but does not affect the signatures of a Sy1 (e.g. NGC 3227 and NGC 4051). These must also be considered strong evidence in favour of a GDM picture since the dust might conceivably drift over the nucleus with time. Indeed the classification of NGC 3227 has a fair amount of discrepancy from its original classification as a Sy2 (Seyfert 1943) and throughout the last couple of decades (Gonzalez-Delgado et al. 1997) where it currently is classified as Sy1.5 - a clear view of the broad line region.

At some level, the *DPI* indices are indicating the covering factor of dust morphologies relevant to GDM. In other words, this is the fractional volume occupied by clouds with an optical depth exceeding the limit necessary to obscure the Sy1 nucleus. However, the *DPI* on its own does not constrain the possibility of a uniform dust distribution, which our near-IR estimates show to be relevant for nuclear obscuration in some cases.

The question is, what do the dustlanes look like at say another factor of 10 improvement in spatial resolution. We know that dust lanes and dusty regions in nearby galaxies as well as the Milky Way are in fact very patchy (Morris and Serabyn 1996). Thus there remains the question of line-of-sight (LOS) to the nucleus. Even finding a dust lane actually crossing the nucleus, with an extinction large enough to quench much of the type 1 AGN signature, does not guarantee that sufficient dust is crossing the very small pencil beam of our instantaneous LOS. However, even when there is no direct circumnuclear evidence for GDM to apply, the trends in the entire sample suggest that there might indeed be dust on smaller scales which we are not sensitive to with our current resolution. Thus we cannot rule out that a GDM scenario is in fact operating in all the Seyfert galaxies, as opposed to an ATM.

We can attempt to use the available information to put a limit on the cloud size. This, along with typical cloud velocities, yields an estimate of the expected time variability of the nucleus. Assuming a cloud velocity of 1000 km/s, a time of $\sim$1000 years is required for a dust cloud to move 1 pc. If an obscuration sufficient to block out the Sy1 features is suffered towards the nucleus, corresponding to $N_H \sim 10^{23}$, then the density $n_H = 3 \times 10^6\,\mathrm{cm}^{-3}$ along with a mass of $m_H \sim 2 \times 10^{-24}$ gm, provides a

hydrogen density of $\rho_H \sim 6 \times 10^{-18}$g cm^{-3}. For an implied cloud volume of 10^{50} cm^3, the cloud mass is m_c=6×10^{32} gm or $1/3\,M_\odot$. The speed may therefore affect variability, but only if the clouds are small. This size is reminicent of Bok globule clouds observed in our galaxy (see for example Santos et al. 1998). Thus we would expect to see variations of Seyfert type on time scales of 10's of years under these assumptions. This is indeed the case for some Seyfert galaxies (NGC 3227 as described above), although variations in classifications through the literature may generally have more to do with different observing techniques and wavelength regimes.

Even if we are to assume that there is in fact a lot of dust crossing over the nucleus, it is still not clear that it is really the 10^{23} or 10^{24} N(H) required if even the hard X-rays are to be obscured. In at least some cases, a model incorporating an opaque nuclear torus (the ATM) may have to be invoked for Sy2's which have Fe Kα emission lines of enormous equivalent width, implying an obscuration by $N_H \geq 10^{24}$ cm^{-2} (NGC 1068 for example - Smith, Done, & Pounds 1993). The resulting A_V of several hundred is well beyond anything observed in our sample, although the near-IR is not very sensitive beyond a few 10's of A_V.

Thus we are finding excessive patchy dust near the Sy2, Sy1.9, and Sy1.8 nuclei, compared to true Sy1's, and perhaps along the line of sight to the nucleus itself, using the extinction sensitivities afforded by the near-IR. Although this may not provide a ubiquitous picture of being able to turn any Seyfert 1 into a Seyfert 2 using GDM, it does point to the possibility that enough patchy dust could exist to accomplish this task in many cases. Mid-IR studies at a similar resolution would be necessary to verify whether the very high column densities, required by some hard X-ray studies, do indeed exist in some cases over patchy dust regions covering the nucleus.

6.6.2 Intrinsic differences

Our analysis has then shed some light on the important question of whether the particular type of active nucleus, type 1 or 2, is related to any property of the host galaxy. We have demonstrated intrinsic differences in both the dust magnitude and patchiness between nearby Seyfert 1 and 2 galaxies. These intrinsic differences also appear in the Hubble type with Sy1 being one morphological class earlier than Sy2.

Whereas the vast majority of Seyfert 2 galaxies show a patchy dust morphology in the core region, there are many Seyfert 1 which show little or no dust patchiness capable of obscuring the nucleus and these would likely never be classified as Seyfert 2 (examples include NGC 4151, NGC 5548, & NGC 7469).

These are to be contrasted with a sample of Seyfert 1 which are distinctly dusty at a similar level as Seyfert 2 (examples include both Syl-1.5 types such as NGC 3227, as well as Sy1.8-1.9 types such as NGC 5033). These could be considered *misclassified* objects in some sense, since they might just as likely ended up as Seyfert 2 had the dust clouds been distributed directly over the nucleus.

The conclusions about Seyfert dustiness being greater in Sy2's and some Syl's make the supposed distinction between Syl and Sy2 a rather hazy one. If our GDM speculation were entirely correct, then visibility of the Seyfert nucleus would be a *non-essential* means to classify these galaxies, since a dusty-type Seyfert galaxy could have a clear line-of-sight through the clouds to the nucleus. Rather, the way to classify these galaxies would be by the presense of a dusty core morphology (with say $DPI > 2$ and $GDI > 2$) 1) Dust-Free; 2) Dust-Enshrouded. Whether or not the actual nucleus is visible is a moot point for the classification. The implication would be that there is a bi-modal distribution of Seyfert types and perhaps active galaxies, which may be connected to the dynamical evolution of the galaxy leading to the production of excessive dust in the core region. This could in turn be related to the proposed connection between Starburst and Seyfert (i.e., Gonzalez Delgado et al. 1998) whereby recent star formation in the nuclear region would result in a dusty morphology capable of obscuring the nucleus.

Our conclusions about the viability of GDM should not be substantially affected by our major known sample bias - the selection of intrinsically more luminous Sy2's. There is no reason to suppose that more luminous Sy2's should have higher dust covering fractions than less luminous Sy2's. Thus the division of Seyferts by dustiness, rather than nuclear visibility, remains intact.

In at least a few cases, the presence of a linear structure lying over the nucleus (ex: Mkn 3, Mkn 1066, Mkn 620) suggests that material may be transported towards the nucleus as described in previous chapters. Such inflowing material may also be responsible for the nuclear obscuration resulting in the Sy2 classification of these objects. Recent studies in the X-ray of Sy2 galaxies (Maiolino et al. 1999) have indeed shown that the degree of line-of-sight obscuration is directly proportional to the strengths of larger-scale bars viewed in ground based images, where *strength* is defined in terms of ellipticity, position angle, and brightness profile arguments (Maiolino et al. 1999). Without higher resolution, however, it is impossible to discern whether it is the presence of a dusty torus or simply distributed dust clouds which causes the actual nuclear obscuration. Nonetheless, the connection of bars with nuclearly obscuration further supports the notion that evolutionary dynamics may be at the root of the increased nuclear dustiness in Sy2 and Sy1.8/1.9 galaxies.

Table 6.4: Descriptions of the central regions of the galaxy sample.

Galaxy	NIR description	resolution (FWHM)†	artifact	F606W description[a]
Seyfert 1				
ic 4329a	more extend to NE? red ring	diff. sat.	Y	DC, nearly edge on
MRK 744	blue rings E-elong. red disk to NW?	diffrac.	Y	DI
MRK 766	red core structures, normal, NE offset?	near diff.	Y	B, F/W, DI ?
MRK 1330	blue ring, spiral, blue NW NLR?	diff.	N	DC
NGC 1275	bright core	0.3"	Y	Wispy spiral
NGC 2639	normal, red extend SE, spiral arms?	0.2"	N	DC, flocculent
NGC 2992	SB on radio loops	diff.	N	DC
NGC 3227	spiraling SB knots,Jdusty,nuclear disk	diffrac.	Y	F/W, D-SW
NGC 3516	Blue S., bar?	diff.	Y	DI B?
NGC 3998	normal	diff.	Y	triaxial
NGC 4051	less dust, blue/red to N.	diff..	Y	D-SW
NGC 4151	core dom.	diff.	Y	normal
NGC 4968	normal, bar?	0.2"	N	DI
NGC 5033	asym core, edge on	diff.	Y	dustlane, core elongated N
NGC 5135	3 cores	0.45"	N	CL
NGC 5273	normal	0.25"	N	spiral
NGC 5506	outflows?	<0.25"	Y	DC, F/W edge-on
NGC 5548	R - SB knots, core extent	diffrac.	Y	normal
NGC 5728	bar 3"	<0.35"	N	bar, dusty
NGC 6814	smooth	0.25"	Y	traces of dust
NGC 7469	knotty HII ring, bar?	diff.	Y	R
Seyfert 2				
MRK 3	normal?	0.3"	N	F/W bright linear center
MRK 348	red bar, outflow	0.25"	Y	double nucleus
MRK 620	bars-in-bars	diff.(?)	Y	F/W center not extended
MRK 1066	red bar? flat central profile	diff.	N	F/W dusty
NGC 1068	bar, outflow?	0.25"	Y	very dusty, spiral
NGC 1241	possible nested bar	0.3"	N	dusty, spiral
NGC 1386	ellongated, knots?, smooth	<0.25"	Y	DC
NGC 3081	bar,spiral arms	<0.3"	N	DI
NGC 3393	bars visible	<0.3"	N	F/W, like Mkn573
NGC 5005	extended structure EW	0.3"	N	very dusty
NGC 5929	no dust lane,normal	0.25"	Y	DC
NGC 5953	elongated core?	0.3"	N	dusty, mini-spiral
NGC 7465	distorted, outflows?	0.2"	N	DI, B, collision?
NGC 7582	distorted/extended edge-on	0.2"	Y	DC, F/W, inclined dust d
NGC 7590	extended smooth	0.3"	N	DC
NGC 7743	smooth	0.25"	N	F/W, DI, early type

† The filter with the best resolution [a] comments adapted from Malkan et al. (1998).
DC - dust lane running across the center
DI - irregular dust
B - nuclear bar
F/W - filiments and wisps (emission lines)
CL - clumpy star formation

Table 6.5: Color features and extinction in near-IR

Galaxy	filters	colour range	nuclear color	A(V) ave/max	DPI_{NIR}	non-dust structure
Seyfert 1						
IC 4329a	H-K	0.2 - 0.5	2.2	2.4/4.8	2	none
MRK 744	H-K	0.4 - 0.8	0.8	6.3/9.5	3	rings, F/W
MRK 766	H-K	0.25 - 0.6	2.1	3.5/6.4	2	bar,F/W
MRK 1330	H-K	1.0 - 0.5	1.6	8.7/12.6	2	blue NLR, ctm regions
NGC 1275	K			0.1†	1	none
NGC 2639	H-K	0.35 - 0.3	0.4	1.5/2.4	2	red SE, mini spiral nucleus
NGC 2992	H-K	.34 - .85	1.1	6.1/10.3	5	jet, spiral arms
NGC 3227	H-K	0.27 - 0.72	1.15	3.4/7.0	4	spiraling SB knots, F/W
NGC 3516	H-K	0.5 - 0.45	1.5	2.2/3.17	1	blue south
NGC 3998	H-K	0.23 - 0.3	0.5	0.3/1.4	1	normal
NGC 4051	H-K	0.3 - 0.5	>1.2	3.1/4.7	1	bar? V-dust, blue N NLR?
NGC 4151	H-K	0.83 - 0.93	1.1	5.2/9.5	1	scattered AGN light
NGC 5033	H-K	0.4-0.8	0.5	7/9.5	5	red rings (J-K)
NGC 5273	H			1.0†	1	
NGC 5506	J	$H-K\sim 1.1^a$		14.2/1.3†	5	nucleus region distorted
NGC 5548	H-K	0.2 - 0.4	0.9	1.1/2.3	1	HII knots
NGC 5728	K	H-K$\sim 0.33^a$		2.1/1.0†	3	bar
NGC 6814	H-K	0.2 - 0.5	0.6	0.9/2.3	1	none
NGC 7469	H	H-K$\sim 0.4^b$	1.0	3.1/0.9†	1	HII knots, ring
Seyfert 2						
MRK 3	H-K	0.3 - 0.5	0.7	2.5/4.7	2	F/W bright linear center
MRK 348	H-K	0.3 - 0.4	0.66	2.8/4.1	2	double nucleus
MRK 620	H-K	0.3 - 0.6	0.54	3.2/5.2	3	bars-in-bars
MRK 1066	H-K	0.2 - 0.1	0.63	2.4/4.5	3	bars, F/W, spiral
NGC 1068	K	H-K=0.3-0.7^{a,c}	1.8	9/1.9†	4	spirals?
NGC 1241	H			1.7†	2	
NGC 1386	H-K	0.5 - 1.1	1.3	4.9/14.3	3	non-dust filaments?
NGC 3081	K	H-K$\sim 0.4^a$		3.2/1.1†	2	spiral
NGC 3393	K	H-K$\sim 0.3^a$		2.2/1.3†	2	F/W, bars , spiral
NGC 4968	H			1.2†	2	spiral
NGC 5005	H	H-K$\sim 0.3^d$		2.3/1.1†	3	distorted core
NGC 5135	K	H-K$\sim 0.5^e$		4.7/1.4†	2	SB knots, Clumpy
NGC 5929	H-K	0.22 - 0.6	0.9	2.1/6.4	2	
NGC 5953	H	H-K$\sim 0.61^b$		10/1.7†	3	HII ring? mini spiral arms
NGC 7465	H-K	0.3 - 0.6	1.1	4.3/6.6	4	none
NGC 7582	H-K	0.6 - 0.9	1.2	7.1/9.5	5	distorted nucleus, clump SF
NGC 7590	H	H-K$\sim 0.4^d$		3.2/1.1†	2	
NGC 7743	H-K	0.2 - 0.4	0.5	2.5/3.4	2	

(a) Alonso-Herrero et al. 1998
(b) Lai 1995
(c) Rouan et al. 1998
(d) NED photometry 10″ aperture.
(e) Kotilainen et al. 1993
† A_V estimated either from other near-IR colours and V-K or else just V-K

Table 6.6: Color features and extinction in optical/nearIR

Galaxy	filters	colour range	nuclear color	DPI_{opt}	GDI	non-dust structure
Seyfert 1						
IC 4329a	V-K	2.4 - 4.1	5.2	5	1.15	none
MRK 744	V-H	2.3 - 4.2	4.8	4	2.35	rings, F/W
MRK 766	V-K	3.25 - 4.1	4.4	3	1.1	bar,F/W
MRK 1330	V-K	3.1 - 4.5	4.2	3	2.2	blue emission line?
NGC 1275	V-K	2.6-3.3	2.6	2	0.01	HII knots
NGC 2639	V-K	2.4 - 4.5	3.1	3	0.4	red extend SE, mini-spiral
NGC 2992	V-H	2.9 - 6.3	3.4	5	3.6	jet, spiral arms
NGC 3227	V-K	3.5 - 5.4	5.5	5	2.5	spiraling SB knots, F/W
NGC 3516	V-K	3.0 - 4.2	4.5	2	0.35	blue to south
NGC 3998	V-K	3.3 - 3.6	3.7	1	0.1	normal
NGC 4051	V-H	3 - 4.5	4.7	3	0.65	bar, blue Northern region
NGC 4151	V-K	3.3 - 4.6	4.9	2	1.0	none
NGC 5033	V-K	3.1 - 4.9	3.2	5	3.3	F/W blue rings
NGC 5273	V-H	2.7 - 3.9	2.6	3	0.15	spiral, knots
NGC 5506	V-J	2.3 - 4.2	5.2	5	4.95	distorted nucleus
NGC 5548	V-K	3.1 - 4.4	4.6	1	0.15	HII knots
NGC 5728	V-K	3.1 - 3.9	4.2	3	0.35	bar
NGC 6814	V-H	3.1 - 4.2	4.8	2	1.25	none
NGC 7469	V-H	2.7 - 4.0	4.4	2	1.1	HII knots, bar/disk
Seyfert 2						
MRK 3	V-H	3.3 - 4.4	2.3	4	1.0	F/W bright linear center
MRK 348	V-H	4.1 - 4.9	5.3	3	0.7	double nucleus
MRK 620	V-K	4.2 - 4.4	4.5	3	1.1	bars-in-bars
MRK 1066	V-H	2.2 - 4.5	3.6	4	1.1	bars, F/W
NGC 1068	V-K	2.3 - 5.7	5.8	5	2.35	none
NGC 1241	V-H	3.1 - 4.6	3.9	4	0.35	spirals
NGC 1386	V-K	3.3 - 4.9	5.3	4	3.5	non-dust filaments?
NGC 3081	V-K	3.9 - 4.7	3.8	4	0.25	spiral
NGC 3393	V-K	3.6 - 4.6	3.9	4	0.3	F/W, bars, spiral
NGC 4968	V-H	3.0 - 4.5	2.8	4	0.25	spiral
NGC 5005	V-H	3.1 - 4.7	4.9	5	0.65	distorted core
NGC 5135	V-K	3.0 - 4.9	2.3	3	0.4	SB knots, CL
NGC 5929	V-H	3.7 - 4.8	5.2	4	1.35	HII knots
NGC 5953	V-K	3.5-4.6	4.9	4	2.45	HII ring, double nucleus
NGC 7465	V-K	3.1 - 4.8	5.3	4	1.85	F/W
NGC 7582	V-K	3.6 - 4.9	5.8	5	3.3	hot dust emission
NGC 7590	V-H	3.1 - 4.9	3.9	3	0.55	F/W?
NGC 7743	V-H	3.5 - 4.3	4.0	3	0.6	none

SEYFERT GALAXY FIGURE CAPTIONS

6.7 Seyfert 1 galaxies (arranged left to right down the rows) ic4329h, m744h, m766h, m1330h, n1275k, n2639h

6.8 n2992h, n3227h, n3516h, n3998h, n4051h, n4151h

6.9 n5033h, n5273h, m1376j, n5548h

6.10 n5728h, n6814k, n7469h

6.11 Seyfert 2 galaxies: m3h, m348k, m620h, m1066h, n1068k, n1241k

6.12 n1386h, n3081k, n3393k, n4968h, n5005k, n5135h

6.13 n5929k, n5953h, n7465h, n7582k, n7590h, n7743h

6.14 Seyfert 1 colour maps: (arranged left to right H-K, V-K unless otherwise noted in the galaxy label. There is one galaxy per row) ic4329hk, ic4329vh, m744hk, m744vh, m766hk, m766vk

6.15 m1330hk, m1330vk, n1275vk, n2639hk, n2639vh

6.16 n2992hk, n2992vh, n3227hk, n3227vh, n3516hk, n3516vk

6.17 n3998hk, n3998vh, n4051hk, n4051vh, n4151hk, n4151vh

6.18 n5033hk, n5033vh, n5273vh, m1376vj

6.19 n5548hk, n5548vk, n6814hk, n6814vk, n7469vh, n5728vk

6.20 Seyfert 2 colour maps: m3hk, m3vh, m348hk, m348vh, m620hk, m620vh

6.21 m1066hk, m1066vk, n1068vk, n1241vh

6.22 n1386hk, n1386vk, n3081vk, n3393vk

6.23 n4968vh, n5005vk, n5135vh

6.24 n5929hk, n5929vh, n5953vh, n7465hk, n7465vk

6.25 n7582hk, n7582vk, n7590vh, n7743hk, n7743vk

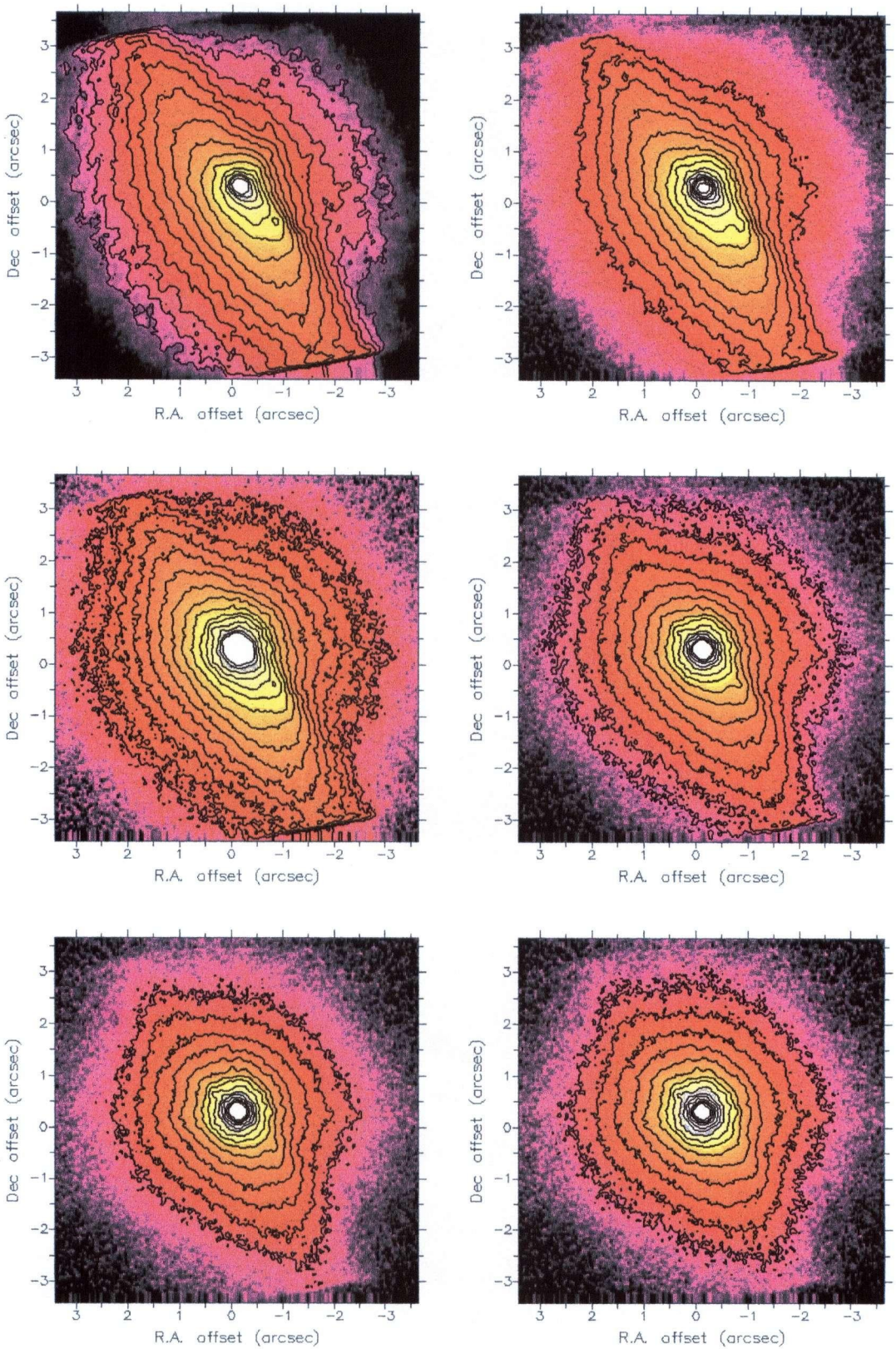

Figure 6.5: A bright AGN PSF added to H-band NGC 2992 at 6x, 15x, 30x, 50x, 100x, and 150x the peak flux

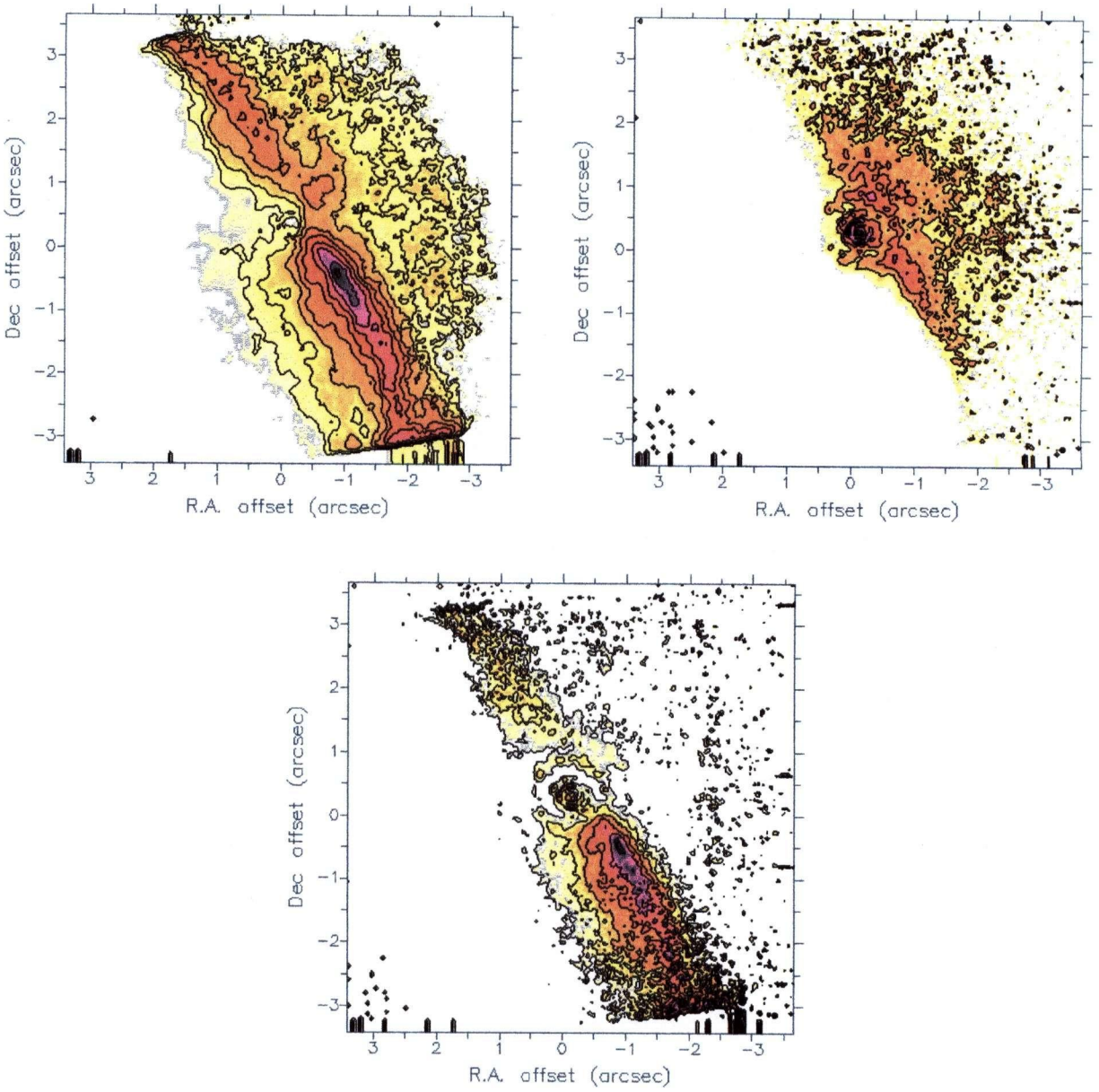

Figure 6.6: A bright AGN PSF added to NGC 2992 at H and V-bands with 6x (left), 30x (right), 100x (bottom) the peak flux in the galaxy. The color maps are then formed and displayed in a magnitude scale. The contour levels have been renormalized to the peak color in each case.

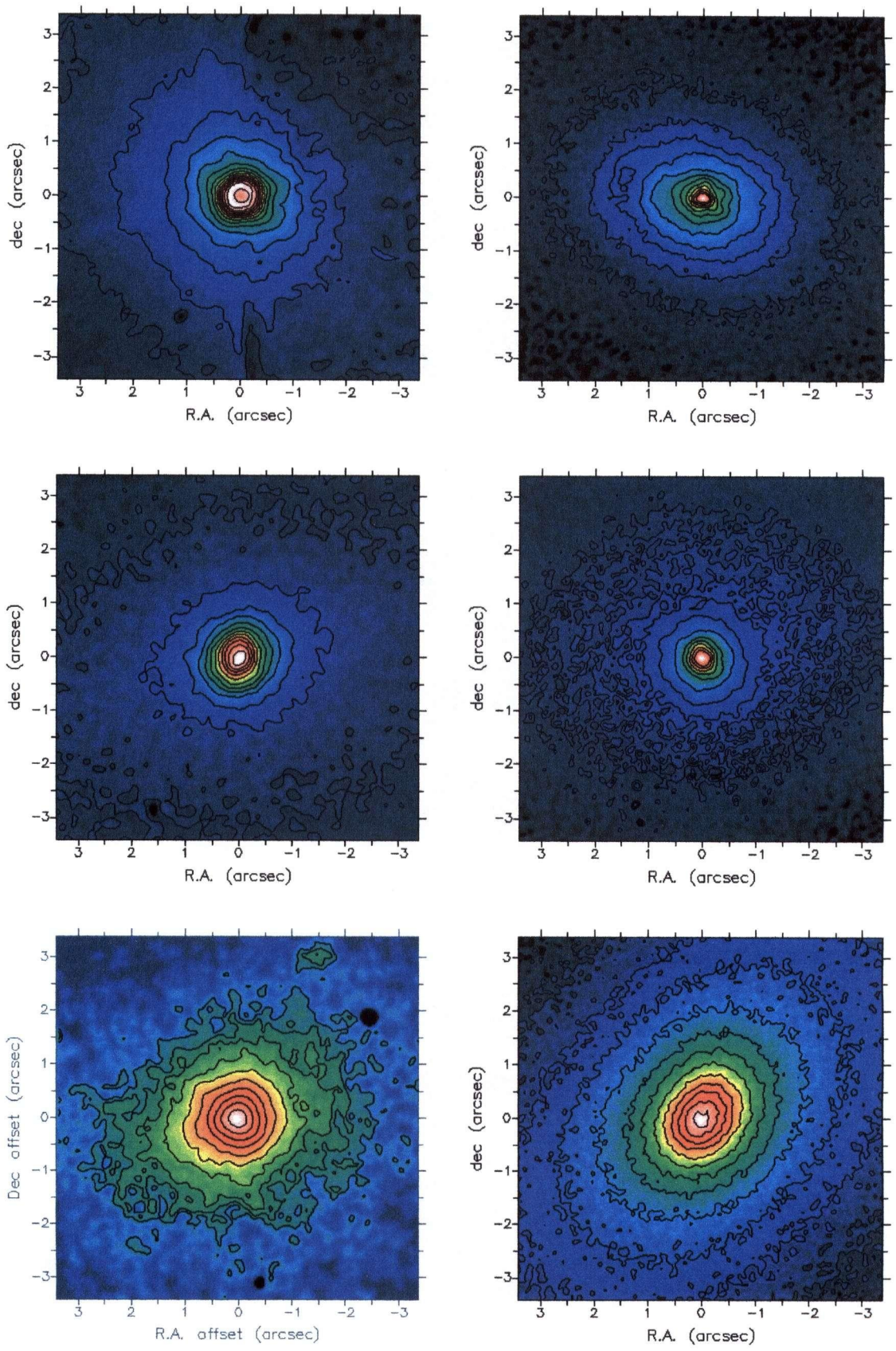
dec (arcsec)
R.A. (arcsec)
dec (arcsec)
R.A. (arcsec)
dec (arcsec)
R.A. (arcsec)
dec (arcsec)
R.A. (arcsec)
Dec offset (arcsec)
R.A. offset (arcsec)
dec (arcsec)
R.A. (arcsec)

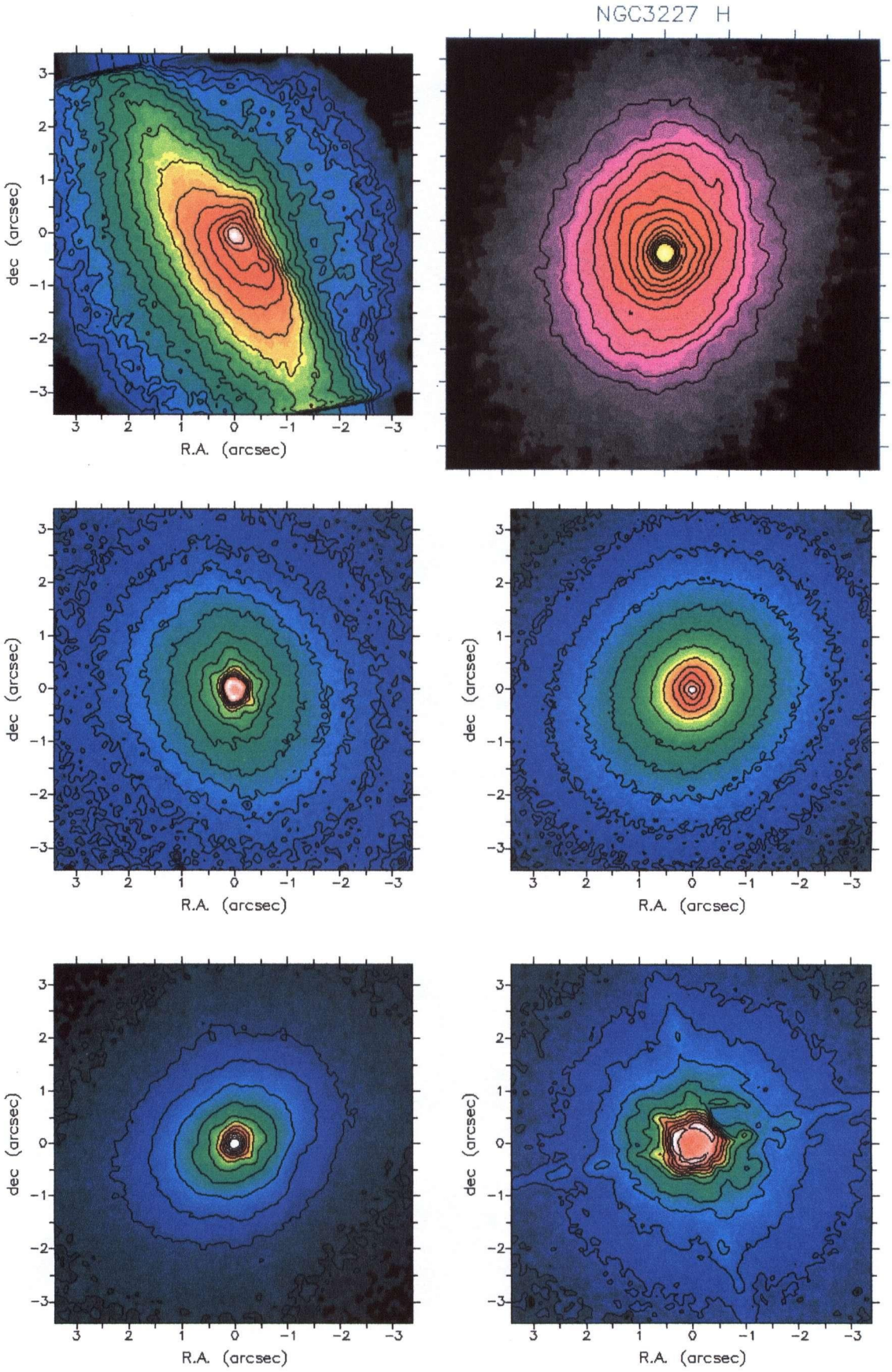
NGC3227 H
dec (arcsec)
R.A. (arcsec)
3
2
1
0
−1
−2
−3

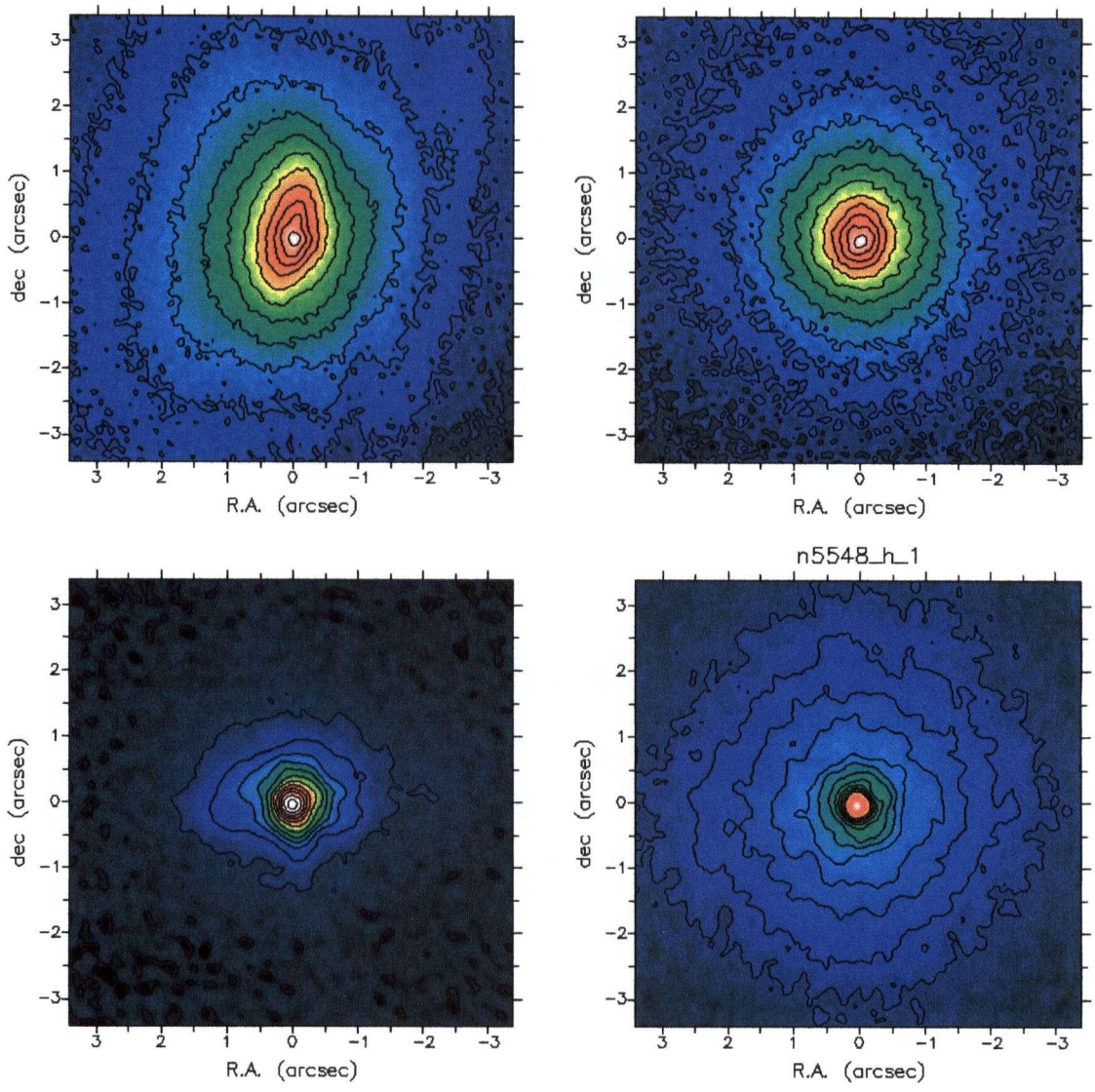

Figure 6.9: n5033h, n5273h, m1376j, n5548h

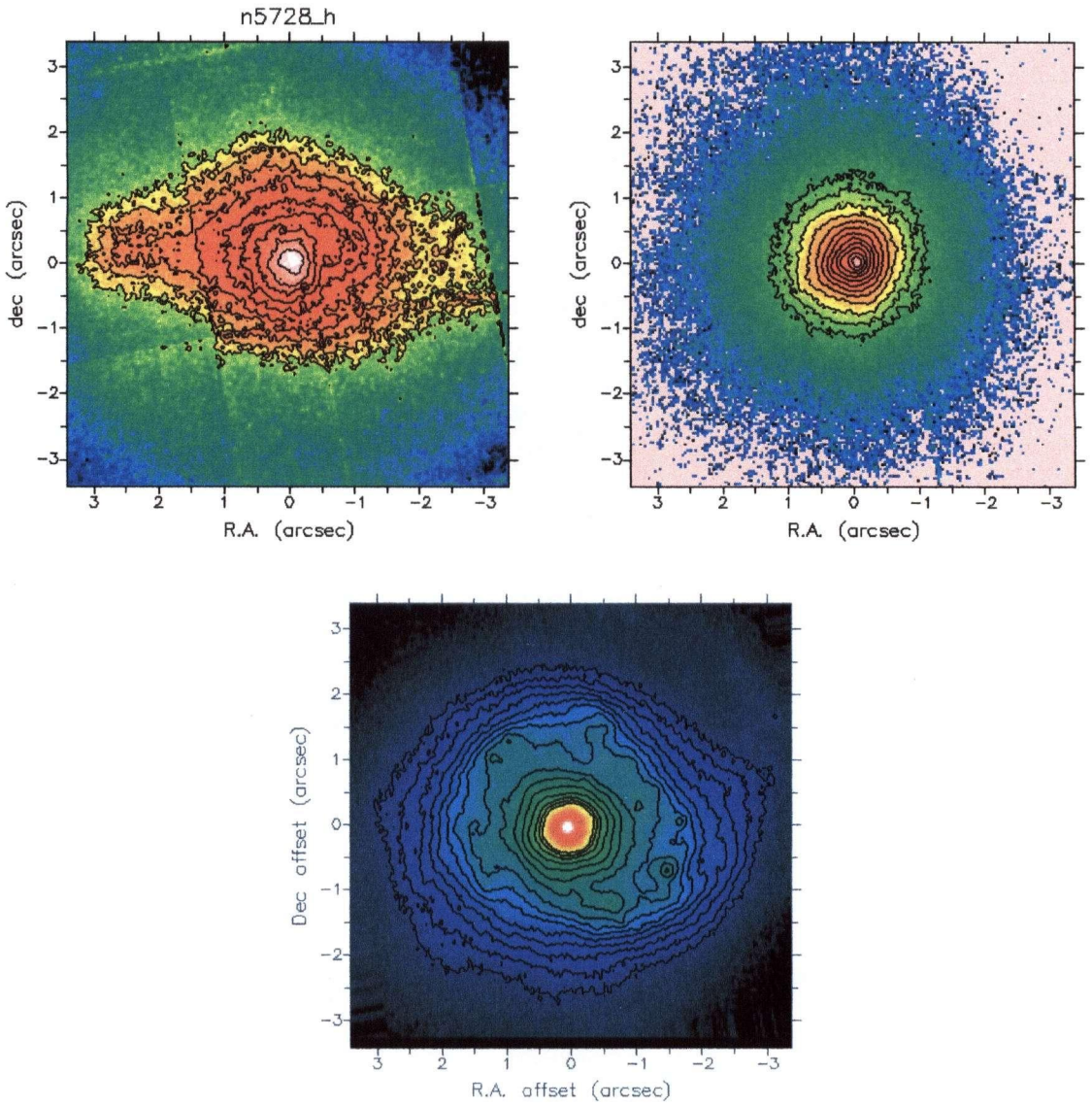

Figure 6.10: n5728h, n6814k, n7469h

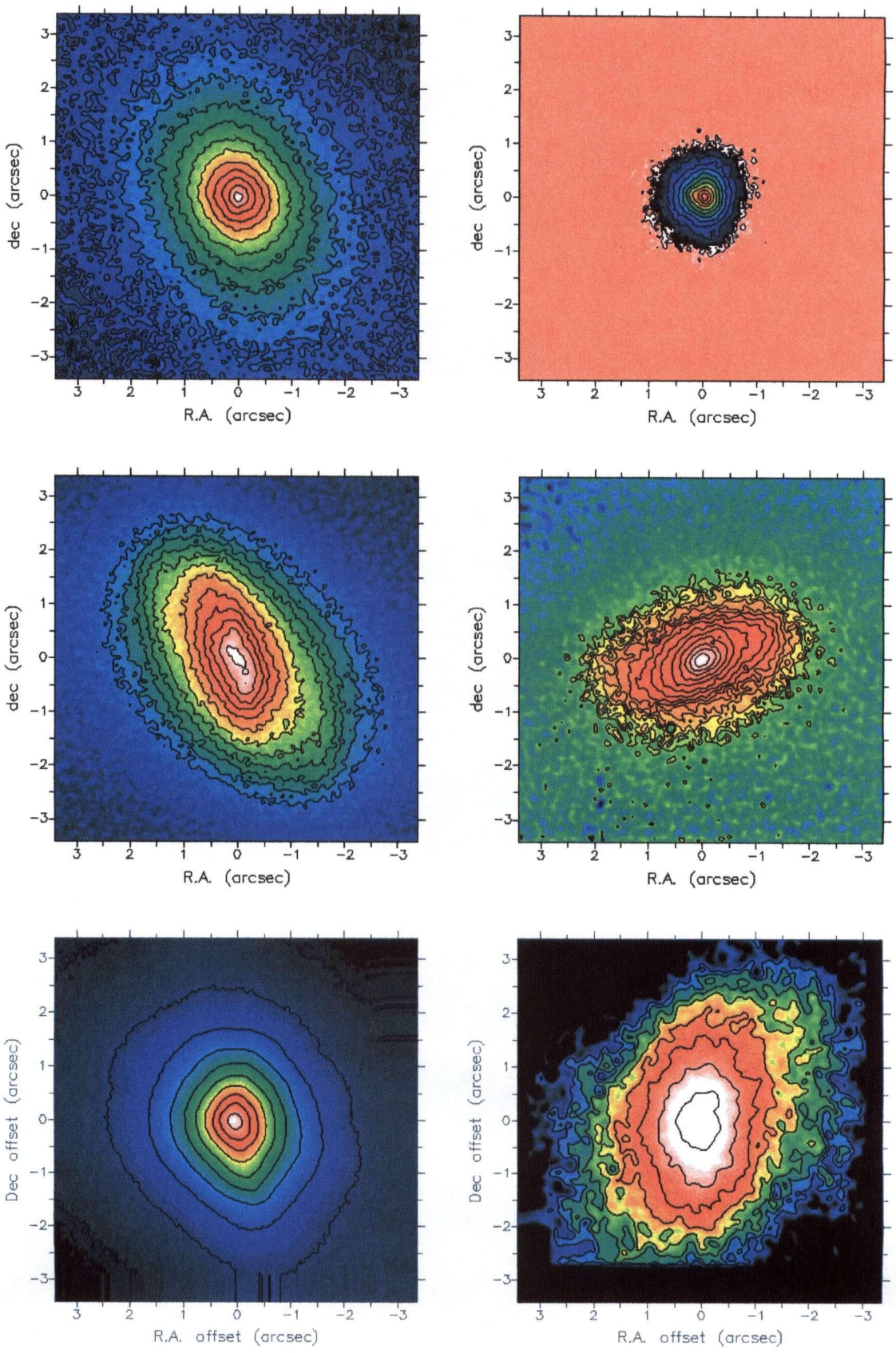
dec (arcsec)
R.A. (arcsec)
dec (arcsec)
R.A. (arcsec)
dec (arcsec)
R.A. (arcsec)
dec (arcsec)
R.A. (arcsec)
Dec offset (arcsec)
R.A. offset (arcsec)
Dec offset (arcsec)
R.A. offset (arcsec)

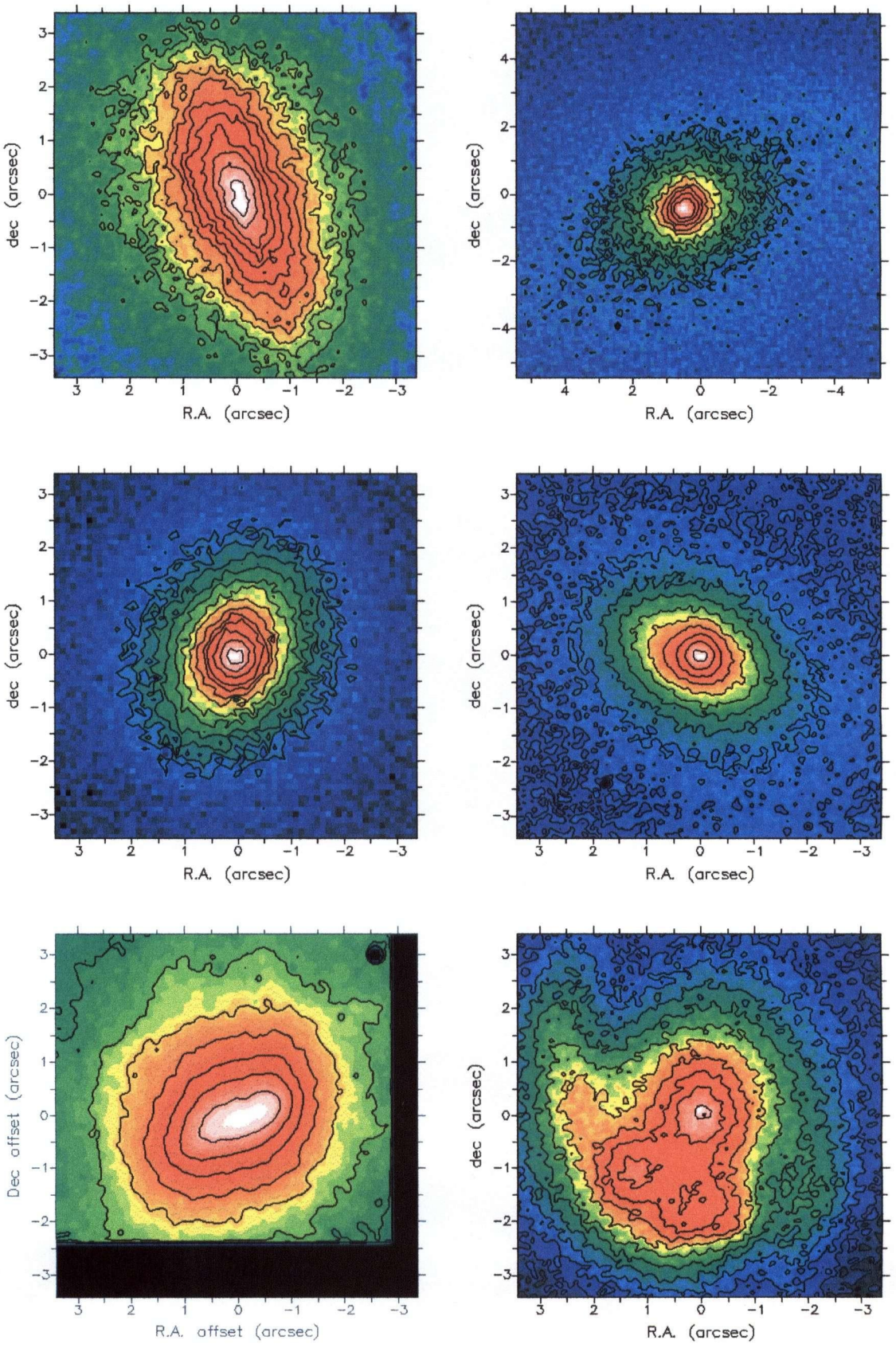
dec (arcsec)
R.A. (arcsec)
dec (arcsec)
R.A. (arcsec)
dec (arcsec)
R.A. (arcsec)
dec (arcsec)
R.A. (arcsec)
Dec offset (arcsec)
R.A. offset (arcsec)
dec (arcsec)
R.A. (arcsec)

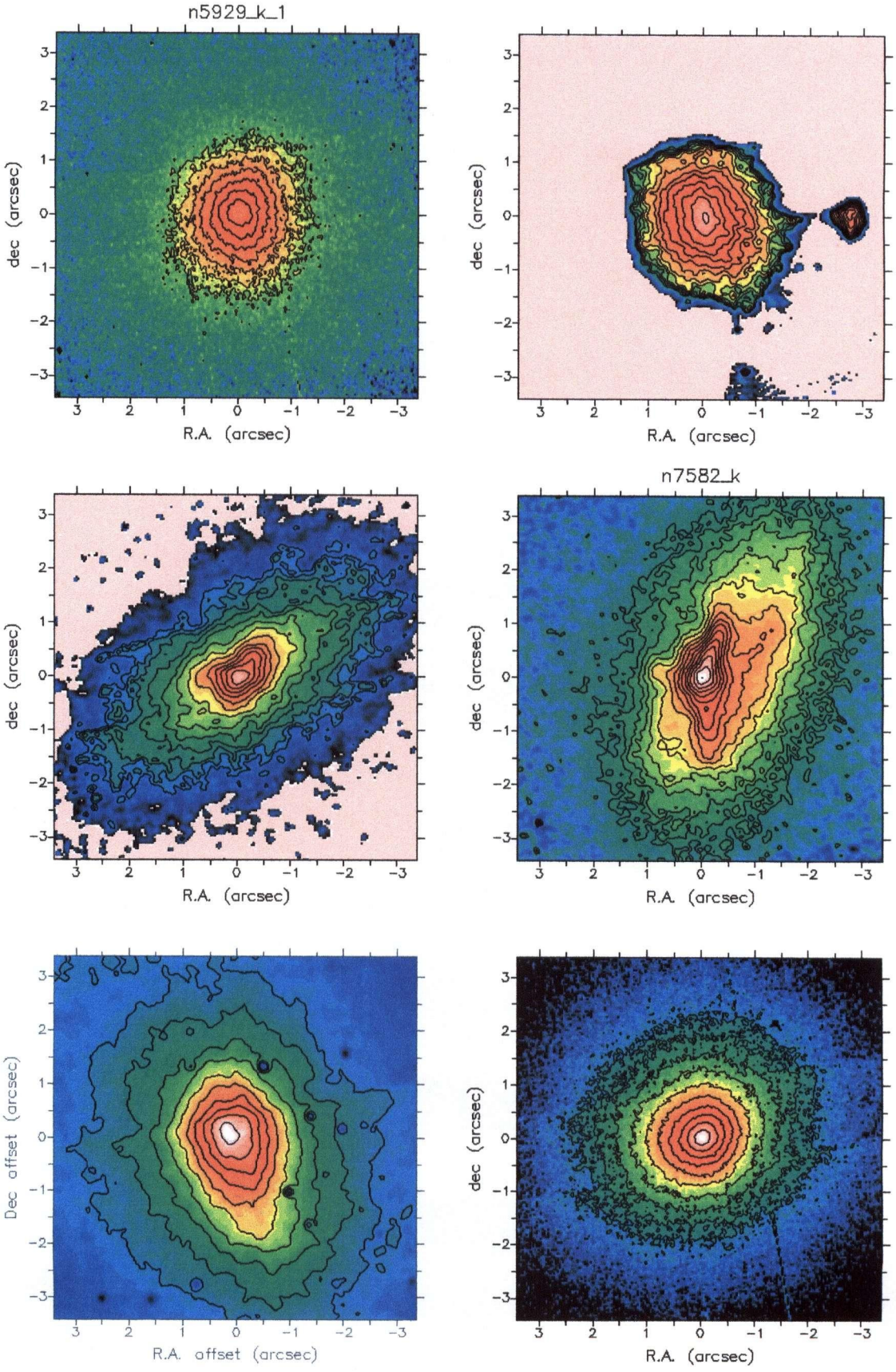
n5929_k_1
n7582_k
dec (arcsec)
R.A. (arcsec)
Dec offset (arcsec)
R.A. offset (arcsec)

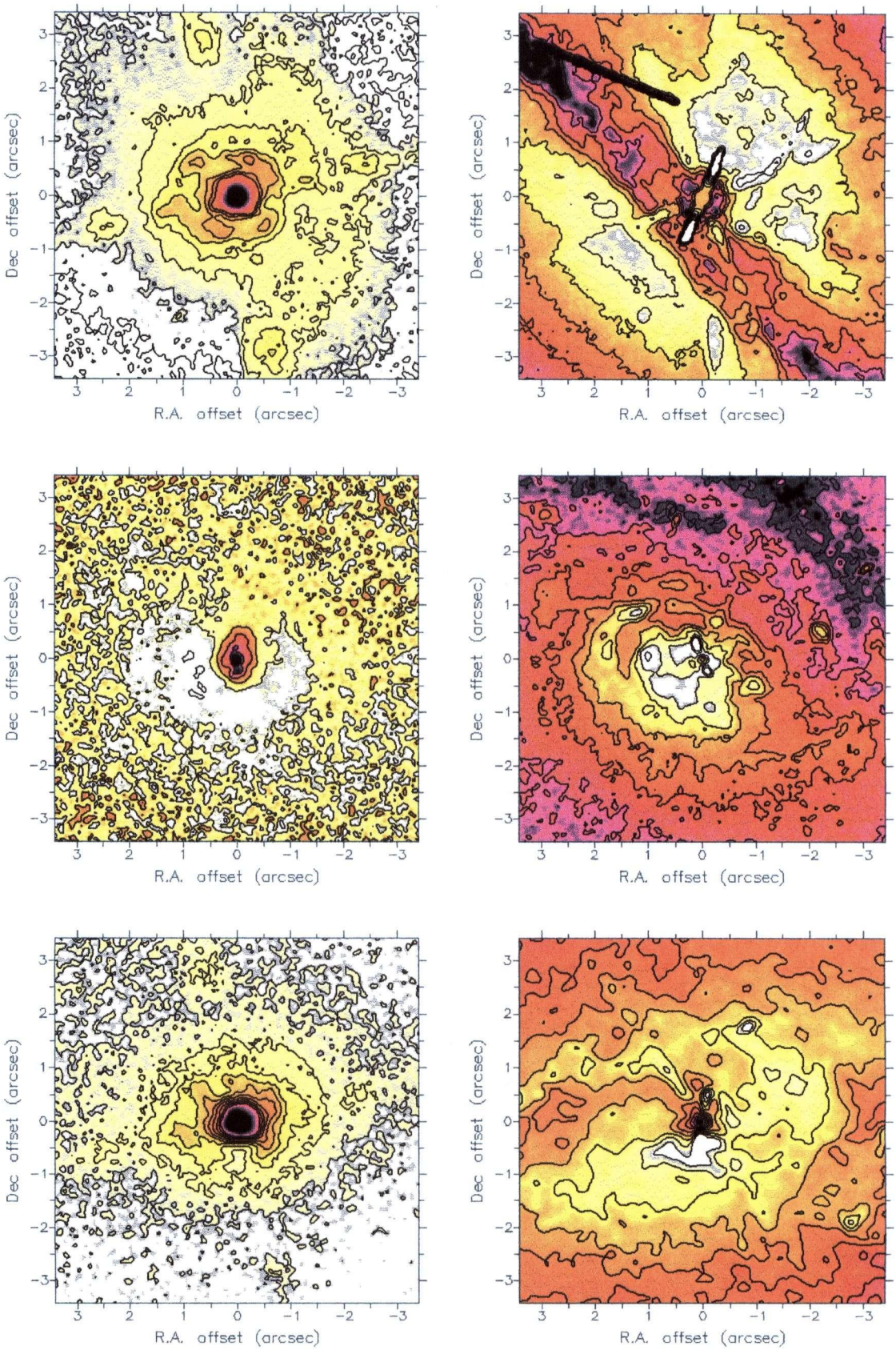
Dec offset (arcsec)
R.A. offset (arcsec)
3
2
1
0
−1
−2
−3

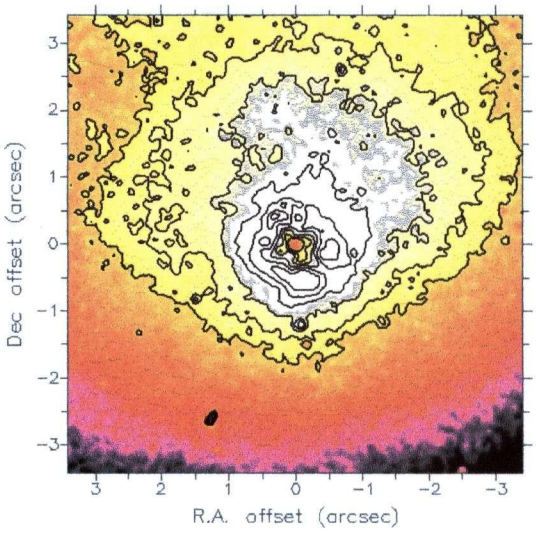

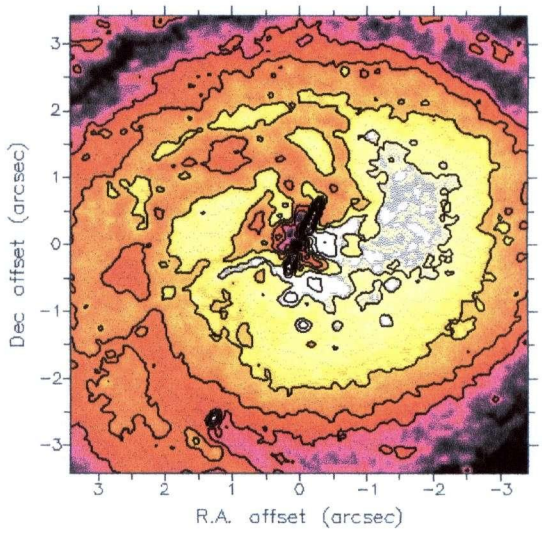

NO FILE: figs5map/dummy.eps

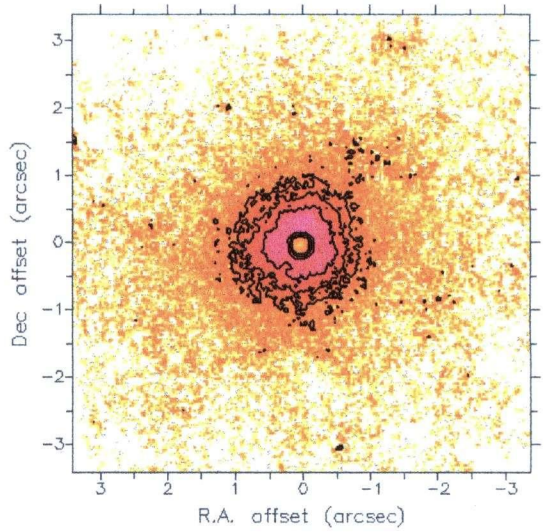

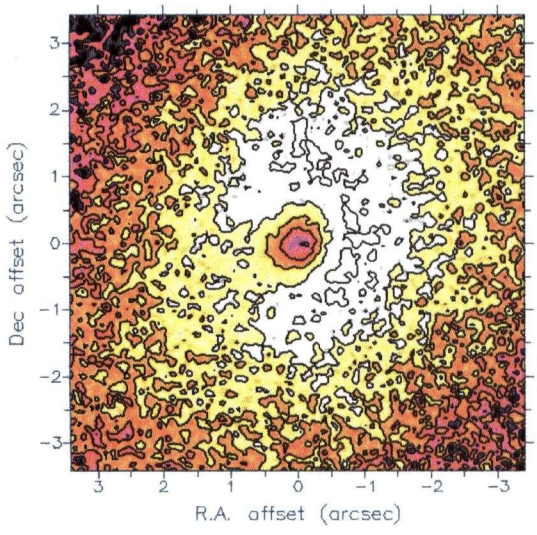

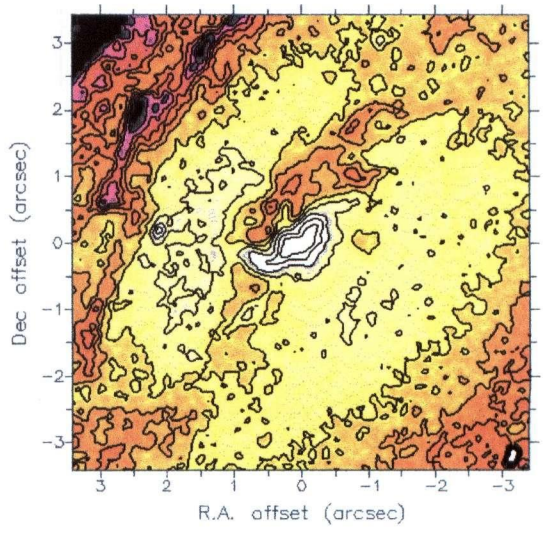

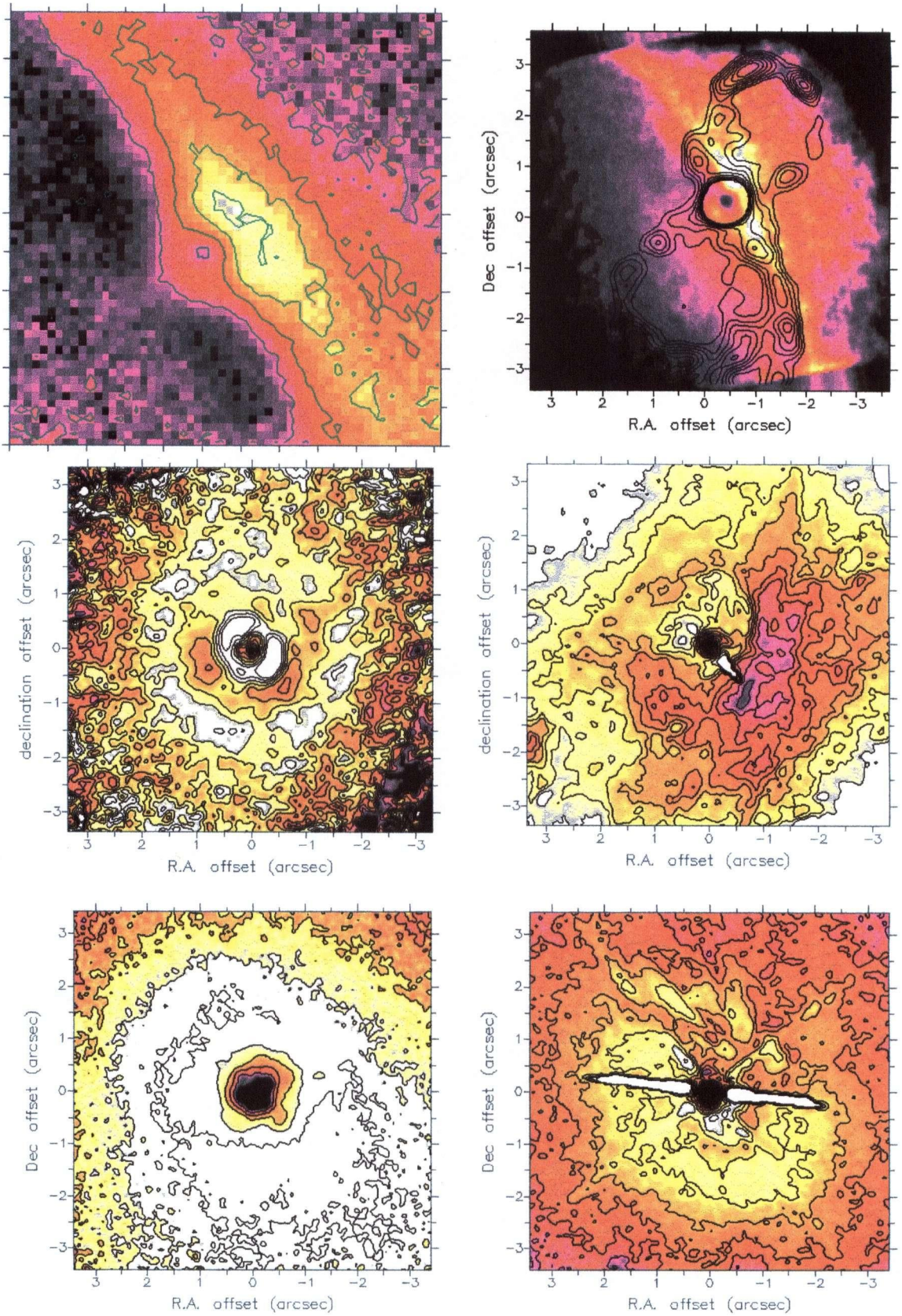
Dec offset (arcsec)
R.A. offset (arcsec)
declination offset (arcsec)
R.A. offset (arcsec)
declination offset (arcsec)
R.A. offset (arcsec)
Dec offset (arcsec)
R.A. offset (arcsec)
Dec offset (arcsec)
R.A. offset (arcsec)

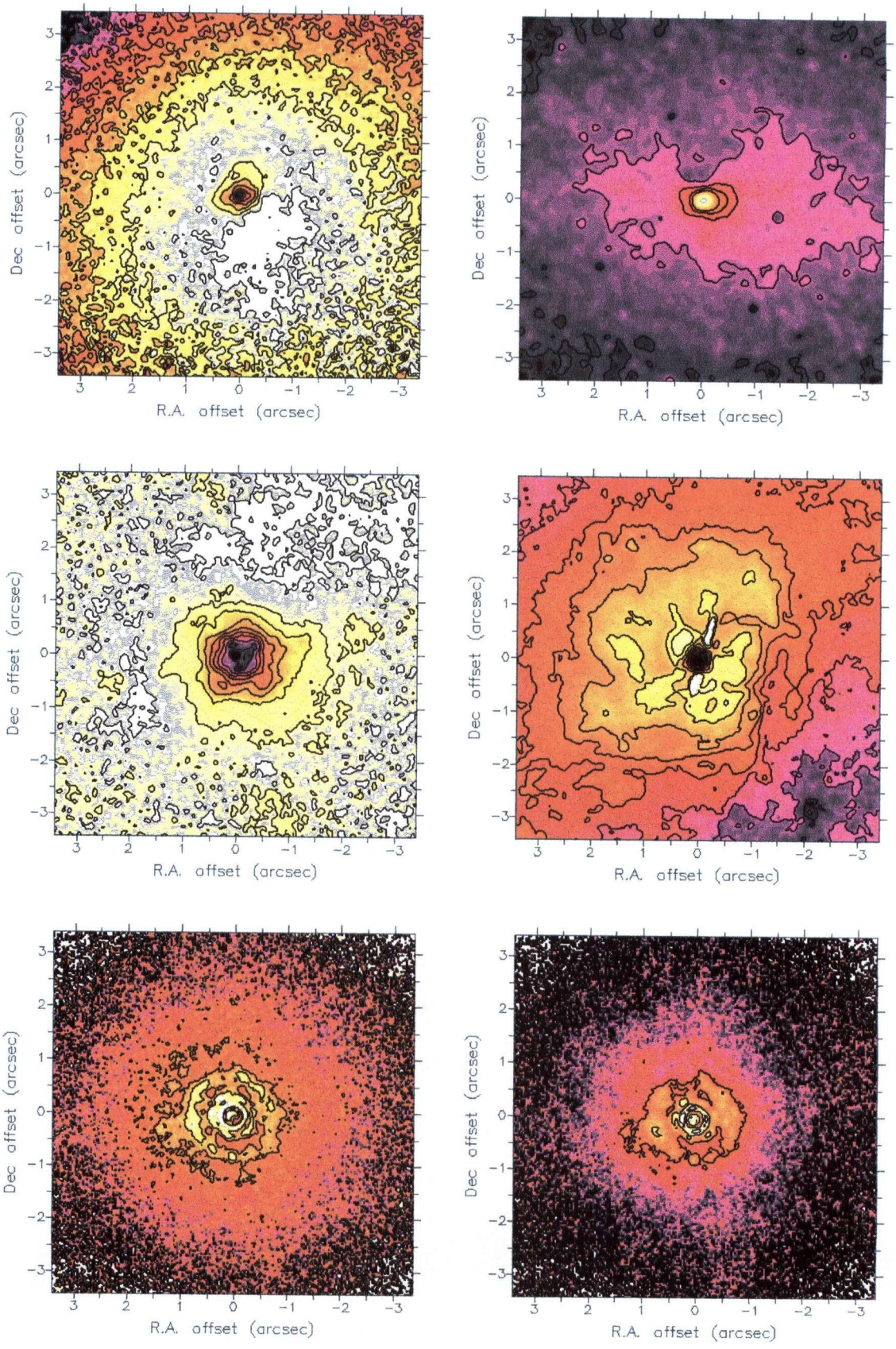
Dec offset (arcsec)
R.A. offset (arcsec)
3
2
1
0
−1
−2
−3

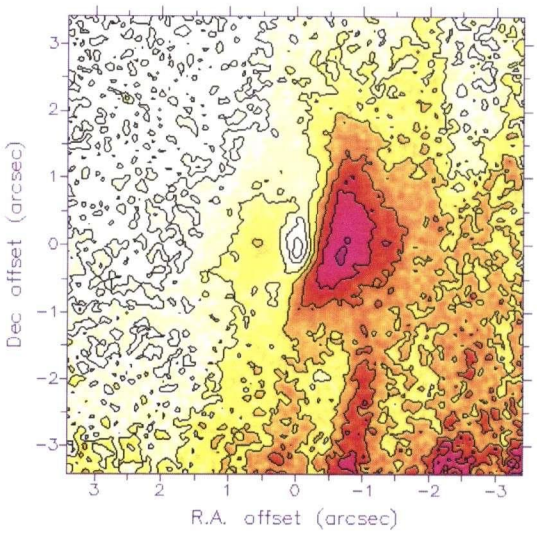

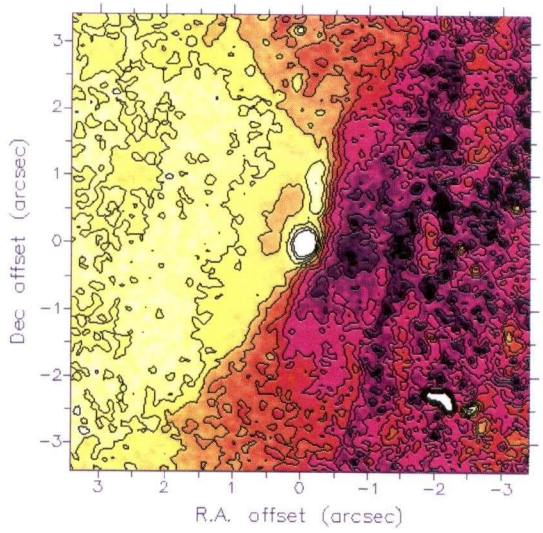

NO FILE: figs5map/dummy.eps

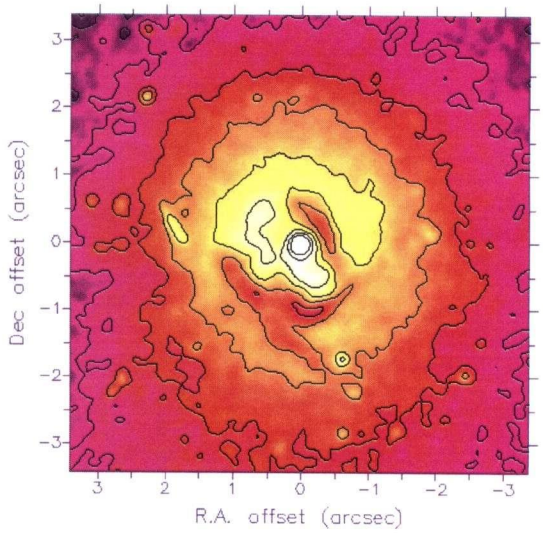

NO FILE: figs5map/dummy.eps

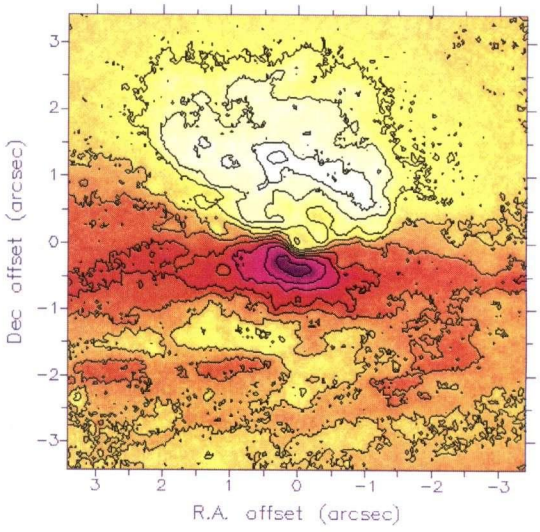

Figure 6.18: n5033bk, n5033yh, n5273yh, m1376vj

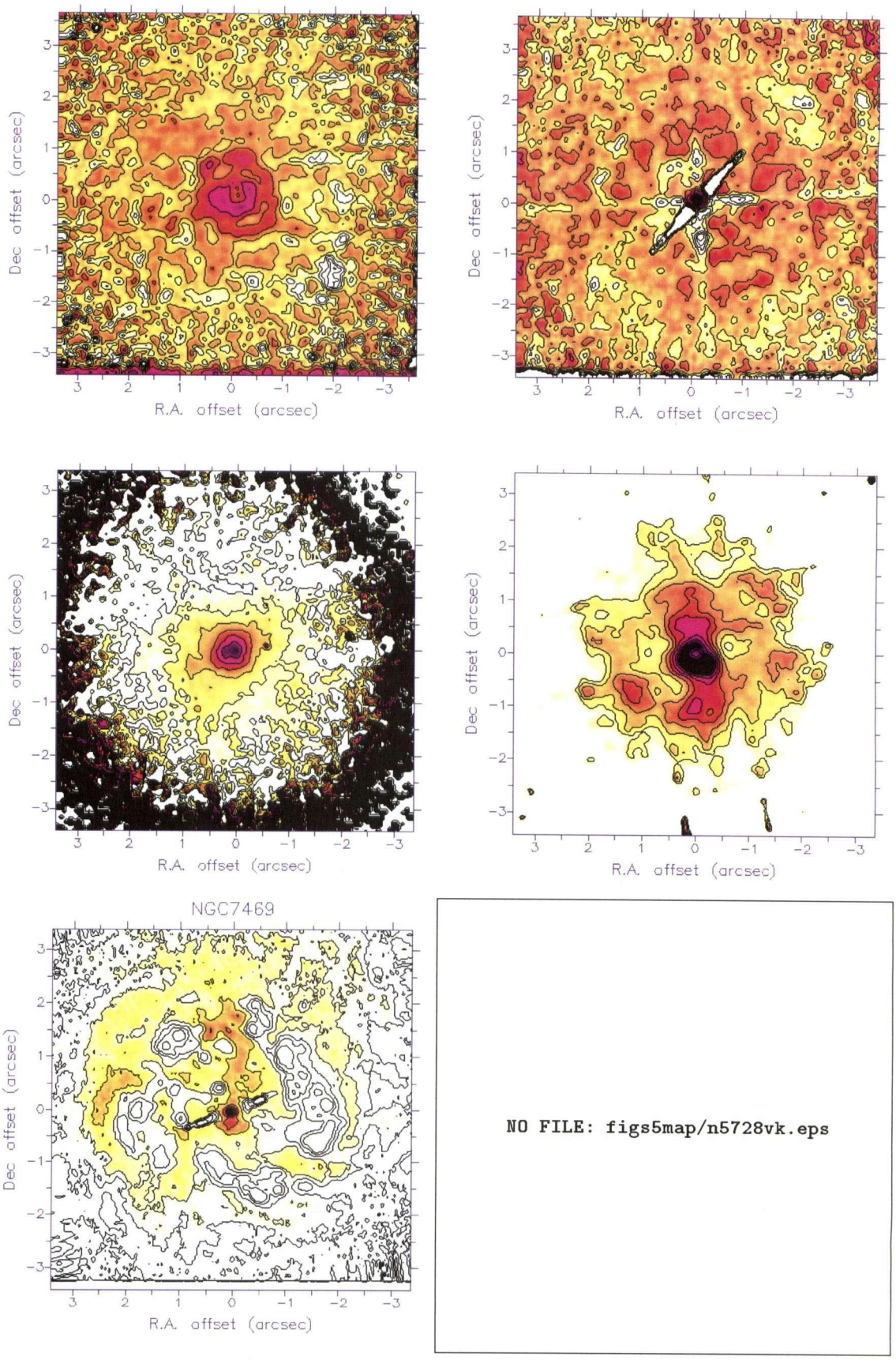

Figure 6.19: n5548hk, n5548vk, n6814hk, n6814vk, n7469vh, n5728vk

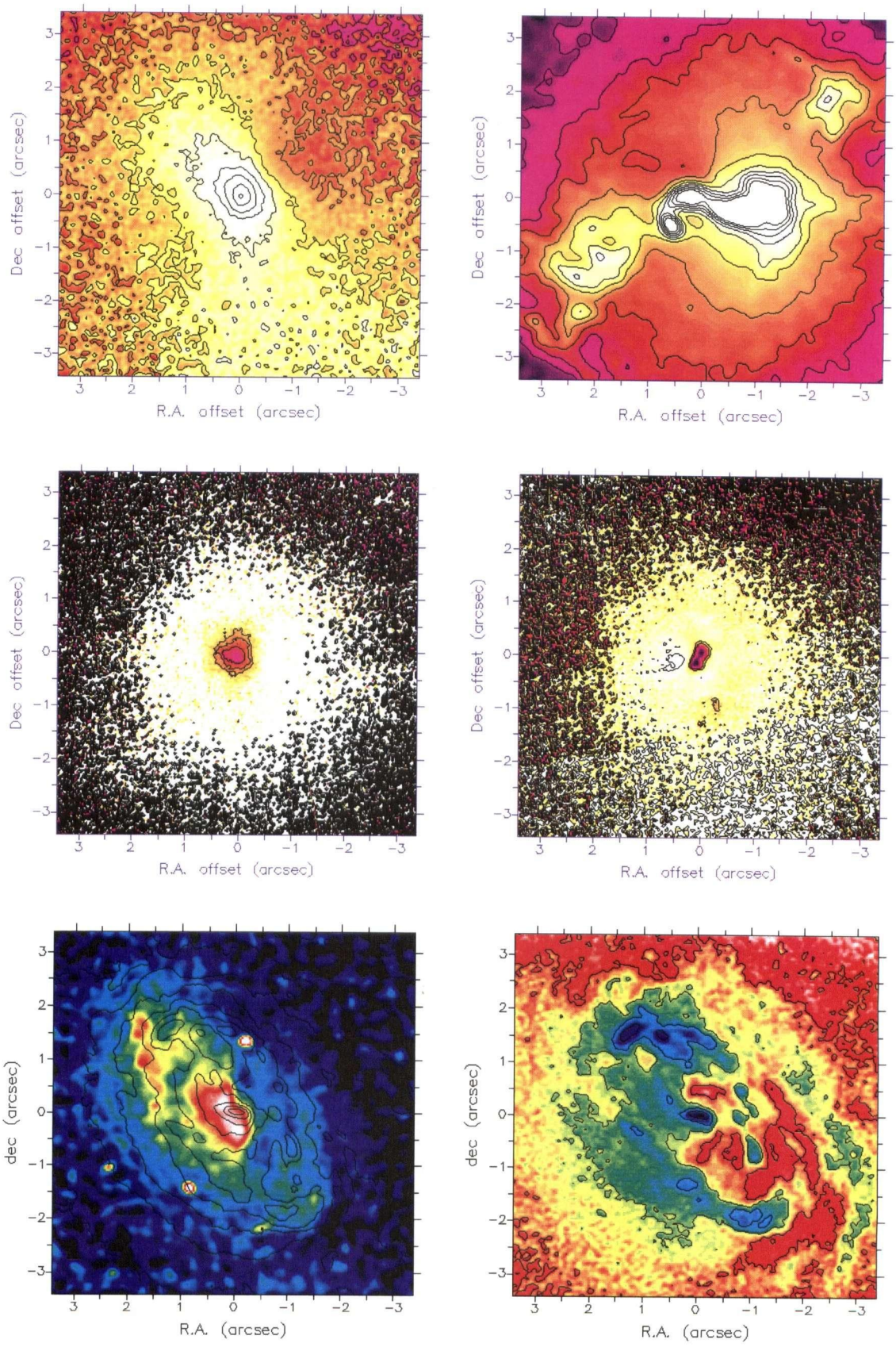

Figure 6.20: Seyfert 2 galaxy maps: m3hk, m3vh, m348hk, m348vh, m620hk, m620vh

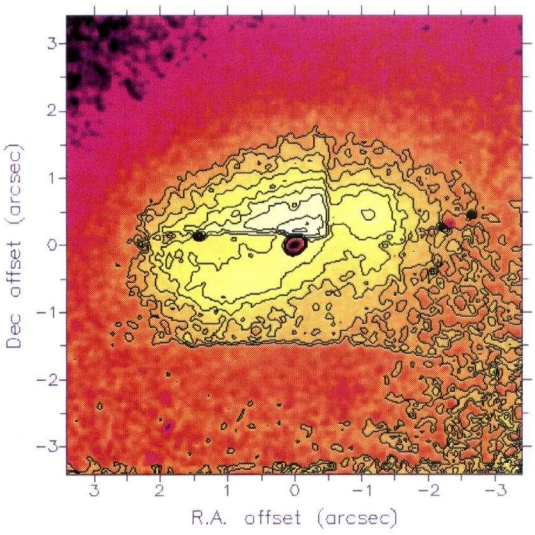

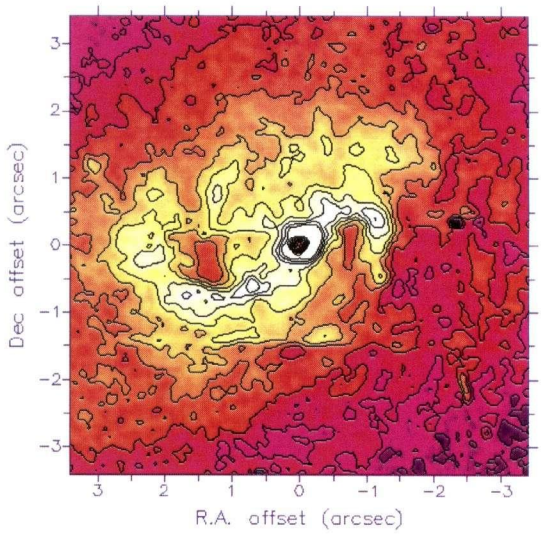

NO FILE: figs5map/dummy.eps

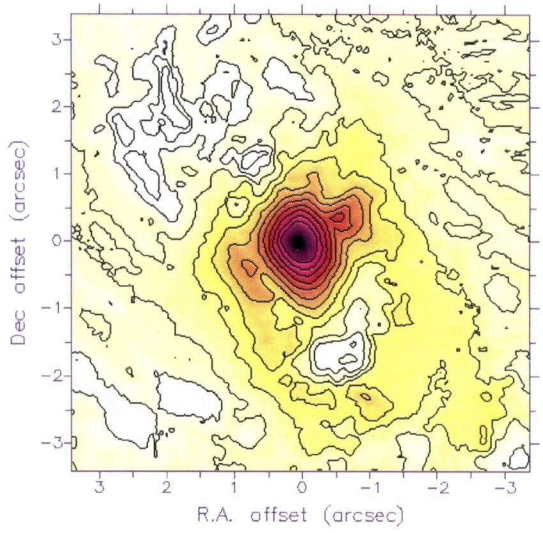

NO FILE: figs5map/dummy.eps

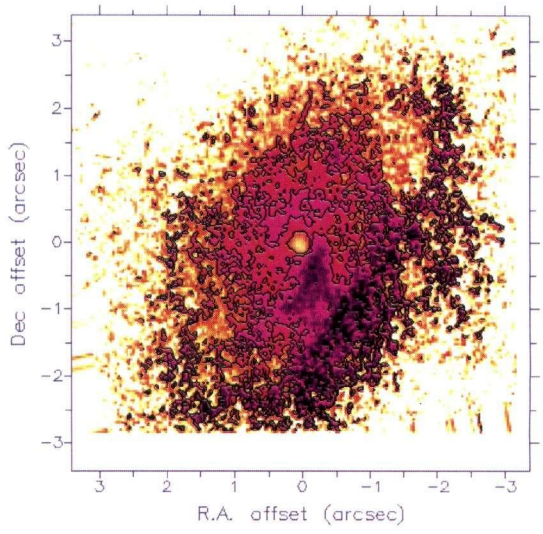

Figure 6.21: m1066hk, m1066vk, n1068vk, n1241vh

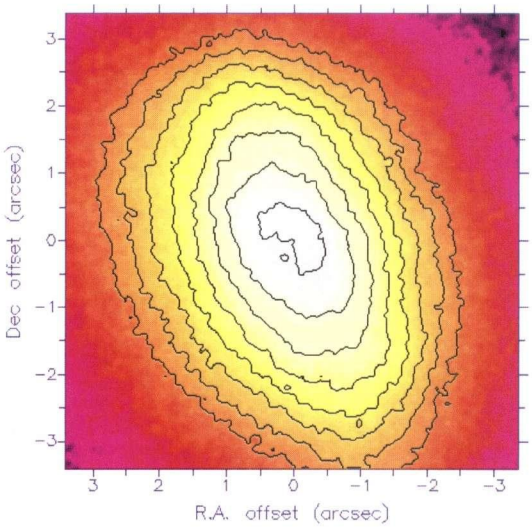

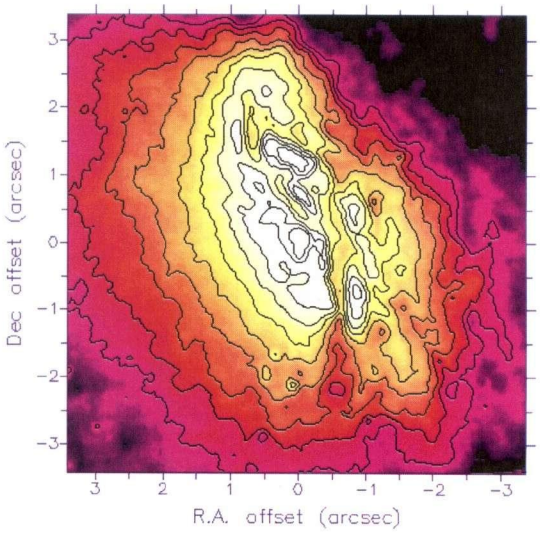

NO FILE: figs5map/dummy.eps

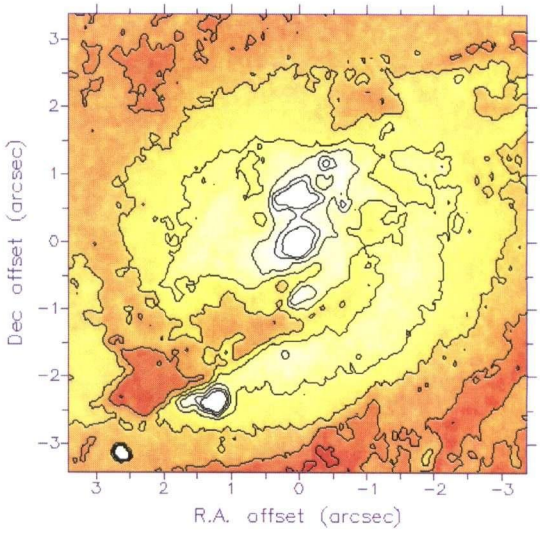

NO FILE: figs5map/dummy.eps

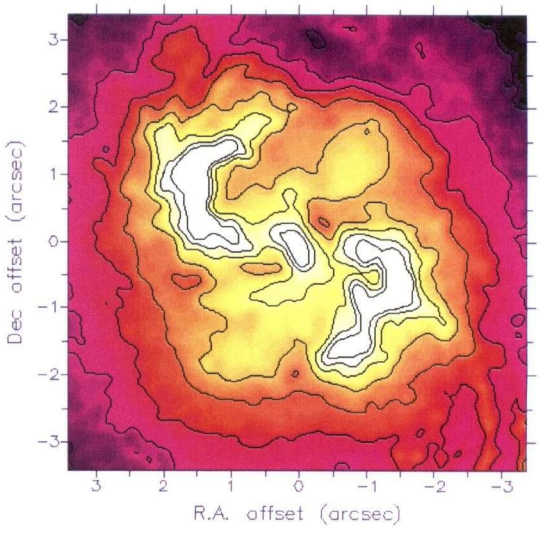

Figure 6.22: n1386hk, n1386vk, n3081vk, n3393vk

NO FILE: figs5map/dummy.eps

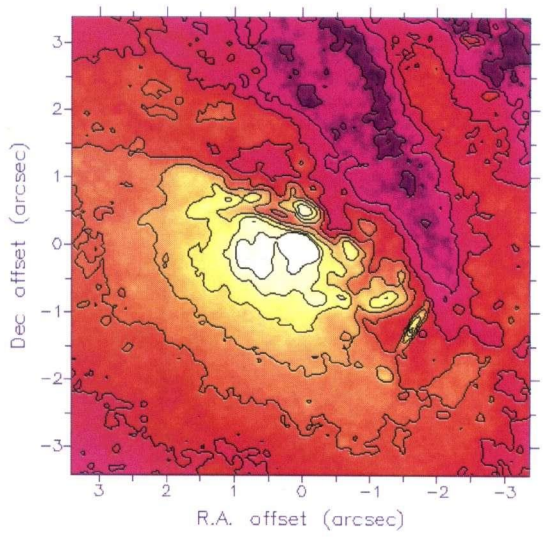

NO FILE: figs5map/dummy.eps

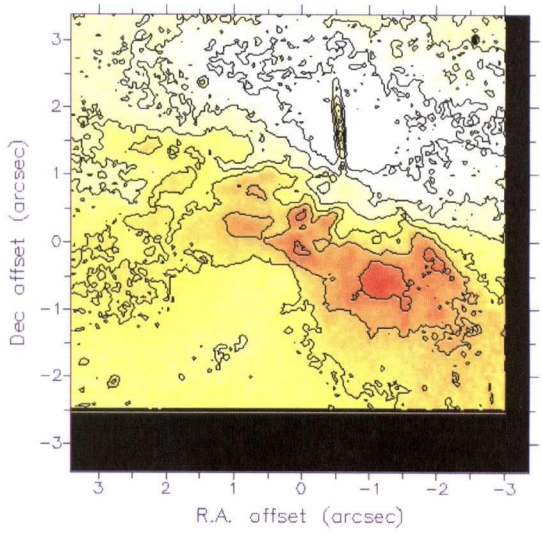

NO FILE: figs5map/dummy.eps

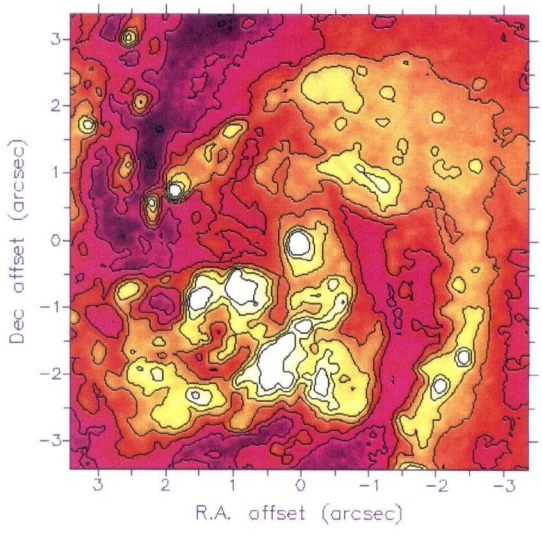

Figure 6.23: n4968vb, n5005vk, n5135vb

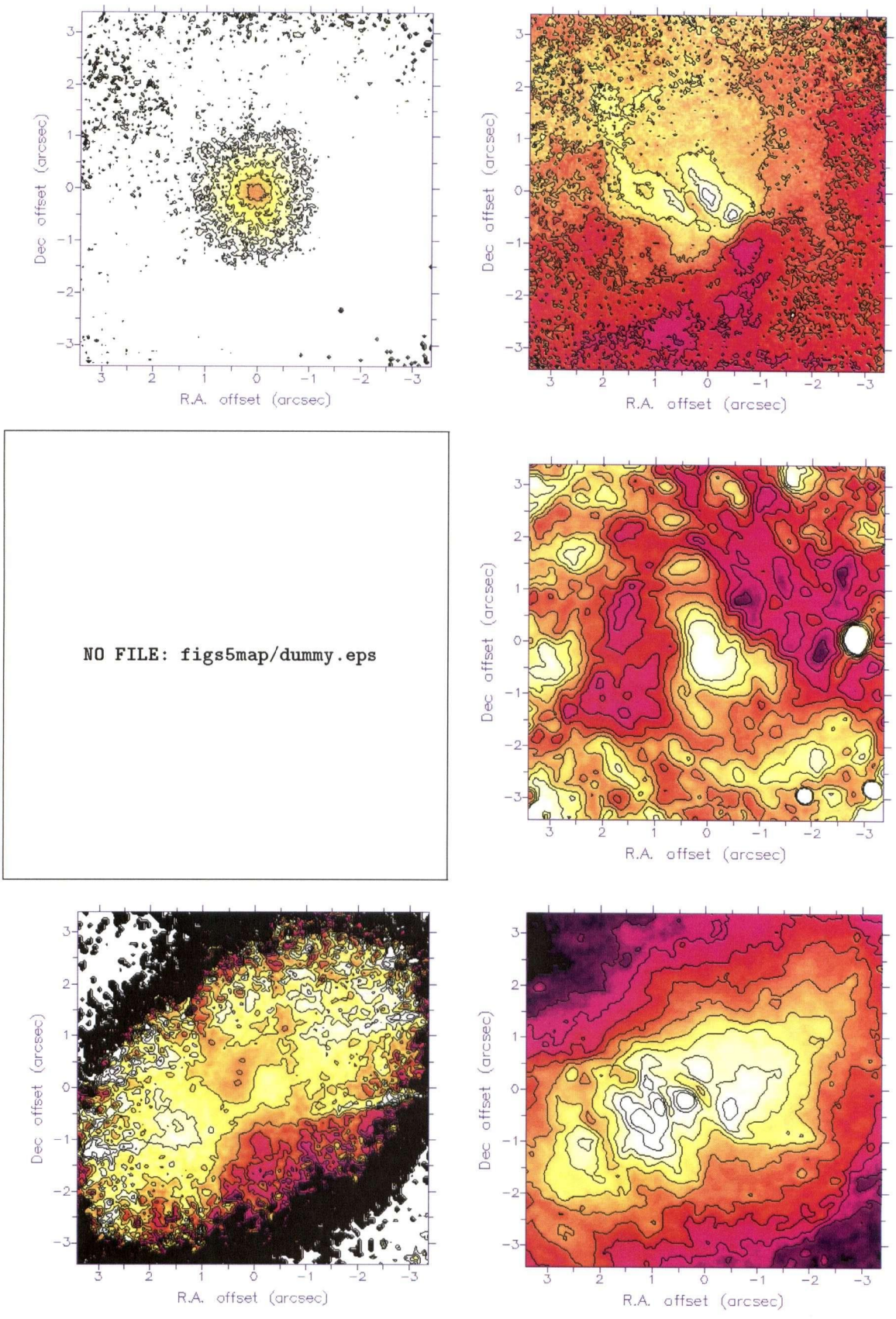

Figure 6.24: n5929hk, n5929vh, n5953vh, n7465hk, n7465vk

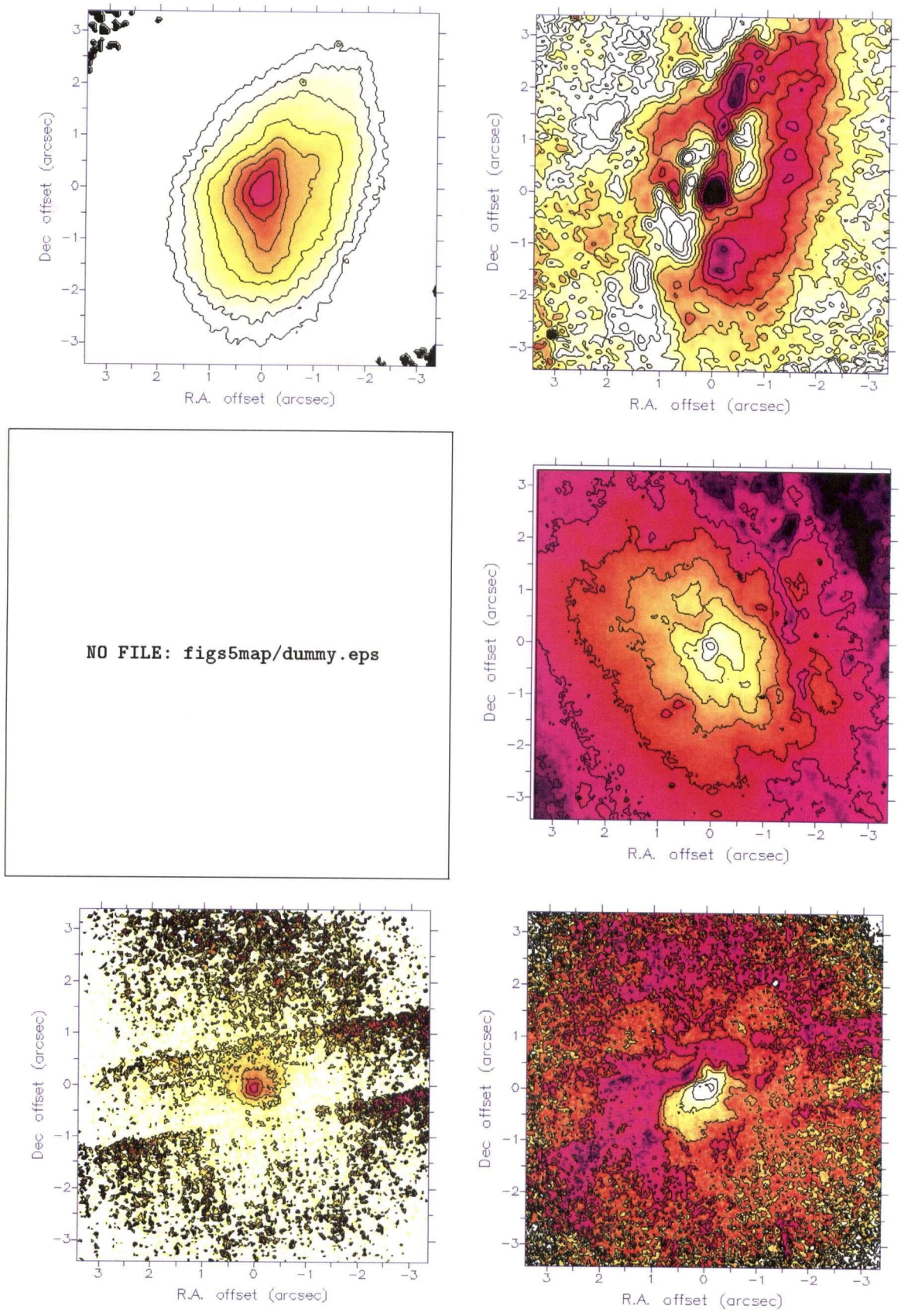

Figure 6.25: n7582hk, n7582vk, n7590vh, n7743hk, n7743vk

Chapter 7

Conclusions

Chapters 2 and 3 outlined the scope of our survey, along with the data reduction steps necessary to arrive at a scientifically useful study. Our unfortunate discovery of artifacts associated with the bright galactic nuclei temper the use of adaptive optics for certain scientific questions. The cause of these artifacts remains somewhat ambiguous, although it is plausible that the deformable mirror and control system may be reacting to the shape of the extended object (galaxy) as seen by the wavefront sensor.

In chapters 4 and 5, we studied two galaxies from our sample in detail. These were chosen as interesting objects of study based on controversial results from previous ground based and HST optical imaging. We were able to elucidate many of the physical processes involved, whilst highlighting structures and mechanisms possibly associated with the central activity. Although artifacts are a very serious problem, our results for NGC 2992 and NGC 3227 show that a detailed multi-wavelength analysis can circumvent many of these difficulties to achieve useful scientific results. For NGC2992, a spiral structure within the central 6″ and a 1″ extended feature are traced down to the core at the resolution of our images. We speculate based on these observed structures that multiple radio components are superposed which contribute to the observed figure-8 morphology in the VLA images: one associated with the spiral structure in the galaxy disk, and another flowing out of the galaxy plane. With NGC3227, an assembly of star formation knots lying in a spiral/ring pattern , is suggestive of embedded spiral arms within the larger-scale spiral of the outer galaxy. At an elongation of PA $\sim 40°$, there may be a nuclear disk or bar structure, although the blue colours are suggestive of some scattered nuclear continuum emission. The extended radio feature observed with MERLIN is coincident with the near-IR region of knots which assume a spiral/ring pattern, but may still be associated with an outflow.

In chapter 6, we used near-IR colour maps to probe the extinction due to dust in the circum-nuclear regions of all the galaxies in our sample. This type of inquiry circumvents much of the artifact contamination by searching for structures extending beyond the central arcsec. In the absence of any standardized classification for dust absorption in galaxies, we have developed a graded system of two indices. A dust patchiness index (DPI) characterizes the dust morphology, and a global dust index

(GDI) combines the DPI morphological index with a quantitative assessment of the extinction.

It was clear that we were finding a lot of patchy dust in the vicinity of the active nucleus (between ten and a few hundred parsecs typically) with the implication that there might be substantial dust along the line of sight to the nucleus itself. We also found a clear trend for dustier core regions in the Sy2, Sy1.8 and Sy1.9 than in the Sy1 with the easily detectable Broad Line Regions (BLRs). Although this may not provide a ubiquitous picture of being able to turn any Seyfert 1 into a Seyfert 2 using GDM, it does point to the possibility that enough patchy dust could exist to accomplish this task in many cases. The observational evidence is now such that an alternative should be considered to the standard classification paradigm where the visibility of the type 1 AGN signature is the main differentiator. The new possibility is that Seyfert galaxies are drawn from two different populations: very dusty, and less/non-dusty. Sy2 are then thought to almost always be of the very dusty type. Whether or not the actual Sy1 nucleus is visible in the very dusty type is then merely a result of the current dust configuration of any given Seyfert nucleus. Mid-IR studies at a similar resolution would be necessary to verify whether the very high column densities do indeed exist in some cases over patchy dust regions covering the nucleus.

Chapter 8

Glossary

AOB - adaptive optics bonnette

AGN - active galactic nucleus

ATM - accreting torus model

BLR - broad line region

CCD - Charge Coupled Device: an electronic detector which transfers photogenerated charge along rows of the array using multi-tiered potentials

CfA - Harvard Center for Astrophysics

CFHT - Canada-France-Hawaii Telescope

DSS - Palomar Digital Sky Survey: see page 75

FWHM - Full Width at Half Maximum

GDM - galactic dust model

HST - Hubble Space Telescope

ILR - Inner Linblad Resonance: see page 77

IR - infra-red

IRAS - Infra-Red Astronomical Satellite

J,H,K-bands - broad band filters covering the main atmospheric windows from 1 to 2.5 microns (see table 2.1)

Jy - Jansky: $10^{-26} W m^{-2} Hz^{-1}$

KIR - Kilopixel InfrarRed camera

LOS - line of sight

MONICA - Montreal Infrared Camera

MTF - Modulation Transfer Function

NGC - New Galactic Catalog

NGST - Next Generation Space Telescope

NLR - narrow line region

PSF - Point Spread Function

pc - parsec: 3.0857×10^{18} cm.

RSA - Revised Shapley-Ames catalog of galaxies

SED - Spectral Energy Distribution

SNe - supernovae

Sy - Seyfert galaxy

SSy1 - (Saturated) nuclear point source is evident, saturated in HST image, WFS counts > 50 on AOB.

USy1 - (Unsaturated) nuclear point source is evident, unsaturated in HST image, WFS counts < 50 on AOB.

RSy1 - (Resolved) identified as Sy 1 but showing no discernible point source

Sy1 - Objects showing broad Hβ emission line and with [OIII]/H$\beta < 0.3$

Sy1.2 - broad Hβ and with [OIII]/H$\beta < 1$

Sy1.5 - broad Hβ and with $1 <$ [OIII]/H$\beta < 4$

Sy1.8 - broad Hβ and with [OIII]/H$\beta > 4$ Hβ with decreasing ratios of [OIII]/Hβ

Sy1.9 - detectable broad line component only in the Hα line

Sy2 - [OIII]λ5007 to Hβ ratio > 3, and [NII]λ6584 comparable to Hα

UKIRT - United Kingdom Infra-Red Telescope

VLA - Very Large Array: a radio interferometer in New Mexico, USA.

WFPC - Wide-field and Planetary Camera

WFS - wavefront sensor

References

[1] Allen M., Dopita M., Tsvetanov Z., Sutherland R., 1998, astroph/9809123

[2] Alloin D., Rouan, D., Rigaut, F., Lai O., Doyon R., Crampton D., Gendron E., Arsenault R., 1998, proceedings of ESO/OSA: *Astronomy with Adaptive Optics*, Sonthofen, Germany.

[3] Alonso-Herrero A., Simpson C., Ward M. J., Wilson A. S., 1998, ApJ, 495, 196

[4] Alonso-Herrero A., M. Rieke & G. Rieke 1998 ApJ, 494, 138

[5] Andrew H.C. and Hunt B.R., 1977, *Digital image restoration*, Prentice-Hall, Englewood Cliffs, N.J., USA.

[6] Antonucci R. 1982, Nature 299, 605

[7] Antonucci R. R. J. 1993, ARAA, 31, 473

[8] Arribas S., Mediavilla E. 1994, ApJS, 437, 149

[9] Athanassoula E., 1992, MNRAS, 259, 345

[10] Awaki H., Koyama, K., Inoue H., Halpern J., 1991, PASJ, 43, 195.

[11] Bassani L., Dadina M., Maiolino R., Salvati G., Risalti G., Della Ceca R., Matt G., Zamorani G., 1998, A&A In Press, astro-ph/9811074

[12] Beuzit J-L., Demailly L, Gendron E., Gigan P., plus 11 authors, 1997, Experimental Astronomy, 7, 285.

[13] Binney J., Tremaine S., "Galactic Dynamics", Princeton University Press, Princeton, New Jersey, USA, 1987

[14] Bonnato C., Pastoriza M., 1988, ApJ, 486, 132.

[15] Cameron A.G.W. 1985, ApJL, 299, L83

[16] Carollo C.M. & Stiaveli M., 1998a, AJ, 116, 68.

[17] Carollo C.M. & Stiaveli M., 1998b, AJ, 115, 2306.

[18] Carleton, N.P., Elvis, M., Fabbiano, G., Willner, S.P., Lawrence, A., Ward, M. 1987, ApJ, 318, 595

[19] Casali & Hawarden T., UKIRT Faint Star catalog, UKIRT newsletter, vol11, 25, 1990

[20] Chapman S.C., Morris S.L., Walker G.A.H.W. 1998, Proceedings of ESO/OSA: *Astronomy with Adaptive Optics*, Sonthofen, Germany.

[21] Chapman S.C., Morris S.L., Alonso-Herrero A., Falcke H., 1999, submitted to MNRAS.

[22] Chapman S.C., Scott D., Lewis G., Borys C., Fahlman G., 1999, A&A Submitted, astroph/9810250.

[23] Clark C., Chapman S.C., McKenna D., Hunter C., Massey S., 1993, SPIE vol2219, 353.

[24] Close L., Roddier F., Roddier C., Graves J., Northcott M., Potter D., 1998, SPIE, 3353, 406

[25] Colbert E., Baum S., Odea C., Veilleux S., 1998, ApJ, 496, 786

[26] Colbert E., Baum S., Gallimore J., Odea C., Lehnert M., Tsvetanov Z., Mulchaey J., Caganoff S., 1996, ApJS, 105, 75

[27] Corwin H., Buta R., DeVaucouleurs G., 1994 AJ, 108, 2128.

[28] Dahari O. & DeRobertis M., 1988, ApJS, 67, 249

[29] Davidge T., Courteau S., 1999, ApJ, in Press.

[30] Doyon R., Joseph R., Wright G., 1994, ApJ, 421, 101.

[31] Edelson, R.A., & Malkan, M.A. 1986, ApJ, 308, 59

[32] Edelson, R.A., Malkan, M.A., and Rieke G., 1987, ApJ, 321, 233

[33] Falcke, H., Wilson A., Simpson C., 1998, AJ, 95, 1689

[34] Friedli, D., Wozniak, H., Rieke, M., Martinet, L. & Bratschi, P. 1996, AA Supl, 118, 461

[35] Friedli, D., Benz, W., 1993 A&A, 268, 65

[36] Gallimore J.F., Baum, S.A., O'Dea C.P., 1997, Nat 388, 852

[37] Ghez A.M., Klein B.L., Morris M., Becklin E., 1998, ApJ, 509, 678

[38] Glass I. and Moorwood M., 1985, 214, 429.

[39] Gonzalez-Delgado R.M., Perez E. 1997, MNRAS, 284, 931

[40] Gonzalez-Delgado R.M., Perez E. 1998, ApJ, 505, 174

[41] Goodrich, R.W. 1990, ApJ, 355, 88

[42] Goodrich, R.W. 1995, ApJ, 440, 141

[43] Haehnelt M., Rees M., 1993, MNRAS, 263, 168

[44] Heckman T. M. 1980, AA , 87, 142

[45] Heckman T. M., Armus L., Miley G. K. 1990, ApJS, 74, 833,

[46] Heyvaerts J., Pudritz R.F. and Norman C., 1987, In *The Galactic Center. Proceedings of a symposium in Honor of C.H.Townes* , edited by D.C. Backer (AIP, New York).

[47] Ho L., 1999, ApJ, 510, 631

[48] Ho L., Filippenko A., Sargent W., 1997a, ApJ, 487, 591

[49] Hurt R.L. 1994, PASP, 106, 549

[50] Hutchings J., Crenshaw D., Kaiser M., Kraemer S., plus 10 authors, 1998, ApJ, 492, 115

[51] Hutchings J., Morris S.L., Crampton D., Steinbring E., 1998, PASP, 110, 374

[52] Ivison R., Smail, I., Le Borgne J-F., Blain A., Kneib J-P., Kerr T., Bezecourt J., Davie J., 1998, MNRAS, 298, 583

[53] Jaffe W., Ford H., Ferrarese L., Vandenbosch F., OConnell R. 1993, Nature, 364, 213

[54] Jaffe W., Ford H., Ferrarese L., Vandenbosch F., OConnell R.,, 1996, ApJ, 460, 214

[55] Knapen J., Laine S., Yates J., Robinson A., Richards A., Doyon R., Nadeau D., 1997, ApJ, 490L, 29

[56] Koo D. & McKee C., 1992, ApJ, 388, 93

[57] Kormendy J., Bender R., Evans A., Richstone D., 1998, AJ, 115, 1823.

[58] Kotilainen J. K., Ward M., Boisson C., Depoy D., Smith M., 1992, MNRAS, 256, 125

[59] Kotilainen J.K, Ward J.M., Williger G.M., 1993, MNRAS, 263, 655

[60] Kotilainen J., Ward M., 1997, A&AS, 121 77

[61] Lai O., Véran J.P., Rigaut F., Rouan D., et al., 1996, Proc. SPIE Vol. 2871, p. 859-870,,

[62] Lai O., Rouan D., Rigaut F., Arsenault R., Gendron E., 1998, A&A, 334, 783.

[63] Lai O., Rouan D., Rigaut F., Arsenault R., Gendron E., 1999, A&A, in press.

[64] Laine S., Knapen J.H., Perez-Ramirez D. Doyon R., Nadeau D., 1998, MNRAS, 302, 33L.

[65] Lawrence A., & Elvis, M. 1982, ApJ, 256, 410

[66] Lawrence A. 1991, MNRAS, 252, 586

[67] Longair M., "High Energy Astrophysics", Cambridge University Press, Cambridge, UK, 1992

[68] Lucy L.B., 1974, AJ, 79, 745.

[69] MacKenty, J. W. 1990, ApJ Suppl., 72, 231

[70] Magain P., Courbin F., Sohy S., 1998, SpJ, 494, 472.

[71] Maiolino, R., & Rieke, G. H. 1995, ApJ, 454, 95

[72] Maiolino, R., Ruiz M., Rieke G., Papadopoulos P., 1997, ApJ, 485, 552

[73] Maiolino, R., Risaliti G., Salvati M., 1999, In Press, (AstroPh/9811237)

[74] Malkan, M.A., & Oke, J.B. 1983, ApJ, 265, 92

[75] Malkan M., Gorjian V., Tam R., 1998, ApJS, 117, 25.

[76] Malkan M., Rush B., Spinoglio L., 1993, ApJS, 89, 1

[77] Markarian B.E., 1967, Afz, 3, 24, "Galaxies with an ultraviolet continuum"

[78] Marco O., Alloin D., Beuzit J.L., 1997, A&A 320, 399

[79] McLean I., 1997, "*Electronic Imaging in Astronomy*", Wiley Interscience, NewYork.

[80] McLeod, K. K., & Rieke, G. H. 1995, ApJ, 441, 96

[81] Mihos, J. C., & Hernquist, L. 1996, ApJ, 464, 641

[82] Miller J. & Goodrich R., 1990, ApJ, 355, 456.

[83] Moles M., Marquez I., & Perez, E. 1995, ApJ, 438, 604

[84] Morris M., Serabyn E., 1996, ARA&A 34 645.

[85] Mulchaey J. S., Mushotzky R. F., & Weaver, K. A. 1992, ApJ Letters, 390, L69

[86] Mulchaey J. S., Koratkar A., Ward M., Wilson A., Whittle M.,.Antonucci R., Kinney A., Hurt T., 1994, ApJ, 433, 625

[87] Mulchaey J. S., Regan M. W., & Kundu, A. 1996, ApJ Suppl., 123, 455

[88] Mulchaey J.S., Wilson A.S., 1995, ApJ, 455L, 17

[89] Mulchaey J.S., & Regan M.W. 1997, ApJL, 482, 135l

[90] Mundell C.G., Holloway A., Pedlar A., Meaburn J., Kukula M., Axon D., 1995, MNRAS, 275, 67

[91] Mundell C.G., Pedlar A., Meaburn J.,Axon D., Unger S., 1996, MNRAS, 277, 641

[92] Mushotsky R.F., 1982, ApJ, 256, 92.

[93] Nadeau D., Murphy D.C., Doyon R., Rowlands N., 1994, PASP 106, 909

[94] Nadeau D., Doyon R., plus 8 authors 1998, SPIE, vol2301, 465

[95] Nagar N., Wilson, A., Mulchaey J., Gallimore, J., 1999, ApJS, 120, 345 (AstroPh/9901236)

[96] Nakajima T., Carleton N., Nishida M., 1991, ApJ Letters, 375, 1

[97] Norman, C. 1987, in *Galactic and Extragalactic Star Formation*, (eds. Pudritz, R. E. & Fich, M.), Kluwer, Dordrecht, p 495.

[98] Oke B., Schild R., 1971, ApJ 166, 95

[99] Osterbrock, D.E. 1977, ApJ, 215, 733

[100] Peterson, B. 1997, An Introduction to Active Galactic Nuclei, Cambridge University Press, Cambridge, UK, Ch. 7

[101] Pier E.A., Krolik J.H., 1992, ApJ, 401, 109

[102] Piner, B. G., Stone, J., & Teuben, P. 1995, ApJ, 449, 508

[103] Quillen A., Ramirez S., Frogel J., 1996, ApJ, 470, 790

[104] Regan M.W. & Mulchaey J.S. 1999, ApJ, In Press, astroph/9905138

[105] Richstone D., Ajhar E., Bender R., Bower G., plus 11 authors, 1998, Nature, 395, 14

[106] Rieke M. and Lebofsky A. 1985, ApJ, 288, 618

[107] Rigaut F., Arsenault R., Kerr J., et al.,1994, Proc. SPIE Vol. 2201, p. 149

[108] Rigaut F., Salmon D., Arsenault R., Thomas J., Lai O., Rouan D., Veran J-P., Gigan P., Crampton D., Fletcher J., Silburn J., Boyer C., Jagourel P., 1998, PASP, 110, 152

[109] Rix H. W., & Rieke M. J. 1993, ApJ, 418, 123

[110] Robson I., *Active Galactic Nuclei*, 1996 Wiley press, West Sussex, England.

[111] Roddier F.J., Graves J.E., McKenna D. , Northcott M.J. , 1991, Proc. SPIE Vol. 1524, p. 248

[112] Roddier F.J., 1999, Fundamentals of Adaptive Optics, in press.

[113] Rotaciuc V., Krabbe A., Cameron M., Drapatz S., Genzel R., Sternberg A., Storey J., 1991, ApJ Letters, 370, 23

[114] Rouan D., Rigaut F., Alloin D., Lai O., Doyon R., Crampton D., Gendron E., Arsenault R., 1998, A&A, 339, 687.

[115] Rush B., Malkan, M.A., & Edelson, R.A. 1996, ApJ, 473, 130

[116] Rush B., Malkan, M.A., & Spinoglio L., 1993, ApJS, 89, 1

[117] Sanders D. B., Phinney E., Neugebauer G., Soifer B., Matthews K., 1989, ApJ, 347, 29

[118] Sanders D.B., Solomon, P.M., & Scoville, N.Z., 1984, ApJ, 276, 182

[119] Sanford L., 1992 SPIE vol1969, 342

[120] Santos N., Yun J., Santos C., Marreiros R., 1998, AJ, 116, 1376

[121] Schinnerer E., Eckart A., Tacconi L., 1998, AGM 14, H08

[122] Schreier E., Capetti A., Macchetto D., Sparks W., Ford H., 1996, ApJ, 459, 535.

[123] Schreier E., Marconi A., Axon D., Caon N., Macchetto D., Capetti A., Hough H., Young S., Packham C., 1998, ApJ, 499L, 143

[124] Schwartz M. 1981, ApJ, 247, 77

[125] Scoville N., Matthews K., Carico D., Sanders D., 1988, ApJL, 327, L61

[126] Scoville N., Evans A., Dinshaw N., Thompson R., Rieke M., Schneider G., Low F., Hines D., Stobie B., Becklin E., Epps H., 1998, ApJL in press, astro-ph/9801006

[127] Sempere M., Combes F., Casoli F., 1995, A&A, 299, 371

[128] Seyfert C.K., 1943, "Nulcear emission in spiral nebulae", QB4 M93 n671

[129] Shlosman I., Frank, J., & Begelman, M. 1989, Nature, 338, 45

[130] Shlosman I., Begelman F., Frank C., 1990, Nature, 345, 679

[131] Simkin S., Su H. & Schwartz, M. 1980, ApJ, 237, 40

[132] Simons D., 1992, Redeye Users Manual, CFHT.

[133] Simpson C., Mulchaey J., Wilson A., Ward M., Alonso-Herrero A., 1996, ApJL, 457, L19.

[134] Smith D.A., Done C., & Pounds, K.A. 1993, MNRAS, 263, 54

[135] Spinoglio L., & Malkan M.A. 1989, ApJ, 342, 8

[136] Tenorio-Tagle G., Munoz-Tunon, C., 1998, MNRAS, 293, 299

[137] Terlevich R., Tenorio-Tagle G., Franco J., Melnick J., 1992 MNRAS, 255, 713

[138] Thuan T.X., 1983, ApJ, 268, 667.

[139] Tran H.D., Miller J., 1995a, ApJ 440, 578

[140] Tran H.D., Miller J., 1995b, ApJ 440, 597

[141] Tran H.D., Miller J.S., Kay,L.E., 1992, ApJ 397, 452

[142] Ulvestad J., 1986, ApJ, 310, 136.

[143] Ulvestad J., Wilson A. 1984, ApJ, 285, 439

[144] Unger S. W., Pedlar A., Axon D. J., Whittle M., Meurs E. J. A. Ward, M. J., 1987 MNRAS, 228, 671

[145] Vanzi R., Alonso-Herrero A., Rieke M., 1998, ApJ, 504, 93.

[146] Veilleux S., Goodrich R., Hill G., 1997, ApJ, 477, 631.

[147] Véran J.P., Rigaut F., Maitre H., 1998, SPIE, *Optical Science, Engineering and Instrumentation*, San Diego.

[148] Véran J.P., Rigaut F., Maître H., Rouan D., 1997, Journ. of the Optic. Soc. of America A 14, 11

[149] Véran J.P., 1997, Thesis, Ecole Nationale Supérieure des Télécommunications and Paris 7

[150] Veron-Cetty C. & Veron C., 1996 A&ASup, 66, 335

[151] Vila-Vilaro B., Robinson A, Perez E., Axon D., Baum S., Gonzalez-Delgado R., Pedlar A., Perez I., Perry J., Tadhunter C., 1995, A&A, 302, 58.

[152] Ward M.J., Blanco P.R., Wilson, A.S., Nishida, M. 1991, ApJ, 382, 115

[153] Ward M., Penston, M., Blades, J., Turtle, A. 1980, MNRAS 193, 563.

[154] Wehrle A. E., Morris M., 1988, AJ, 95, 1689.

[155] Weinberger A.J., Neugebauer G., Matthews K., ApJ, In Press, (astro-ph/9904076)

[156] Wilson A., 1996, Vistas in Astronomy, v40, 63.

[157] Wilson A., Tsvetanov Z. 1994, AJ, 107, 1227

[158] Wozniak H., Friedli D., Martinet, L., Martin, P., Bratschi, P. 1995, AA Supl, 111, 115

[159] Zitelli V., Granato G., Mandolesi N., Wade R., Danese L., 1993, ApJ Suppl, 84, 185